Electrochemo-mechanical Coupling in Electrocatalytic Oxidation of Methanol on Platinum

Vom Promotionsausschuss der
Technischen Universität Hamburg
zur Erlangung des akademischen Grades
Doktor-Ingenieurin (Dr.-Ing.)
genehmigte Dissertation (Monografie)

von
Xinyan Wu

aus
Liaoning, China

2025

Gutachter: Prof. Dr. Jörg Weissmüller
Prof. Dr. Patrick Huber

Tag der mündlichen Prüfung: 23. Juni 2025

DOI: `https://doi.org/10.15480/882.15816`

ORCID: `https://orcid.org/0000-0002-8068-788X`

Abstract

This study investigates the impact of elastic strain on platinum electrode surfaces and its effects on both the adsorption of reactants and the electrocatalytic oxidation of methanol in alkaline solutions. By exploring the coupling between external mechanical modulation and electrocatalytic activity, the research aims to uncover how strain influences both the reaction currents (Faraday currents) and the adsorption enthalpy of methanol and its intermediates.

To explore this coupling effect, two experimental approaches are employed. First, the impact of surface strain on adsorption enthalpy is assessed through surface stress variations, measured via cantilever bending experiments. Second, the strain effect on the overall reaction current is examined using Dynamic Electro-Chemo-Mechanical Analysis (DECMA). Here, a lock-in technique is utilized to capture strain-modulated reaction currents, quantifying them as functions of the applied potential. The study also discusses the role of uncompensated resistance in parameter adjustments, which is crucial for accurately interpreting the intrinsic coupling between externally applied strain and reaction currents on platinum thin film electrode surfaces.

Methanol oxidation reaction (MOR) is selected as the model system due to its importance in various industrial applications, including fuel cells and chemical production. To gain a deeper understanding of the complex electrocatalytic processes involved in MOR, classical electrochemical characterization techniques are employed, such as cyclic voltammetry (CV) and electrochemical impedance spectroscopy (EIS). These techniques are applied under different parameters and methanol concentrations to capture a comprehensive view of the reaction mechanisms.

The findings reveal that external strain significantly influences the methanol oxidation current. Tensile strain enhances reactivity at low overpotentials, while compressive strain becomes more effective at higher overpotentials, a condition more typical in practical applications. However, the adsorption enthalpy of methanol exhibits negligible dependence on strain, suggesting that the observed changes in electrocatalytic activity are not primarily driven by alterations in methanol adsorption strength. These insights underscore the importance of considering strain effects in the design of high-performance electrocatalysts. Understanding and quantifying how mechanical strain impacts overall reaction rates provides valuable guidance for developing more efficient catalytic materials.

Contents

List of Figures

Chapter 1

Introduction

1.1 Background of electrocatalysis

Since this century, more and more attention has been paid to develop new, clean, and efficient energy solutions. Fuel cells have emerged as a promising option due to their potential for clean and sustainable energy generation. These electrochemical devices convert chemical energy into electrical energy, offering high efficiency and environmentally friendly operation. Depending on the type of fuel cell and operating conditions, they can achieve energy conversion efficiencies ranging from 45% to 60% or even higher [1]. Such high energy efficiency makes it promising to lead to lower fuel consumption and reduced greenhouse gas emissions.

The concept of a fuel cell dates back over 180 years to the early 19th century, when William Grove first described the principle of electrochemical reactions capable of generating electricity using hydrogen and oxygen [2]. The modern development of fuel cells gained momentum in the mid-20th century, fuel cells were initially used in niche applications such as spacecraft, submarines, and remote power systems [3]. Recent years, extensive research and development efforts have been dedicated to improving fuel cell performance, durability, and cost-effectiveness. Advances in materials science, electrochemistry, and system engineering have led to significant progress in fuel cell technology, enabling their use in a wider range of applications, including stationary power generation for homes, businesses, and industries, transportation (e.g., fuel cell vehicles), portable power devices, and even auxiliary power units for aircraft and marine vessels. Fuel cells can operate using a variety of fuels, including methanol, ethanol, hydrogen, natural gas, and other hydrocarbons. This versatility in fuel options provides flexibility in fuel sourcing and utilization, which can be advantageous in various applications and geographic locations [4, 5]. There are many types of fuel cells [6–9], including proton exchange membrane fuel cells (PEMFCs), solid oxide fuel cells (SOFCs) [10, 11], molten carbonate fuel cell (MCFC), direct methanol fuel cells (DMFCs), and others, each with their unique advantages and limitations.

DMFCs represent a promising type of PEMFCs offering the potential to generate electricity through the direct oxidation of methanol, a readily available and easily transportable liquid fuel. In DMFCs, methanol is supplied to the anode compartment, where it undergoes oxidation through the methanol oxidation reaction (MOR) catalyzed by substances such as platinum. This reaction yields protons and electrons, which migrate through the proton exchange membrane to the cathode compartment. Here, protons combine with oxygen from the air to form water, releasing energy in the form of electricity [9, 12–16]. This process is illustrated schematically in Figure 1.1. The utilization of methanol as a fuel offers several advantages, including its wide availability from sources such as coal, coke oven gas, and natural gas. Moreover, the byproducts of methanol oxidation, primarily carbon dioxide and water, pose minimal environmental pollution, with the potential for carbon dioxide to be captured and recycled into methanol, thus achieving resource sustainability [17, 18]. However, a significant challenge in DMFCs lies in the sluggish kinetics of the methanol oxidation reaction, which impedes the overall efficiency and performance

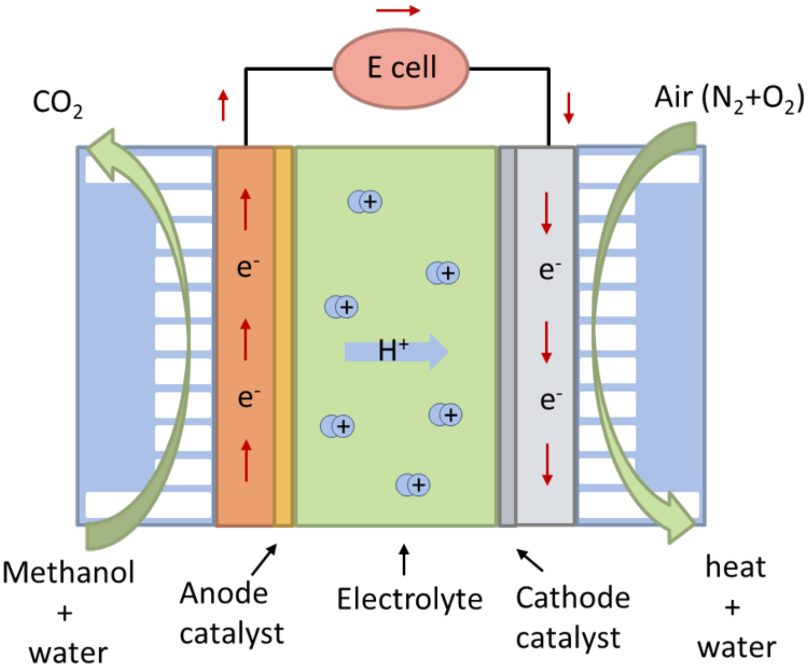

Figure 1.1: Schematic illustration of the structure of a Direct Methanol Fuel Cell (DMFC): at the anode (orange layer), methanol is oxidized, producing protons (H^+), electrons (e^-), and carbon dioxide as final product. The protons pass through the proton exchange membrane (green area), while the electrons flow through an external circuit, generating electrical energy (E cell). At the cathode (gray layer), oxygen reacts with the incoming protons and electrons, forming water. The overall process results in the generation of electricity, with carbon dioxide and water as byproducts.

of the fuel cell. Overcoming this obstacle requires the development of effective catalysts capable of accelerating the methanol decomposition process, thus enhancing the efficiency and viability of DMFC technology.

Platinum remains the best candidate of catalyst for methanol oxidation in DMFCs due to its superior catalytic activity [19–21]. The thermodynamic potential of methanol decomposition is actually quite low ($E^\circ = 0.02\text{V}$), which is comparable to hydrogen oxidation ($E^\circ = 0\text{V}$). However the reaction rate in reality is much slower than hydrogen oxidation reaction. There are some facts limit the efficiency of MOR, such as the methanol crossover through the proton exchange membrane [22] and the poison effect from the reaction intermediates, such as carbon monoxide (CO). CO is believed to adsorb strongly on the surface thus block the active spots and shows an ineluctable poisoning effect especially in acid electrolyte [23–29]. These effects lead to a fast decay in the catalytic stability and performance of Pt for MOR.

A parallel pathway mechanism of methanol oxidation with a series of intermediates has been extensively investigated and verified over the past few decades [30–32]. This oxidation process occurs via a six-electron transfer reaction, ultimately yielding CO_2 in acidic solutions:

$$\mathrm{CH_3OH + H_2O \longrightarrow CO_2 + 6\,H^+ + 6\,e^-} \tag{1.1}$$

and ${CO_3}^{2-}$ in alkaline environment:

$$\mathrm{CH_3OH + 8\,OH^- \longrightarrow {CO_3}^{2-} + 6\,H_2O + 6\,e^-} \tag{1.2}$$

One pathway is to go through a number of different soluble intermediates from methanol deprotonation, such as $HCOOH, HCHO, CO_2$, which can be oxidized by the hydroxide ions adsorbed on the Pt surface (PtOH) into final product without occupying surface active spots. Another pathway is to form CO and this strong bonding between Pt and CO is an inhibitor of the further oxidation reaction as the less Pt for OH adsorption and further oxidation, which is well-known as the poisoning effect, and mainly responsible, as the whole reaction rate determining step (RDS), to slow the kinetic of methanol oxidation.

1.2 Strain engineering in electrocatalysis

The strain effect, characterized by the deformation or distortion of the atomic lattice structure in catalyst materials, plays a crucial role in enhancing the reactivity of the MOR on Pt catalysts. In electrocatalysis, the application of mechanical strain can significantly modify the electronic structure and reactivity of catalytic materials, leading to either enhanced or suppressed catalytic activity [33–36].

Mechanical strain alters the energy levels of the electronic states within the material [33, 37], which in turn affects the binding energies of reactant molecules and intermediates on the catalyst surface. Specifically, by modifying the adsorption properties of these molecules, strain influences the kinetics of the reaction and the overall catalytic performance.

This phenomenon is particularly relevant in the study of Pt catalysts, especially in contexts such as Pt nanoparticle or nanoporous Pt synthesis [38, 39], surface modifications with secondary metals [40–42], and deposition on high surface area supports [43, 44]. Understanding and leveraging the strain effect is essential for optimizing Pt catalysts for MOR, as it directly impacts catalytic efficiency, stability, and selectivity. By elucidating the complex relationship between strain effects and catalytic activity, Pt catalysts with superior MOR reactivity is expected to be improved, thereby advancing the development of DMFC technology.

1.2.1 Enhanced electrocatalytic performance from strain modulation

Electronic theoretic density function theory (DFT) computation has been an effective method to understand the effects of strain on electrocatalytic properties and enable the rational design of strain-engineered catalysts with desired performance characteristics. The specific adsorbate–surface combinations was also rationalized to give a qualitative prediction on the response of binding energy on surface sites to strain [45].

From experimental observations, many studies have indeed reported enhanced electrocatalytic performances of strain-modified materials. Han *et al.* reported a considerably improved stability and activity of a Pt-enriched anodic material via strain engineering in practical fuel cell operations [46]. Peter Strasser attempted to isolate the strain effect from ligand and geometric effects using a core-shell structure of dealloyed Pt-Cu, which contains a few atomic monometallic layers. This structure is supported on a substrate with different lattice parameters, and shows improved catalytic reactivity for the oxygen-reduction reaction (ORR) in fuel cell electrodes [47]. To measure the strain in core-shell materials, a recently developed technique called 4D-scanning transmission electron microscopy (4D-STEM) nanobeam electron diffraction has been reported, providing an effective and accurate method to map the quantitative lattice strain. This technique distinguishes the nanocube core from the shell and quantifies the unit cell size as a function of distance from the core-shell interface [48].

Understanding and controlling strain effects on catalysts can lead to the design and development of more efficient electrocatalysts for various energy conversion and storage applications. However, during the synthesis process of above experiments, the strain effect always companies with ligand or geometric effect, which hinders the discussion on correlation between strain effect and catalytic reactivities. Even though many studies tried to isolate the strain effect by focusing on catalytic nanostructures for which the surface strain effect has the dominant role, gaining a better understanding of exclusive strain effect in the enhancement of electrocatalytic reactivity is still necessary and stays challenging.

1.2.2 Strain modified Pt and Pt based nanomaterial for methanol oxidation reaction

Pt and Pt-based catalysts are considered as the most effective catalytic materials for MOR due to their outstanding catalytic performances. As introduced before, the main two pathways of MOR are through CO (poisoning catalyst surface activity) and through HCOOH like soluble intermediates. Pt/C catalyst, as the most common used material for MOR, suffers from the poising pathway, as it has a relative lower reaction barrier than the second reaction pathway. In this case, the step of oxidizing surface adsorbed CO into COOH or CO_2 governs the whole methanol oxidation reaction rate, as it is the most sluggish step or subreaction, namely the reaction rate determining step (RDS). Strain engineering involves applying mechanical stress or altering the lattice structure of a material to modify its properties. In the specific context of Pt and Pt-based catalyst material for MOR, strain modification can enhance catalytic activity by tuning the adsorption energies of reaction intermediates involved in MOR.

Numerous studies have explored strategies to enhance the catalytic efficiency of Pt for MOR, with a common goal of synthesizing low Pt-containing catalysts while maintaining high reactivity. Increasing the surface area of Pt catalysts has emerged as a key approach to improving efficiency. Methods such as Pt nanoparticle synthesis, nanoporous structures, nanowires, and core-shell configurations offering high surface area-to-volume ratios, effectively maximizing the catalyst's active surface area [49–53]. Strain effect plays important role in all these mismatching situations. Zhang and *et.al* observed enhanced electrocatalytic activity on core-shell CoPt nanocomposite catalysts towards methanol oxidation, as the different thickness of Pt shell exhibit different strain effect [54]. Synthesized core-shell CoPt nanocomposite catalysts showed enhanced catalytic activity in the methanol oxidation reaction. The enhancement may result from favorable strain effects related to the thickness of Pt shell formed on the non-noble metal substrate. Alternatively, deposition of Pt on high surface area supports is also a popular way to increase the surface area, such as carbon black or mesoporous silica [55–59]. Tianou He recently reported a study of a wide control of the electrocatalytic reactivity of Pt shell for MOR, finding that the strain-activity correlation actually follows an M-shaped tendency [60]. Strain engineering can also be combined with alloying strategies to further enhance the catalytic activity and selectivity of Pt-based catalysts for MOR. Alloying Pt with other metals, such as copper (Cu) [52], ruthenium (Ru) [49, 50], palladium (Pd) [61, 62], tin (Sn) [63, 64], molybdenum (Mo) [65], rhenium (Re) [66], bismuth (Bi) [67] and others, which are less noble and more tolerant towards CO poisoning, can also improve the overall catalytic performance of Pt for MOR.

1.3 Strain-reactivity coupling effect

The consistency of whether tensile or compressive strain is more beneficial to improve MOR activity on Pt is still under discussion. Also, the most important fact is that when placing an overlayer on the bulk or adding extra alloying metal elements, the changes in electronic structure originate not only from a strain effect but also from electrons exchange (ligand effect). Ligand effect can alter the catalytic activity by modifying the electronic properties of the active sites, changing how reactant molecules bind to the surface. Both strain and ligand effects are particularly pronounced at surfaces and interfaces where the local atomic arrangement differs from that of the bulk material. In order to investigate the strain effect exclusively, researchers face unique challenges and develop sophisticated experimental techniques and simulation methods.

Smetanin and Weißmüller introduced a self-designed setup, which is also the main technique applied in this thesis work, Dynamic Electro-Chemo-Mechanical Analysis (DECMA), which successfully provided an effective way to quantify the potential response directly to externally applied strain on Au thin film surface [68, 69]. This method is beneficial for skipping the trivial interpretation of the intermediates interaction and adsorption enthalpy, offering a bridge to link the electrocatalytic current to external elastic strain as shown in Figure 1.2. Deng made a further

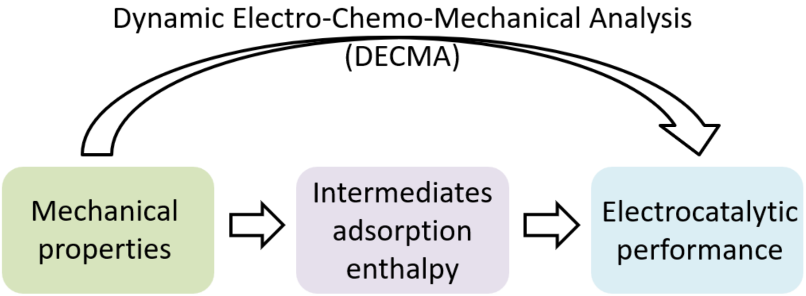

Figure 1.2: Schematic representation of the concept of Dynamic Electro-Chemo-Mechanical Analysis (DECMA), the diagram illustrates how mechanical properties influence the adsorption enthalpy of reaction intermediates, which then impacts the overall electrocatalytic performance. DECMA provides a direct method to quantify the coupling effect between mechanical strain and electrocatalytic current. This approach helps in understanding the interdependence of mechanical and electrochemical properties in electrocatalysis, allowing for skipping the intermediate steps in the electrocatalytic process.

development towards this direction and investigated the reaction current response to applied cyclic strain modulation on Au and Pt in the form of a strain-reactivity coupling coefficient in the fundamental electrocatalytic reaction - hydrogen evolution reaction (HER) [70]. Yan and coworkers also reported the elastic strain effect in HER reaction but on Ni, Pt and Cu by a setup allowing *in situ* mechanical loading/unloading to the thin film metal on polymethylmethacrylate substrates support [71]. They found that compressive strain can enhance the activity of Ni and Pt, but decrease the activity of Cu. By the same method, they also demonstrated a large elastic strain effect on a tungsten carbide film. It induced larger changes in catalytic activity towards HER and the compressive strain has a positive effect [72]. Fernando reported a study of depositing a Pt layer with different thickness (thus tunable strain in the Pt layers) onto Au(111) substrate for investigating the surface strain effect on the adsorption and oxidation of methanol, and found that slightly compressive strain increases the reaction activity [73].

1.4 Outline of this thesis

This thesis presents a study on mechanical and electrochemical coupling effect in the form of coupling coefficients during methanol oxidation reaction on sputtered Pt thin films in alkaline environment. In this dissertation, the advantages and limitations of strain in altering the electrocatalytic properties of heterogeneous catalytic materials are discussed, emphasizing the importance of bringing the concepts of mechanoelectrochemistry into the traditional field of electrocatalysis. So far, the most widely investigated electrocatalytic reactions with strain effect are hydrogen evolution reaction (HER) [71, 74–79] and oxygen evolution reaction (OER) [74, 79–82], as they are simple reactions with only one or two reaction steps, and showing more straightforward relation with strain effect. In this PhD work, a more complex electrocatalytic reaction, methanol oxidation reaction (MOR), is investigated aiming to provide a more direct evidence of strain effect on overall reaction without looking into each single step and bring the concept of mechanoelectrochemistry into a broader field of electrocatalysis. A detailed electrochemical study of cyclic voltammogram performance has been carried out on Pt electrode surface during methanol oxidation reaction in 0.1 M KOH support electrolyte with different concentration of methanol. The reaction mechanism and possible reaction path ways were discussed. Simultaneously with CV measurements, the *in situ* stress variation was measured by a cantilever bending experiment to monitor the surface stress evolution during the methanol molecule and its intermediates adsorption, desorption and oxidation processes. The current-strain coupling coefficient gives a clear relationship between MOR reaction activity and external strain effect on Pt electrode.

There are six chapters of this thesis. It starts with a general introduction of the electrochemical background of direct methanol fuel cell which applies methanol oxidation reaction as the main electrocatalytic reaction to improve the energy convert efficiency, then follows the introduction of strain engineering of nanomaterials and summarizes recent progress and achievements in strain modified catalytic nanomaterials from both theoretical simulation and practical experiments. The strain-reactivity relation is emphasized as a possibility to understand the motivation on how to improve electrocatalytic activity from mechanical modulation.

The second chapter gives the theoretical background of this study, including some important fundamental definitions and concepts in electrochemistry, and introduction of some commonly used electrochemical measurement methods. It also gives detailed information on the coupling parameters which are used to quantify the strain modulation on electrode potential (potential-strain coupling coefficient, ς) and reaction current (current-strain coupling coefficient, λ). At the end of this chapter, the model reaction in this work – methanol oxidation reaction – is elaborated in terms of the reaction mechanism and all possible reaction sub steps. All the possible reaction intermediates are summarized with their names and chemical formations in a list.

Chapter three covers all experimental-related information, including the setup and connection circuit illustrations, sample fabrication procedures, and facilitated strategies used throughout the research.

Chapter four presents the experimental results, beginning with the characterization of sputtered Pt thin film samples using X-ray diffraction (XRD) and atomic force microscopy (AFM) to analyze surface orientation and morphology. Then the CVs of Pt electrode in different electrolytes are presented with different cyclic scan strategies to provide a clear picture of MOR on Pt in alkaline environment, followed by stress variation measurement in a series electrolyte with different methanol concentration and DECMA results in 0.1 M KOH with 0.1 M methanol electrolyte.

In chapter five, all important findings in this work are discussed, including different reaction mechanisms, the potential rate determining steps in various situations, and the dual role of the Pt surface oxides the its influence on the reaction reactivity. The adsorption of methanol, its intermediates, and CO at different reaction stages is elaborated upon the surface stress evolution. Also the tensile and compressive strain effects were discussed in different potential regions during the reaction process.

The final chapter provides an outlook on future DECMA studies on Pt and Au thin film surfaces during another important electrocatalytic reaction: the oxygen reduction reaction (ORR). Preliminary results are presented, and potential research directions are proposed to further advance the understanding and optimization of electrocatalytic reactions.

Chapter 2

Theoretical background

2.1 Electrochemistry

2.1.1 Electrochemical cell: three-electrode system

A typical electrochemical cell is a device consisting of electrodes immersed in an electrolyte solution in a vessel. A three-electrode system is a configuration commonly used in electrochemical experiments, which includes a working electrode (WE), reference electrode (RE), and counter electrode (CE), as shown in the Figure 2.1. Such setup is widely used in techniques such as cyclic voltammetry, chronoamperometry, and electrochemical impedance spectroscopy for studying electrode processes, corrosion, and various electrochemical reactions.

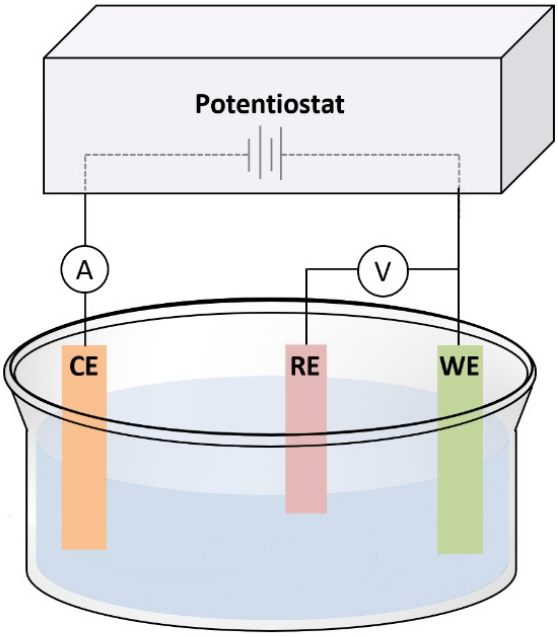

Figure 2.1: Schematic representation of a three-electrode electrochemical cell and its equivalent circuit diagram. The cell consists of working electrode (WE), reference electrode (RE) and counter electrode (CE).

The WE is the main part of this whole three-electrode electrochemical cell system, as the most interesting part-electrochemical reduction-oxidation reactions (REDOX) happen on the interface between working electrode and electrolyte with electrons transferring through. The WE is typically made of a material relevant to the interests of experiment. A small area of working electrode is always favorable towards some electrochemical cells without ideally designed configuration to minimize the IR drop (R_U, uncompensated solution resistance), especially when there is high reaction current passing through. The WE bears the applied potential from a potentiostat with reference to an ideal non-polarizable RE, which has a stable equilibrium potential. The function of this reference electrode is to be used as a reference to give a measurable potential on WE, and there is no current flow through them. The CE helps to complete a whole circuit to make current be able to flow. The CE is typically made from inert materials, such as Pt or graphite, with a big surface area to guarantee that the kinetics of the reaction occurring on it do not interfere the one happening on the WE.

2.1.2 Structure of electrode-liquid interface

The electric double layer (EDL) forms at the interface between the electrode and the electrolyte, resulting from charge separation. The electrode surface is often charged by the dissociation of surface groups or the selective adsorption of certain ions from the solution, as shown in Figure 2.2. Maintaining electrical neutrality necessitates an excess of counter ions in the liquid adjacent to the charged surface, balancing the solid surface charge but with opposite polarity. It consists of the Stern layer, containing specifically adsorbed ions near the electrode, and the diffuse layer, comprising ions attracted to the electrode by electrostatic forces but not specifically adsorbed. The structure and composition of the EDL are very depending on factors such as the nature of the electrode material, the electrolyte composition, and the applied potential.

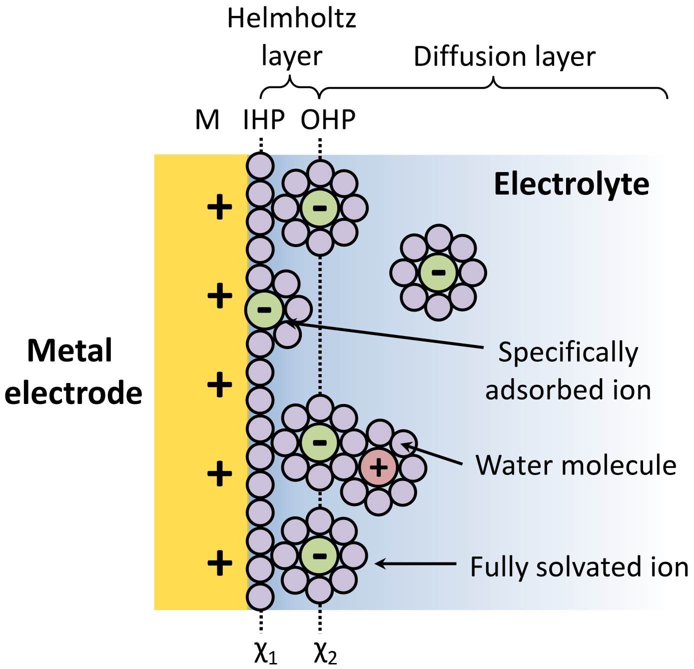

Figure 2.2: The model of the electrical double layer, illustrating the structure of Helmholtz layer. The Helmholtz layer comprises two planes: the inner Helmholtz plane (IHP), located at a distance χ_1 from the metal-solution interface, and the outer Helmholtz plane (OHP), positioned χ_2 units away from the interface. Beyond the OHP lies the diffusion layer, extending into the bulk solution.

According to Stern's perspective, a portion of the counter ions closely binds to the surface due to specific ion adsorption or non-electric attractions, such as van der Waals forces, forming an inner layer known as the compact, Helmholtz, or Stern layer. The center of specifically adsorbed ions is χ_1 distance away from the interface, defining the inner Helmholtz plane (IHP), while the center of fully solvated ions, χ_2 away from the interface, marks the outer Helmholtz plane (OHP). The region extending from the OHP to the bulk solution constitutes the diffusion layer, where nonspecifically adsorbed species are distributed.

At a given potential, the charge on the metal electrode surface is denoted as q^M, and the charge in the solution side is q^S. Consequently, the surface charge density is defined as $\sigma^M = q^M/A$, where A represents the electrode surface area. Thus, the overall charge density $-\sigma^M = \sigma^S = \sigma^i + \sigma^d$, where σ^i denotes the charge density of specifically adsorbed ions and σ^d represents the charge density in the diffusion layer.

Imagine a typical resistor-capacitor (RC) circuit incorporating an electrical double-layer capacitor, depicted in Figure 2.3. In this circuit, the overall potential is determined by $E = iR + q/C_d$, where R represents the resistance, C_d denotes the double-layer capacitance, and q is the charge stored in the capacitor. The current flowing through the circuit is

$$i = \frac{dq}{dt} = -\frac{q}{RC_d} + \frac{E}{R} \tag{2.1}$$

At the beginning (t=0), differentiate Equation 2.1, the relationship between current and time shows current decreasing exponentially along time axial:

$$i = \frac{E}{R} e^{\frac{-t}{RC_d}} \tag{2.2}$$

τ is the time constant, this is the time lag that the charging takes up before the interface can reach the desired potential. And when $t = \tau$, the current decreases to 37% of its initial value and when $t = 3\tau$, the charging current reaches 95%.

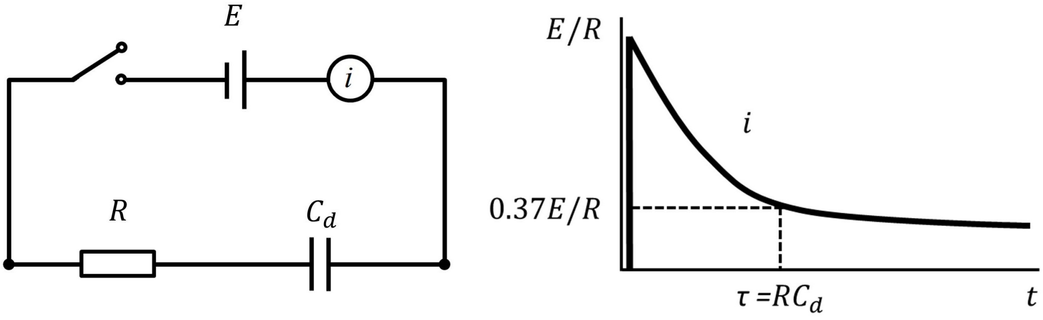

Figure 2.3: Left is the RC equivalent circuit diagram including a capacitor (analogous to double layer's capacitive behavior) and a resistance component. Right is measured capacitive current variation versus time.

In electrochemical systems, the time constant depends on factors such as the diffusion of ions to and from the electrode surface, the kinetics of electrochemical reactions, and the resistance of the electrolyte solution.

2.1.3 Resistance in electrochemical system

In an electrochemical system, there are several resistances which can influence the overall behavior and performance of an electrode in electrochemical reactions. From the WE to CE, the overall resistance contains the interface resistance (charge transfer resistance, R_{ct}, and diffusion resistance, R_d), uncompenstated resistance, R_u (the resistance between WE and RE) and the resistance between the CE and the RE (R_e). The sum of last two parts is always referenced in literature as the electrolyte resistance or solution resistance, most of it are the uncompensated resistance, so in some research, the uncompenstated resistance is also used to represent the solution resistance. According to the working principal of a potentiostat, it can consider the R_e but can not recognize the R_u, as the potentiostat drives the current flow between CE and WE until the potenial drop between RE and WE reaches the desired potential value. The last but not the least is the contact resistance (R_c), which is from the thin film sample resistance and the connection resistance in the whole electronic circuit. These resistances, alongside capacitance and inductance, are integral components incorporated into equivalent circuit models. Such models are commonly used to analyze electrochemical impedance data obtained from electrochemical measurements.

IR drop/Uncompensated solution resistance (R_u)

When there is current flowing through the whole electrochemical cell system, the driving force (overpotential) is distributed not only on working electrode but also in electrolyte, this potential drop through the electrolyte solution is called the solution resistance, R_{sol}, which is the resistance of the electrolyte.

In practice, a potentiostat controls the potential between the WE and the CE based on its operating principle. However, to align the user-set potential value as closely as possible to the real potential difference between the WE and the RE, the potential of the CE is set to a compliance value by the potentiostat. Despite efforts to minimize the distance between the WE and RE, inherent resistance inevitably arises due to their separation, causing a potential drop across the electrode-electrolyte interface. This resistance cannot be fully compensated by the potentiostat, resulting in an error in the applied voltage value:

$$E = E_{app} - iR_u \tag{2.3}$$

Thus, the actual potential (E) is always lower than the applied value from the potentiostat and varies depending on the magnitude of the reaction current. Even with a low uncompensated resistance, the IR drop becomes significant at high reaction currents, and sometimes potentially causes a distortion of the cyclic voltammogram, an illustration of such distortion is shown as Figure 2.4.

There are three common experimental methods to measure this uncompensated IR drop by potentiostat: electrochemical impedance spectroscopy(EIS), current interrupt technique and positive feedback. In practical, there are various factors that can contribute to potential drop at the interface between the working electrode and the electrolyte, regardless of the technique employed during controlled-potential operation. Some common factors are: inadequate electronic conductivity of the catalyst, insufficient electrolytic conductivity of the solution, the separation distance between the RE and the WE, resistance in the contacts, and the irregularity of the electrode surface [83–86].

To mitigate the uncompensated IR drop, three common strategies are employed:

1. **Luggin capillary design**: introduce a Luggin capillary design to avoid the perturbation of the potential distribution. The Luggin capillary is typically a narrow tube positioned few millimeters away to the WE to minimize the physical distance between WE and RE efficiently, thus reducing the IR drop. This design is often employed in electrochemical setups. A Luggin capillary is applied to the cell of DECMA setup in this work (see in Figure 3.5).
2. **WE area reduction**: Decrease the WE area to reduce current and diminish the IR drop effect.
3. **Highly conductive supporting electrolyte**: Select a highly conductive supporting electrolyte to decrease the overall solution resistance, thereby reducing the uncompensated resistance.

2.1.4 Nonfaradaic and faradaic process

Nonfaradaic and faradaic processes are two fundamental phenomena that occur at an electrode surface. The core difference between these processes lies in whether there is charge transfer through the electrode-electrolyte interface.

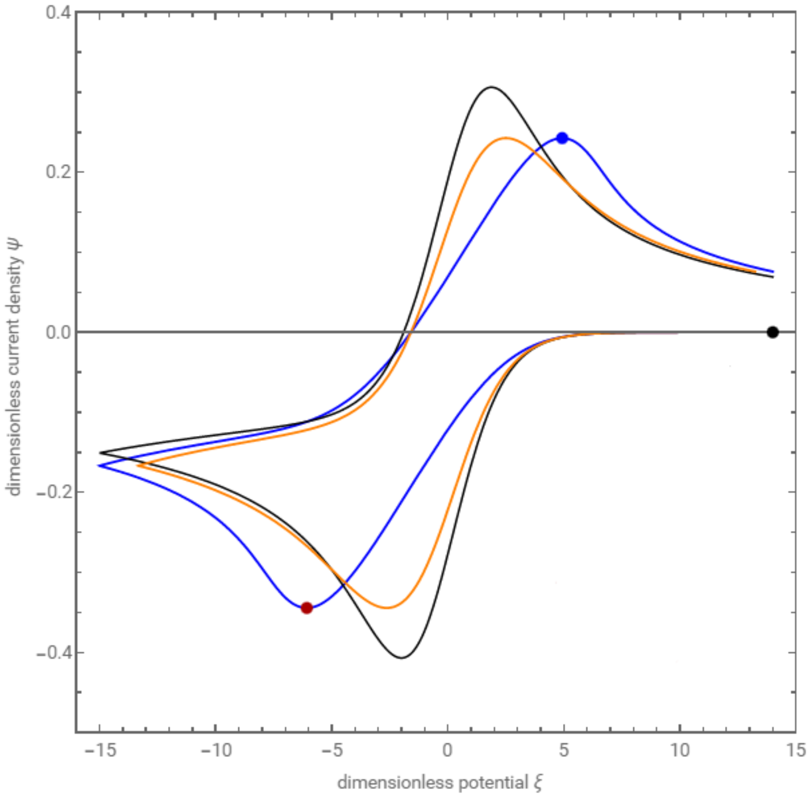

Figure 2.4: Demonstration of the cyclic voltammogram with undesirable effect of the uncompensated IR drop effect. Black solid line shows the ideal CV of a redox reaction without suffer from IR drop; blue solid line is the CV corrupted by IR drop; orange line is the CV obtained from the blue line when the electrode potential is numerically corrected from IR drop.

In a nonfaradaic process, there is no charge transfer at the electrode, meaning no redox reactions occur during this process. As introduced in Section 2.1.2, within the double layer region, the charges remain at or on the electrode surface and do not transfer through the interface. This characteristic is a defining feature of nonfaradaic processes, also known as capacitive processes. During a nonfaradaic process, charges can be stored at the electrode surface, leading to changes in its composition over time.

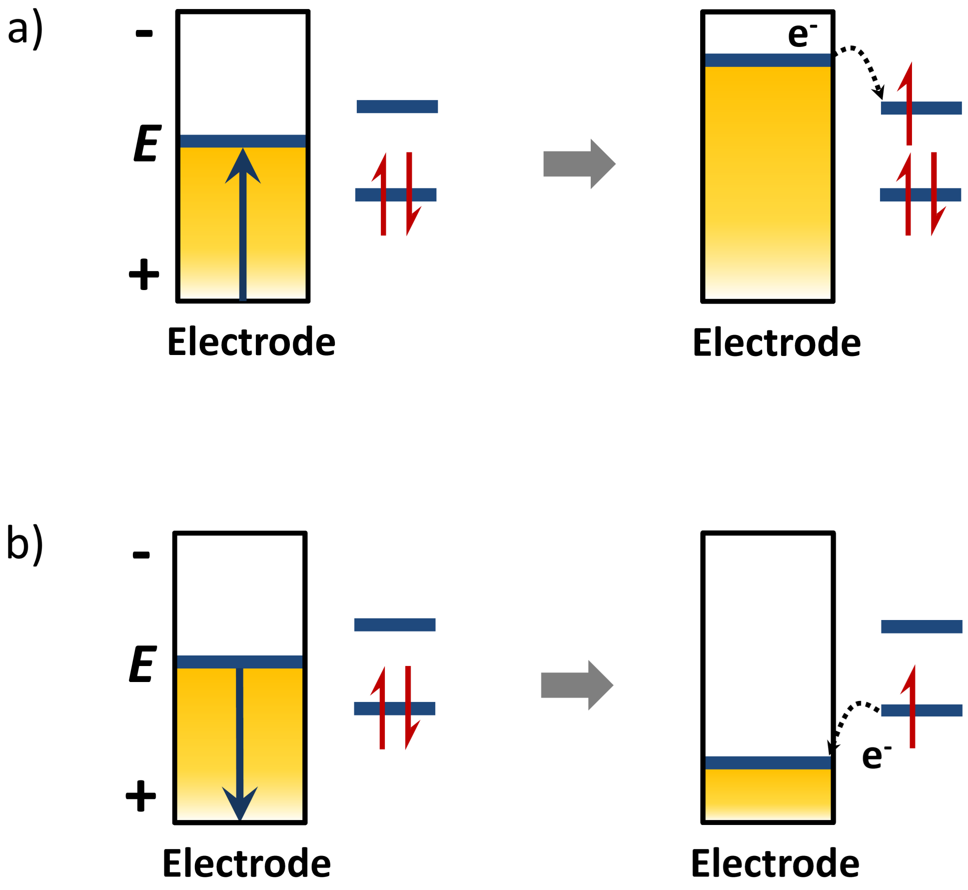

Figure 2.5: Schematic illustrations of reduction and oxidation processes driven by potential control at the interface between electrode and electrolyte. a) is the oxidation process, where the a positive potential is applied, the electrons in the metal electrode are raised to a higher energy level and are able to transfer from the electrode to electrolyte. b) shows the opposite scenario, where a negative potential is applied, causing electrons to move from the electrolyte to electrode.

When there is charge or electron transfer through the electrode-electrolyte interface and causing oxidation or reduction reactions on the electrode surface, the process is termed a faradaic process. As shown in Figure 2.5, when increasing the energy of electrons by driving the potential more negatively, the electrons overcome the energy barrier and transfer through the interface into electrolyte. The electrode loses electrons and is oxidized in a chemical reaction, and species in solution thus gain electrons from the electrode, causing a reduction process. Similarly, when decreasing the electrons energy by increasing the electrode potential causing the opposite phenomenon, namely the oxidation reaction.

This process follows Faraday's laws of electrolysis[a]. So in a faradaic reaction, the reactants

---

[a] Faraday's laws of electrolysis, first described by Michael Faraday in 1833, state that (1) the amount of chemical change produced by current at an electrode-electrolyte interface is proportional to the quantity of relatively consumed electricity; (2) the amounts of chemical changes produced by the same quantity of electricity in different substances are proportional to their equivalent weights.

and products as well as the potential intermediates should be involved as parts of this process. The key character of faradaic process is that the reactants which come from the bulk solution can approach the electrode surface by mass transfer and conduct charge exchange with the electrode then form products which will eventually leave the electrode surface and transfer back to the bulk solution. In other words, the charges should be taken away by products or intermediates and do not stay or store around the electrode-electrolyte interface.

Also these two processes exhibit totally different behaviors in cyclic voltammetry (CV). In capacitor (double layer) region, the current-potential curve shows in a quasi-rectangular shape and is proportional to the scan rate ν. Whereas the faradaic current response to potential can form distinguished peaks at specific potential and the value of this peak is proportional to the ν or $\nu^{1/2}$. When there is a faradaic reaction occurring at a potential, a corresponding peak appearing in a CV curve. However, the opposite is theoretically not correct, which is related to a phenomenon called pseudocapacitance[b]

2.1.5 Thermodynamics of an electrode

Open circuit potential(OCP)

Open circuit potential is the equilibrium potential measured between reference and working electrode when the circuit is open, namely without applying any voltage and current.

$$E_{ocp} = E_{we} - E_{re}, (i = 0) \tag{2.4}$$

When a system is at open circuit potential, the electrode reaches a dynamic equilibrium with the surrounding electrolyte and there is no current flow in the system. Consequently, the measured potential at this condition can provide valuable information about the thermodynamics of the electrochemical reactions occurring at the electrodes. OCP can be measured using a high-impedance voltmeter or a potentiostat. When measuring OCP, the counter electrode should be bypassed or with no applied potential to the cell from potentiostat. A constant OCP (normally less than ±5 mV) lasting for few minutes indicates that the system should be thermodynamically stable for measurement. The value of the OCP can be affected by several factors, such as temperature, concentration and type of ions present in the solution, as well as the electrode surface conditions.

Potential of zero charge (PZC)

PZC is a fundamental concept in electrochemistry, especially in the study of electrode-electrolyte interfaces. At this potential, the surface electrostatic charge of an electrode is zero, namely the surface is neither positively nor negatively charged. Generally, PZC deals with electrode surface phenomena, while OCP concerns the overall redox behavior in the whole electrochemical system. In some specific situations, the pzc might coincide with OCP, but it is not the general case.

There are some methods to determine the PZC. Normally near the PZC, the capacitance of the double layer typically reaches a minimum, where the surface tension reaching a maximum. So from the impedance measurement, PZC should be found at the point where the imaginary part of impedance is a minimum. Also, CV can be used to provide as an indirect method to determine PZC, as during the cyclic sweeping, the potential at which the faradaic current is zero indicating a minimal charge transfer thus offering an estimation of PZC.

---

[b] Pseudocapacitance is a conception to describe the phenomenon that the charge storage shows in faradaic behavior (with charges transfer through the electrode-electrolyte interface) but in the form of capacitive cyclic voltammetric signature. This is a relative novel notion in the last four decades in electrochemistry discipline especially in case of metal oxide formation system.

Equilibrium electrode potential: Nernst equation

The Nernst equation is a fundamental equation in electrochemistry to describe the relationship between the potential of an electrochemical cell and the concentrations of the reactants and products. It is often used to calculate the instantaneous potential from the standard potential (E^0) and the reaction quotient (Q)[c], and the number of transferred electrons (n) at a give temperature (T).

In an electrochemical system, the electrode potential represents the energy per unit charge. The total energy of the system is related to the potential and the amount of charge transferred. The Gibbs free energy change ΔG in a redox reaction is related to the cell potential E:

$$\Delta G = -nFE \tag{2.5}$$

where n is the number of electrons transferred in the reaction, F is Faraday's constant (F = 96485 C/mol). And the *standard electrode potential*[d] is related to the *standard Gibbs free energy* change for the reaction:

$$\Delta G^0 = -nFE^0 \tag{2.6}$$

Consider a general simplified redox reaction with only n electrons transfer:

$$\mathrm{O} + \mathrm{ne}^{-1} \rightleftharpoons \mathrm{R} \tag{2.7}$$

The free energy of this system represents the work done by the cell, $\Delta G = W = qE$, q is the charge ($q = nF$) and related to the activity variation of the reactants and products in terms of:

$$\Delta G = \Delta G^0 + RT \ln \frac{a_R}{a_O} \tag{2.8}$$

R is the universal gas constant ($8.314\ \mathrm{J \cdot mol^{-1} \cdot K^{-1}}$)) and T is the temperature in Kelvin. The activity can be replaced by concentration($\mathrm{mol \cdot L^{-1}}$) when the concentration of the solution is low[e]:

$$\Delta G = \Delta G^0 + RT \ln \frac{C_R^*}{C_O^*} \tag{2.9}$$

The direction of a reaction that consumes electrons is termed as an oxidation process, while the reversed process involving the liberation of electrons is referred to as reduction. In the case of a reversible electrode reaction, when the rate of the forward reaction (O→R) is equal to the rate of the reverse reaction (R→O), it signifies that the charge transport rates in both directions are balanced. This equilibrium point, where the reaction achieves dynamic equilibrium, is known as the equilibrium electrode potential or reversible electrode potential (E_{eq}):

$$E_{eq} = E^0 - \frac{RT}{nF} \ln \frac{C_R^*}{C_O^*} \tag{2.10}$$

This equation can be written in a more practical way for a quick calculation (at $T = 298$ K):

$$E = E^0 - \frac{0.0592\ V}{n} \log Q \tag{2.11}$$

---

[c] In chemistry, a reaction quotient Q is a function of the activity or concentration of a chemical within a reaction, and in the redox reaction $\mathrm{O} + \mathrm{ne}^{-1} \rightleftharpoons \mathrm{R}$, $Q = \frac{a_R}{a_O} = \frac{C_R^*}{C_O^*}$, which resembles the equilibrium constant expression, k, but considers the current concentrations rather than the equilibrium concentrations.

If $Q < k$, the reaction will proceed in the forward direction to reach equilibrium, and if $Q > k$, the reaction will proceed in the reverse direction to reach equilibrium. When $Q = k$ the system is at equilibrium.

[d] standard states usually refers to 1M concentration for solutes, 1 atm pressure for gases, and pure solids or liquids, and the temperature is 298.15 K (25°C).

[e] Activity, a, is a concept in chemistry that quantifies the "effective concentration" of a species in a mixture, which takes into account non-ideal behavior due to interactions between molecules. $a = \Upsilon C$, Υ is the activity coefficient, and when the concentration is low, Υ tends to unify, namely the activities can be replaced by species concentration.

In electrochemistry, Gibbs free energy calculations provide a way to assess the spontaneity of reactions and predict whether they are thermodynamically favorable or not. The Nernst equation can help to determine the potential at which a specific redox reaction occur under a given condition.

2.1.6 Kinetics of electrode reaction

Thermodynamic analysis of electrochemical reactions provides essential insights into their feasibility by determining the Gibbs free energy change (ΔG) and the equilibrium potential. This analysis helps ascertain whether a reaction is energetically favorable or not. However, thermodynamics alone cannot explain how quickly a reaction will proceed under given conditions. To understand the reaction rate, kinetic analysis is required, which examines the relationship between overpotential and the exchange current density.

Overpotential

Overpotential (or overvoltage), denoted as η, is the extra potential that applied to an electrochemical cell to drive a reaction at a certain rate (faster than the rate under equilibrium conditions). It is the difference between the actual electrode potential when a current is flowing and the equilibrium potential of the electrode where no net current flows. The overpotential accounts for the losses due to kinetic limitations and resistances in the system.

$$\eta = E_{j\neq 0} - E_{j=0} \tag{2.12}$$

Here, $E_{j\neq 0}$ is the electrode potential when there is current flowing, $E_{j=0}$ is the equilibrium potential, where the current density (j) is zero. Therefore, overpotential can only be measured when a current is present in the electrolyte. In essence, overpotential reflects the additional energy required to overcome various resistances (such as charge transfer resistance, mass transport limitations, and other losses) in order to sustain the electrochemical reaction at a desired rate.

Overpotential-current: Butler-Volmer (BV) equation

In the case of a complex reaction, which can be broken down into a series of elementary reactions, understanding the kinetics of each step is crucial. These elementary steps often exhibit significant differences in their reaction rate constants (k), sometimes spanning several orders of magnitude. Among these steps, the one with the slowest rate, known as the rate-determining step (RDS), dictates the overall rate of the reaction. The kinetics associated with this rate-determining step fundamentally govern how quickly or slowly the entire reaction proceeds.

Considering the electrode process as Equation 2.7, the reaction rate is defined as the amount of product per electrode area in unit time, and is proportional to the concentration of O species, the kinetics can be further understood in terms of the concentration of O species at different locations and times.

At a distance x from the bulk electrolyte to the electrode surface, denoted as $C_O(x,t)$, and at the surface the concentration is $C_O(0,t)$, and anodic reaction rate (where reactants convert into products) v_a and the cathodic reaction rate (where products convert back into reactants) v_c can be described as:

$$v_a = k_a C_R(0,t) = \frac{i_a}{nFA} \tag{2.13}$$

$$v_c = k_c C_O(0,t) = \frac{i_c}{nFA} \tag{2.14}$$

Due to the reversible nature of electrochemical reactions, reactants continuously convert into products and products simultaneously convert back into reactants. The individual reaction rate constants for the forward (k_a) and backward (k_c) reactions govern this process.

When there is an exchange of current through the electrode-electrolyte interface, both forward and backward reactions are occurring simultaneously. The net reaction rate at the interface is the difference between the rates of the backward (v_c) and forward (v_a) reactions:

$$v_{net} = v_c - v_a = k_c C_O(0,t) - k_a C_R(0,t) = \frac{i_{net}}{nFA} \tag{2.15}$$

Thus, the overall reaction net current is

$$i_{net} = nFA[k_c C_O(0,t) - k_a C_R(0,t)] \tag{2.16}$$

Here, v_{net} represents the overall net reaction rate, i_{net} is the net current, n is the number of electrons transferred in the reaction, F is Faraday's constant, and A is the electrode area. This equation describes how the net current is related to the difference between the rates of the forward and backward reactions, reflecting the dynamic balance between these opposing processes at the electrode-electrolyte interface.

When there is a variation of electrode potential (from E_1 to E_2, as shown in Figure 2.6), the energy levels for both oxidation and reduction reactions shift accordingly. The energy contributions from oxidation and reduction under the influence of a change in electrode potential can be expressed as follows:

$$\Delta G_a = \Delta G_{0a} - (1-\alpha)F(E_2 - E_1) \tag{2.17}$$

$$\Delta G_c = \Delta G_{0c} + \alpha F(E_2 - E_1) \tag{2.18}$$

ΔG_a and ΔG_c are the changes in Gibbs free energy for the anodic oxidation and cathodic reduction reactions, respectively. F is Faraday's constant, and $E_2 - E_1$ represents the change in electrode potential. The transfer coefficient, α, also known as the symmetry factor, varies between 0 and 1 and is related to the shape of the energy barrier for the reaction. It represents the fraction of the potential energy change that affects the activation energy of the oxidation and reduction processes. In other words, the transfer coefficient α determines how the potential change affects the activation energies of the oxidation and reduction processes, influencing the reaction rates. A higher α value means a greater impact on the reduction energy barrier, while a lower α value means a greater impact on the oxidation energy barrier. This relationship is crucial in understanding the kinetics of the electrochemical reaction and how changes in electrode potential can shift the balance between the forward and backward reactions.

According to Arrhenius Equation [f], the reaction rate constants can be presented respectively as

$$k_a = A_a \exp(- \triangle G_{0a}/RT) \tag{2.19}$$

$$k_c = A_c \exp(- \triangle G_{0c}/RT) \tag{2.20}$$

A_a and A_c are the pre-exponential factors which incorporate the frequency of collisions with the correct orientation for the reaction to occur. It is specific to each reaction and can be influenced by factors such as the nature of the reactants and the solvent. This exponential factor part accounts for the proportion of molecules in the reaction mixture that have kinetic energy equal to or greater than the activation energy at a give temperature T.

As introduced in section 2.1.5, when the electrode reaction reaches equilibrium, where the rates of oxidation and reduction are equal, the reaction rate constant at equilibrium is called the standard rate constant $k^0 = k_a = k_c$.

Combining these equations (from Equation 2.15 to Equation 2.19), the current-potential relationship is obtained as:

$$i = FAk^0\left[C_O(0,t)\exp(-\alpha F\Delta E) - C_R(0,t)\exp((1-\alpha)F\Delta E)\right] \tag{2.21}$$

---

[f] Arrhenius equation gives the dependence of the rate constant of a chemical reaction on the absolute temperature as $k = A\exp(-\frac{E_a}{RT})$

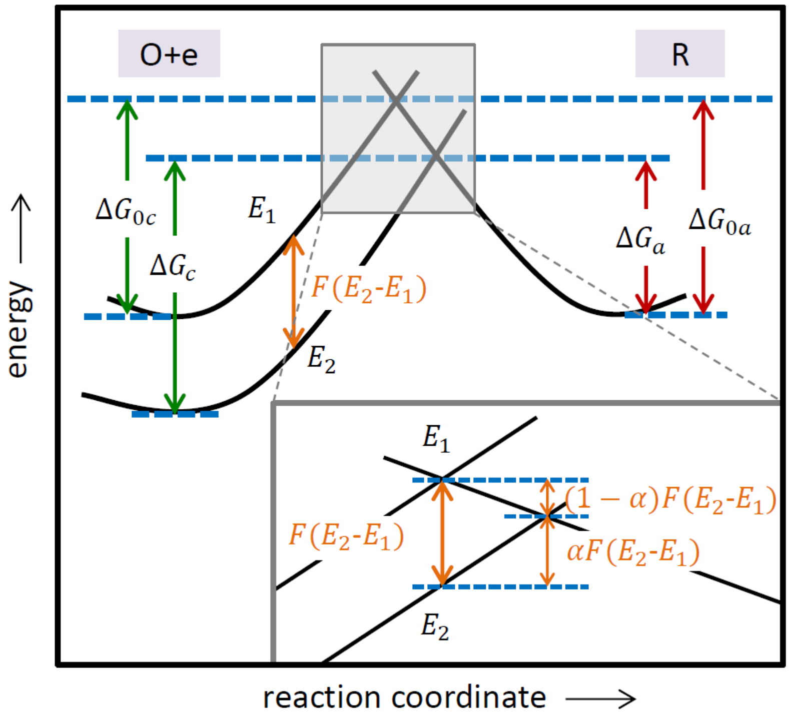

Figure 2.6: The variation of electrode potential changes the energy of oxidation and reduction reactions. There are potential energy curves, the left one is associated with the cathodic reaction and the right one is with the anodic reaction. The crossing point of these two curves is the transition state for the electron transfer process. When there is potential applied, the energy changes negatively from E_1 to E_2 and equals to $\Delta G = -nF\Delta E$, (n=1 in this representation figure). This energy difference is split into two parts, $\alpha F(E_2 - E_1)$ and $(1-\alpha)F(E_2 - E_1)$, where α is a symmetry factor and related to the fraction of energy barrier that is influenced by the electrode potential variation. Thus, the cathodic energy barrier (ΔG_c) decreases and the anodic energy variation (ΔG_a) increases, making the reaction more favorable for reduction.

This is the well-known Bulter-Volmer equation, which provides the fundamental kinetic relationship between current and electrode potential, describing the overall rate of an electrode reaction.

$$i = i_0 \exp\left(\frac{(1-\alpha)nF\eta}{RT}\right) - i_0 \exp\left(\frac{-\alpha nF\eta}{RT}\right) \tag{2.22}$$

This derivation links the electrochemical kinetics to the thermodynamic properties and energy barriers of the reactions.

Tafel slope

The Tafel slope is generally considered to be a fundamental characteristic of an electrochemical reaction, related to the reaction kinetics, particularly the charge transfer coefficient and the number of electrons involved in the rate-determining step.

The equation of Tafel slope is actually derived from the Bulter-Volmer equation in a simplified version, considering either the anodic reaction or the cathodic reaction:

$$j \approx j_0 \exp\left(\frac{\alpha_a nF\eta}{RT}\right) \tag{2.23}$$

Then taking the natural logarithm of both sides and converting to common logarithm by multiplying ln 10 (ln 10 = 2.303) :

$$\log j = \log j_0 + \frac{\alpha_a nF\eta}{2.303RT} \tag{2.24}$$

Then the tafel slope equation can be obtained as:

$$\eta = \frac{2.303RT}{\alpha_a nF} \log j - \frac{2.303RT}{\alpha_a nF} \log j_0 \tag{2.25}$$

simplified as:

$$\eta = b \log j + a \tag{2.26}$$

Now it is readily to see that tafel slope b describes the relationship between the overpotential η of an electrode reaction and the logarithm of the current density j, a is a constant related to the exchange current density j_0.

The Tafel slope is related to the transfer coefficient α and the number of electrons involved in the rate-determining step. For a one-electron transfer reaction, the Tafel slope is given by:

$$b = \frac{2.303RT}{\alpha F} \tag{2.27}$$

To measure the Tafel slope in experiment, normally a linear sweep voltammetry (LSV) or chronoamperometry experiment is performed to obtain a range of current densities at different overpotentials. Then plot the overpotential on the y axis and the logarithm of the current density on the x axis to identify the linear Tafel region. Then the slope of this linear region is the Tafel slope b. Finally, verify the measured slope for accuracy and reliability through repetition and comparison with known standards or theoretical predictions.

2.1.7 Mass transport

Mass transport phenomenon can happen within the one phase or between different multiple phases due to uneven concentrations. This phenomenon consists of three types of processes:diffusion, convection and migration, which exist together at the same time due to the different distance from mass to the interface. In different systems, the mass transfer process from the bulk solution to the electrode surface is completed through one or more of the above forms. The general equation of mass transfer flow is

$$J_j = -D_j \bigtriangledown C_j + C_j \nu - \frac{z_j F}{RT} D_j C_j \bigtriangledown \phi \tag{2.28}$$

The first term is diffusion, second term is convection and third is electromigration, which can be ignored,when the supporting electrolyte concentration is large enough.

Diffusion

A component transfers from a region of higher concentration to a region of lower concentration under a concentration gradient, which is called a diffusion phenomenon. Fick's law gives the functional relationship between flow and concentration, for an electrode reaction which the mass transfer is conducted by only diffusion, that is,

$$-J_O(0,t) = \frac{i}{nFA} = D_O[\frac{\partial C_O(x,t)}{\partial x}]_{x=0} \tag{2.29}$$

The amount of electrons transfer is proportional to the mass transfer of O by diffusion during the same time.

Convection

The forms of mass transfer by convection include natural convection and forced convection. The so-called natural convection refers to the convection caused by the density difference of the solution system due to the difference of local concentration and temperature. Forced convection is usually caused by external stirring, such as common electrochemical methods: rotating disk electrode (RDS) and rotating ring-disk electrode (RRDE).

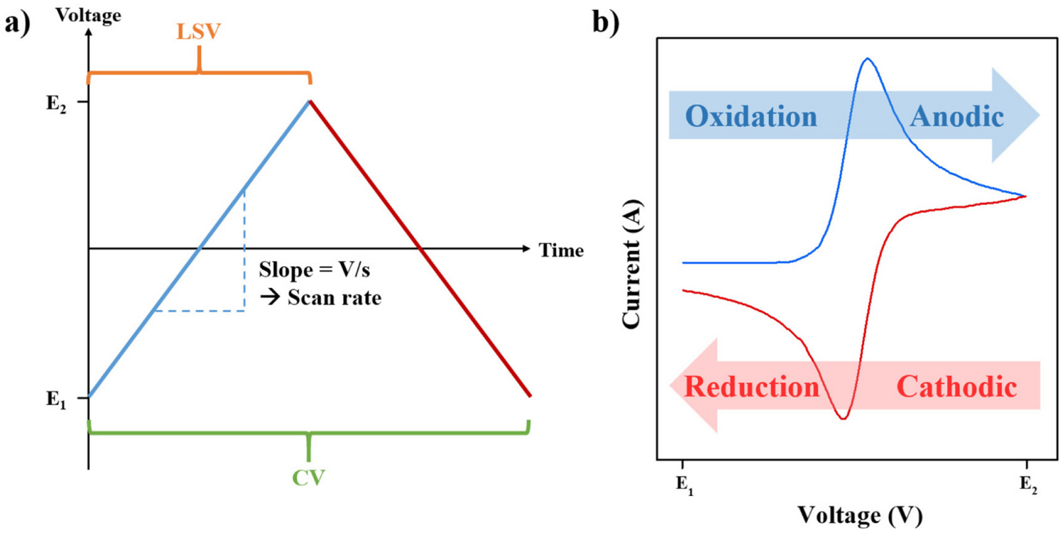

Figure 2.7: a) a typicle cyclic voltammogram scan, recording potential versus time; b) an ideal reversible redox reaction recording during cyclic voltammogram [87]

2.2 Electrochemical measurement techniques

2.2.1 Cyclic voltammetry

The cyclic voltammogram (CV) is a fundamental electrochemical technique widely employed for characterizing electrochemical systems. It offers a comprehensive understanding of both thermodynamic and kinetic properties.

In a typical CV experiment, as shown in Figure 2.7a, the applied potential is systematically varied in a back-and-forth manner between two defined limits (E_1, E_2), following a predetermined slope with respect to scan time, referred to as the scan rate. In result, the measured current is plotted against the applied potential as shown in Figure 2.7b.

During the forward anodic scan, where the potential increases from a lower to an upper value, the working electrode undergoes oxidation as it accepts electrons from the electrolyte. This leads to a progressive increase in oxidation current, culminating in a peak at a specific potential (blue curve in Figure 2.7 b). Conversely, during the backward scan, as the potential decreases, the direction of charge transfer reverses. Here, the working electrode releases electrons, undergoing reduction, thereby resulting in a reduction current (red curve in Figure 2.7 b) with a behavior mirroring that of oxidation current. The shape of the CV, the separation between oxidation and reduction peaks, and the peak asymmetry can provide insight and information about the mechanism of various electrochemical reactions.

Reaction reversibility

The symmetry of the oxidation and reduction peaks shows the reversibility of the overall electrochemical reaction. When the reduction process is electrochemically reversible, the distance between the anodic and cathodic peaks (peak to peak separation, $\triangle E_p$) can be used to estimate the reversibility of the redox reactions. The reversible process always refers to a fast electrode charge transfer kinetic process through the interface, as the Nernst equilibrium is established immediately when there is a change of the applied potential and the electrons transfer process follows the Nernst equation.

Conversely, when the rate of electron transfer at the interface lags behind the mass transfer processes occurring within the electrolyte, the electrode reaction becomes sluggish. Consequently, a greater overpotential is needed to facilitate the oxidation or reduction reaction, causing the corresponding peaks to shift to more positive or negative potentials. This results in an increased $\triangle E_p$, indicating a reduced reversibility and diminished efficiency in electron transfer kinetics.

2.2.2 Electrochemical impedance spectroscopy (EIS)

Electrochemical impedance spectroscopy (EIS) is a powerful tool in electrochemical analysis for characterization of the electrode-electrolyte interface. It can provide a way to distinguish distinct contributions from various processes occurring simultaneously on the electrode surface. EIS enables the investigation of an electrochemical system's properties through the lens of impedance, which can be viewed as the AC analog of resistance in a DC circuit.

In EIS, we consider the electrode-electrolyte interface and bulk electrolyte system as a "black box", observing the response of current flowing through this black box (the entire electrochemical system) to altering potential or current signals across a range of frequencies. This response is known as impedance, a term introduced by Oliver Heaviside in the 19th century, which evolved from resistance in DC circuits to AC situations [88]. By this method, the interface and bulk properties in the electrochemical system can be investigated through analogies to the circuit elements separating out the responses of different mechanisms in the whole system by the time constant of their response to the perturbation. To be more specific, the responses signal is always considered as the sum of two independent constituents, namely the response of the double layer (a capacitor component) and the response of the Faradaic reaction (a resistance component).

Applying an AC current or potential of different frequencies allows the separation of processes based on their different time scales. For example, if we set the frequency in the same time scale as the double layer capacitance and reaction rate control region, the diffusion effect on electric performance can not be measured in the current response as the concentration gradient has no time to develop.

EIS provides a way to link the electrochemical phenomena in the cell to the common behavior of circuit elements, which have different response to alternating electrical signals in the form of impedance. Three common electric circuit elements: resistance, inductor and capacitor, have different current response to an AC input and are often used to construct an equivalent analog circuit. Impedance can be described as the alternating current analog of resistance to a DC signal and it represents the output electrical signal to the AC input in a complex resistance.

The input AC signal is in the form sinusoidal function of time:

$$E(t) = E_0 \sin(\omega t) \tag{2.30}$$

where E is the potential at time t and E_0 is the potential amplitude of the input signal. The current response has an amplitude(I_0) and with a phase shift(φ):

$$I(t) = I_0 \sin(\omega t + \varphi) \tag{2.31}$$

According to Ohm's law, the impedance is the result of the E/I:

$$Z = \frac{E}{I} = \frac{E_0 \sin(\omega t)}{I_0 \sin(\omega t + \varphi)} = Z_0 \frac{\sin(\omega t)}{\sin(\omega t + \varphi)} \tag{2.32}$$

The real part represents the resistance which is in phase with the sinusoidal potential, and imaginary parts represent inductor or capacitor, which have a 90° phase shift from the potential. In an electrochemical system, the resistance contribution includes the charge transfer resistance, solution resistance and polarization resistance. Double layer capacitance can be modeled as a capacitor. Normally, the real case of the equivalent analogy circuit consists of some of those electronic components in a hybrid combination of parallel and series connections, and not only one equivalent circuit model fits.

The results of complex impedance can be plotted in Nyquist plots and Bode plots as shown in Figure 2.9. In Nyquist plot (Figure 2.9a), the real part (resistance) of the complex impedance

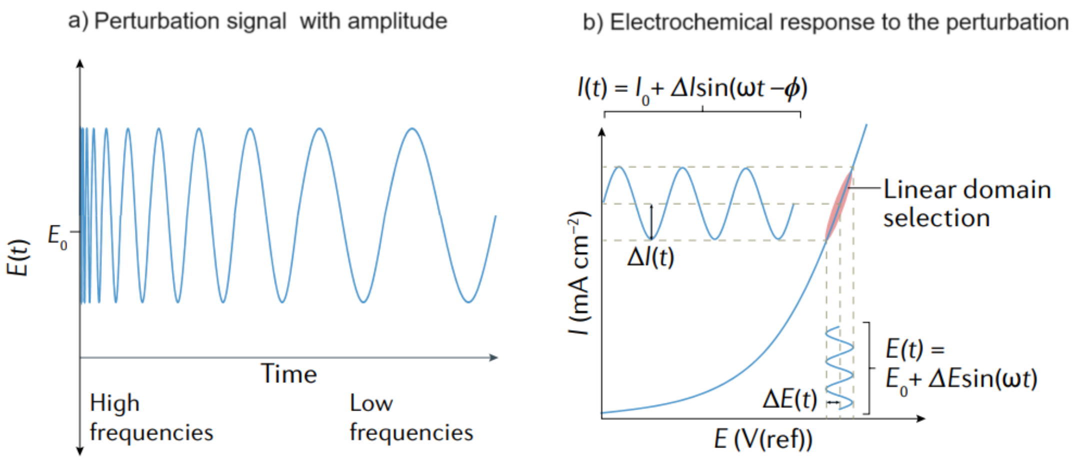

Figure 2.8: a) A periodic perturbation signal with a certain amplitude is applied between the WE and RE from high to low frequencies. b) The electrochemical response to this perturbation. The response to an input perturbation is a linear function of the single-frequency or multi-frequency input (Image: Nature Reviews Methods Primers [89])

is plotted on the x axis, and the imaginary part (capacitor) is plotted on the y axis. This plot typically consists of one or more semicircles, each corresponding to different electrochemical processes. However, the detailed frequency information cannot be read from Nyquist plots, only high or low frequency region can be estimated. In the high-frequency region, the imaginary part approaches zero (the left part of the x axis), and the impedance is dominated by the solution resistance. This point, located at the intersection of the plot with the x-axis, represents the lowest impedance value and indicates that the capacitive elements in the system are effectively "short-circuited" due to the rapid oscillations of the AC signal. At lower frequencies, the plot usually exhibits a larger imaginary component (the right region of the x axis), corresponding to processes such as charge transfer resistance and diffusion.

In Bode plot (Figure 2.9b), the log of frequency is plotted as x axis, and the amplitude of impedance and the phase shift between potential perturbation and current response are plotted as y axis. It is normal used to help an identification of capacitive and inductive characteristics. For example, a phase shift of 0° indicates purely resistive behavior, while shifts of +90° and -90° indicate capacitive and inductive behaviors, respectively.

2.2.3 AC voltammetry

AC voltammetry is another sophisticated analytical technique derived from AC electrochemistry. This technique involves applying a sinusoidally oscillating voltage with a certain amplitude and frequency to an electrochemical cell and measuring the current response. Normally, the AC voltage is superimposed on a steady DC signal or a DC voltage sweep, as illustrated in Figure 2.10, which shows a voltammetric signal with steps under an AC perturbation.

By varying the frequency of the applied AC signal, AC voltammetry allows for the investigation of electrochemical processes across different time scales. For instance, electrochemical double-layer charging and discharging are rapid processes that can be effectively studied at high frequencies. In contrast, diffusion-controlled processes, which occur more slowly, are better examined at low frequencies. This frequency-dependent analysis enables the separation and detailed study of different electrochemical phenomena, which is not feasible with conventional CV.

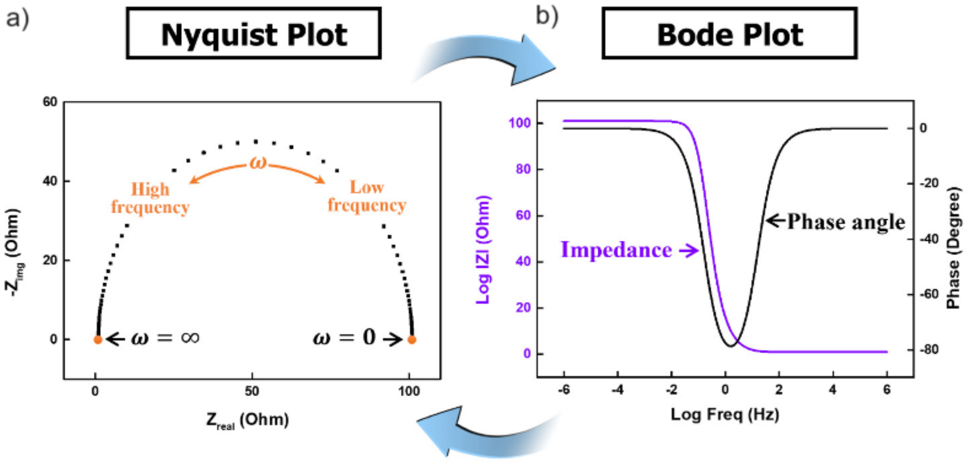

Figure 2.9: a) A Nyquist plot showing the negative imaginary impedance versus the real part of the impedance. b) Bode plots show how the phase shift and magnitude of impedance changes with applied frequency. These two classic impedance graphs are switchable. (Image: Journal of Electrochemical Science and Technology [90])

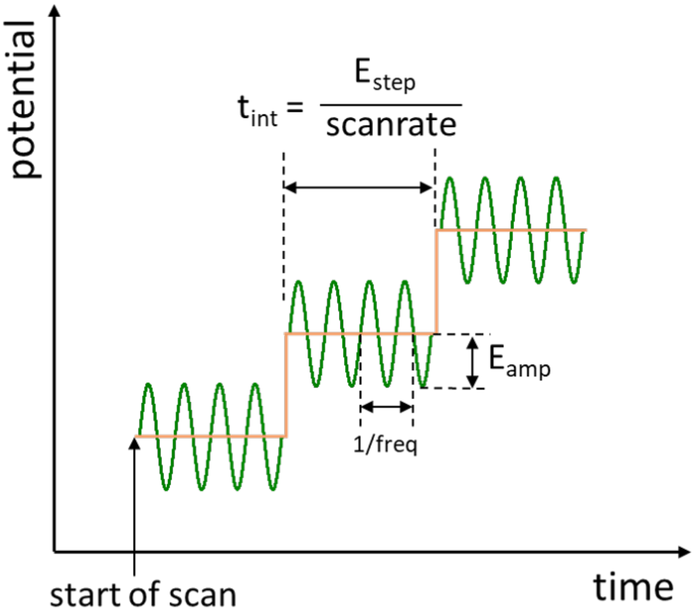

Figure 2.10: A schematic representation of AC volatmmetry: a potential step scan with a superimposed sine wave with a certain small amplitude and frequency.

2.3 Fundamental understanding of surface strain in a nanomaterial

Elastic strain is one of the most important fundamental physical properties in materials science study. Strain is typically expressed as a dimensionless quantity, represented by the Greek letter epsilon (ε), and is calculated as the change in length or dimension divided by the original length or dimension. In the elastic regime, strain can be understood as the change in atomic distances ($\Delta d/d_0$) or bond lengths within a material when subjected to external forces or stresses. It can be positive (tensile strain) when the material is stretched or elongated, or negative (compressive strain) when the material is compressed or shortened, as shown in the top row of Figure 2.11. It is an important aspect of nanomaterials that significantly influences their properties and behaviors.

Normally nanomaterials have a high surface-to-volume ratio compared to bulk materials. As a result, the influence of atoms at the surface experiencing different forces and bonding environments compared to those in the interior cannot be neglected. This leads to surface-specific phenomena, including surface strain. From strain engineering perspective, there are two types of strain, namely intrinsic strain and external applied strain. Intrinsic strain is the change of material lattice constant caused by bending, twisting, wrinkling and other factors. The most common surface modified materials, such as those obtained by chemical vapor deposition (CVD), suffer from in-plane strain due to lattice mismatch with the substrate and differences in thermal expansion coefficients during the growth process. Therefore, two-dimensional materials with different strain levels can be obtained by changing the type or crystal plane of the growth substrate. The external applied strain can be roughly divided into mechanical methods and chemical methods, in terms of alloying, doping, phase engineering etc. When a material with atomic level thickness is placed on a flexible substrate, the deformation of substrate can be transferred to the attached thin film material. Relative slip between substrate and thin film material can be overcome by metal or polymer coating. Such strain can be found in core-shell structured catalysts, as the lattice parameter is inevitably different from the core and shell material, and this lattice mismatch is related to many factors, such as the shell thickness, the epitaxial growth way and the size and shape of the core material, as shown in the second row of Figure 2.11, the shape of core part can be particle, rod, wire, cube, sheet, etc.

2.4 Coupling between electrode surface mechanics and reactivity

2.4.1 Thermodynamic description of electrode surface

Considering to increase a certain surface area, the contribution of energy from liquid and solid are different as there is the coherency and the presence of shear stresses in the solid, consequently the extra surface in liquid comes from only adding more atoms to the surface. This portion of energy is well known as the concept-surface tension (γ) [92, 93]. However, the contribution of this energy in a solid is more complex due to the presence of atomic bonds. When there is new surface formation, in solid, the surface free energy contribution arises from two aspects: i) **Plastic deformation**: adding surface atoms within the constant surface atomic distance, which is the same behavior as in liquid, so the surface changes in a plastic way; ii) **Elastic strain**: the number of surface atoms remains constant, but the interatomic distances change with elastic strain, this part of surface energy is generated by the surface stress. These two fundamental concepts must be considered carefully when studying the thermodynamics and mechanics of solid surfaces.

In thermodynamic theories, for solid-liquid interface, the variation in surface free energy is proportional to the variation in surface area:

$$\Delta G^{sl} = \gamma^{sl} \Delta A \tag{2.33}$$

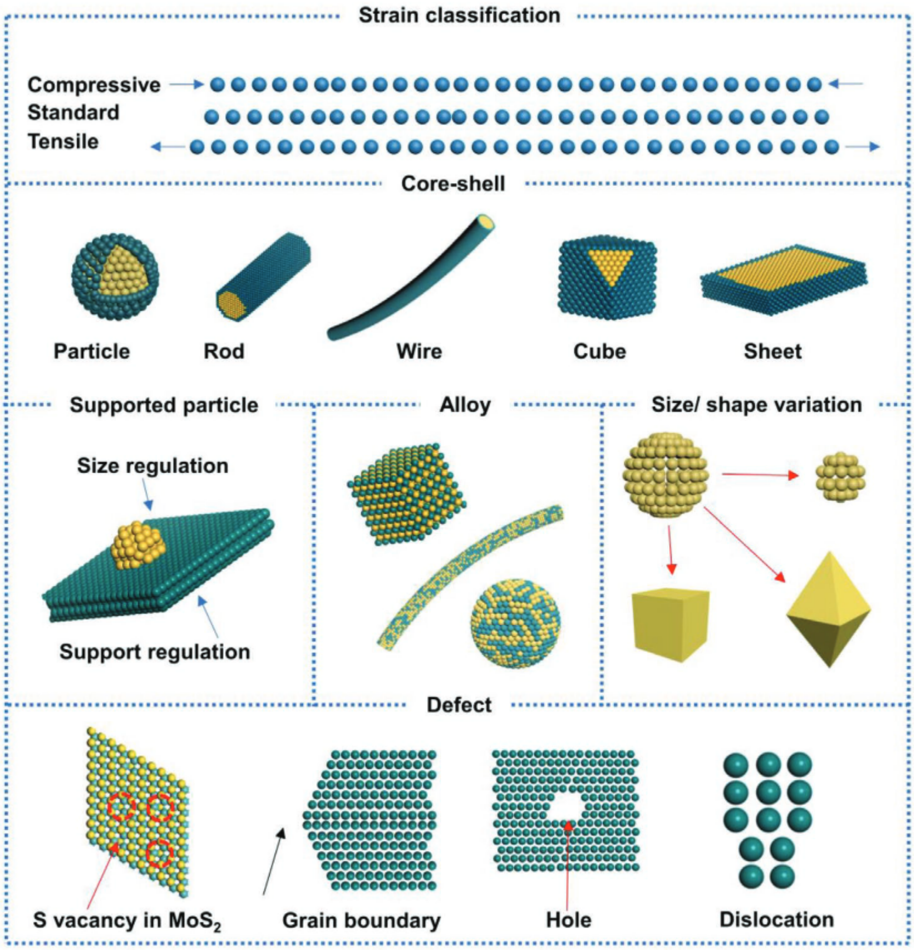

Figure 2.11: A schematic diagram of different types of strain in material manufacture reported in recent studies and [91]

The original variation of surface area is from the combination of two area changing methods giving two surface area definitions: solid liquid interface Lagrangian area A_L[g] and physical area A. The solid-liquid surface tension (γ^{sl}) is defined as to describe the reversible work per unit area to form extra area, while the surface stress is referred to expand interatomic distance (strain) on the already existing surface area. With respect to the surface free energy contribution from elastic strain, the derivative of surface tension is introduced as surface stress, $f = \partial\gamma/\partial e$. In terms of surface stress, this part of surface free energy is

$$\Delta G^{sl} = A\Delta\gamma^{sl} = A\frac{\partial\gamma}{\partial e}e = f^{sl}Ae \tag{2.34}$$

It is important to note that at a solid surface, the surface stress is the derivative of the surface tension with respect to tangential strain, while for liquid surface, the surface tension is equal to surface stress as the strain of a liquid surface does not exist. In other words, surface tension is a scalar quantity and always remains a positive value, while surface stress is a tensor, only when a solid electrode surface is isotropic, the surface stress can be simplified as a scalar.

2.4.2 Surface stress variation during adsorption

During an adsorption process, the change of the electrode surface charge density (q) or the absorbates density give rise to a distance change between surface atoms which can be balanced by the underlying bulk, but altering the electrode surface stress state. In other words, the electrode surface stress changes during adsorption of ions or electric charging process, as shown in the middle row of Figure 2.12, depending on the adsorbed ion, which can show either dilatation or contraction, giving rise to either compressive or tensile eigenstress accordingly and exhibit curvature in macroscale (bottom row of Figure 2.12).

This overall change in surface stress can be measured using the cantilever bending method. When the electrode potential varies, the surface state changes accordingly due to different adsorbates on the surface, causing the cantilever wafer to bend due to the increase (compressive surface strain) or decrease (tensile surface strain) in the distance between surface atoms. This curvature change of the wafer sample, according to Stoneys Equation [96], can be translated into surface stress variation (more details of this cantilever bending experiment introduction can be found in Chapter 3.4).

An example of experimental data is shown as Figure 2.13. This example demonstrates the cyclic voltammogram of a sputtered gold thin film in the double layer region, namely the surface charging and discharging area. During cyclic potential scans, simultaneously the curvature of the wafer bending was measured *in-situ*. The surface stress variation Δf was derived from this curvature using Stoneys equation with respect to surface superficial charge density, which is the integration of the current density. The surface tension variation $\Delta\gamma$ shown in Figure 2.13b is the result of computation of surface superficial charge q according to Lippmanns equation [97]:

$$d\gamma = -qdE \tag{2.35}$$

$$\Delta\gamma(E) = \gamma(E) - \gamma_0 \tag{2.36}$$

Figure 2.13b shows the surface stress and surface tension variation of the gold electrode versus superficial charge q during cyclic voltammetric scan. It is readily seen a clear difference between surface stress and surface tension of a solid surface in perspective of experimental measurements. The surface tension exhibits a maximum value at the potential of zero charge as we introduced

---

[g] The Lagrangian area is used to measure the surface area in a stable state regardless of surface strain during elastic deformation [94], namely as a reference state. Stretching of the surface in an elastic way does not increase A_L, but adding more atoms to the surface with a certain interatomic distance does. The relation between A_L and physical area A is $A = A_L(1 + e)$.

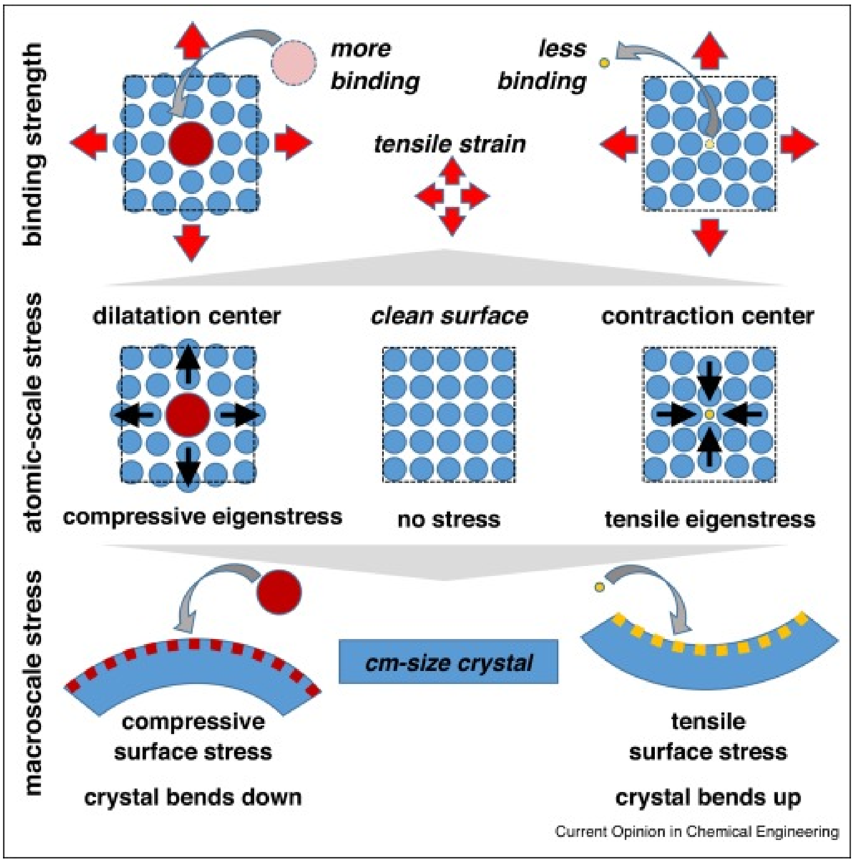

Figure 2.12: The experimental macroscale behaviors resulting from atomic scale mechanical interactions [95]. When an atom is adsorbed onto a clean surface, it can act as either a dilatation center or a contraction center, depending on whether it induces compressive or tensile eigenstress, respectively. On the macroscale, this results in the bending of a thin film, either compressive or tensile stress. And, under external tensile strain, the binding interactions between the surface and the adsorbed atoms are altered: a stronger binding to the dilatation center (where atoms are more closely packed), while a weaker binding to the contraction center (where atoms are more widely spaced). Under external compressive strain, the behavior is reversed.

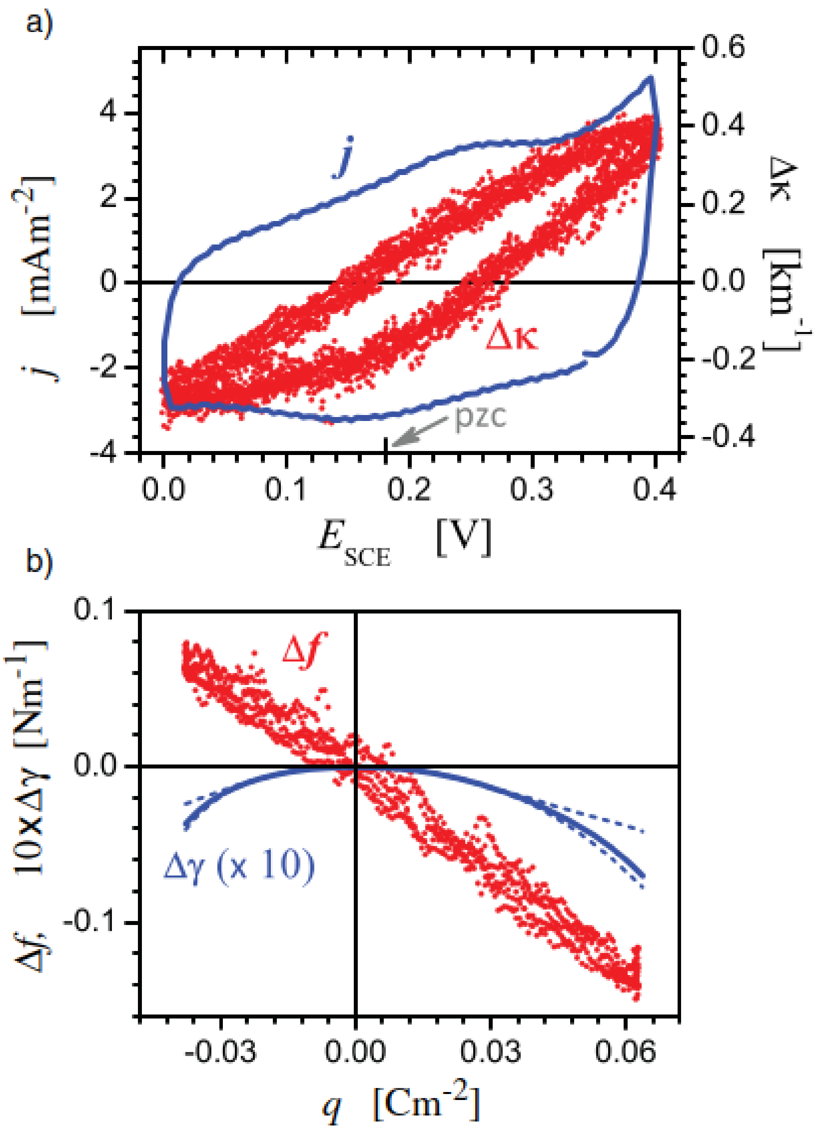

Figure 2.13: Experiment data of cantilever bending experiment from previous work of M. Smetanin [68]. a) Cyclic voltammogram in the region of double layer on sputtered gold surface of cantilever wafer, the scan rate was 10 mV/s, the red dots is the wafer bending curvature $\Delta\kappa$ which was measured simultaneously during cyclic scans. b) The surface stress variation, Δf, was calculated from wafer bending curvature $\Delta\kappa$ according to Stoneys equation. The charge Δq as x-axis is integrated from current $j(E)$ with respect to electrode potential E in a). The surface tension in blue line with 10 times magnification is computed from $j(E)$ through Lippmanns equation. The blue dashed line indicates the proximate error from the calculation of Lippenmann equation.

before, which is a clear distinguishable characteristic from surface stress. Any change of the surface charges, no matter positively or negatively charged, can only induce a quadratic decrease of the surface tension with q, whereas the surface stress f varies linearly with q, and the slope of the surface stress variation with q is the electrocapillary coupling coefficient $\varsigma_q(E)$ [98].

2.4.3 Strain effect on surface adsorption

Strain effects on adsorption energy are crucial for understanding and controlling surface interactions. During adsorption or desorption processes, as introduced in the last section, the surface stress state changes accordingly. At the mean time, when the surface strain state changes, the surface adsorption properties will also change. This coupling effect reveals the interconnected nature of surface electrochemical and mechanical properties.

Applying strain to a surface alters the distances between surface atoms, which can either enhance or inhibit the adsorption of molecules by altering the adsorption enthalpies or electrode potential [43, 45, 99–101], hence, promote or hinder the electrocatalytic reactions occuring on the electrode surface. To be more specific, when the surface is under tensile strain, as shown in Figure 2.12 top row, the bonding between the adsorbed ion and the surrounding atoms depends on not only the existing applied strain state, but also the eigenstress caused by the adsorbed ion itself, thus showing either a stronger or weaker binding to the surface. The real situation of the strain effect on adsorption are more complex than d-band model prediction, thus requires quantitative studies for accurate prediction from experiments.

2.4.4 Maxwell relations and potential-strain coupling coefficient

Considering a solid electrode immersing in a homogeneous electrolyte, the interfacial free energy, ψ, is taken to generate a fundamental function of the interfacial charge density, q, and surface tangential strain, e, together with their energy-conjugate variables, which is electrode potential, E, and surface stress,f. Here, we assume that during an ideal electrosorption process, the surface charge transfer happens by the pure capacitively adsorbed ions on the solid-electrolyte interface. So the contribution of the surface free energy comes from the mechanical work of surface stress (changing the surface atom distance in terms of surface strain e) and electrical work of electrode potential (adsorption induced charge density variation q):

$$d\psi = Edq + fde \tag{2.37}$$

An analogous situation on solid-gas surface with such appropriate constitutive assumption for the surface energy variation during the adsorption can be expressed and the free energy change of the solid-gas interface (ψ^{sg}) is

$$d\psi^{sg} = \mu d\mathit{\Gamma} + fde \tag{2.38}$$

μ is the chemical potential of the adsorbing species in the gas phase and Γ is the superficial excess–the difference between the number of ions at the surface compared to in the bulk solution.

Maxwell equation was first reported by Gokhshtein [100, 102] half century ago. Maxwell relation links mechanics and electrochemistry and enable the electrocapillary coupling coefficient ς to be the descriptor to quantify this phenomenon from both practical experiment and numerical simulation. This concept of Maxwell equation was then confirmed by experiments with more detailed numerical magnitude from recent work of Weissmueller's group [69, 103]. They verified this material parameter can be determined empirically from experiment as a state function of electrode potential $\varsigma(E)$.

It specifies the correlation between surface stress to surface charge density and electrode potential to surface strain of the electrode-electrolyte interface by:

$$\varsigma = \left.\frac{dE}{de}\right|_q = \left.\frac{df}{dq}\right|_e \tag{2.39}$$

The electrocapillary coupling coefficient ς is the core parameter in this filed, which is also called the potential-strain coupling coefficient. From this equation, it is readily to see that the response of potential variation to external elastic strain at constant charge is numerically equal to the surface stress variation to interface charge transfer at constant surface strain with opposite sign.

Also, similarly the relationship on the solid-gas interface:

$$\zeta = \left.\frac{d\mu}{de}\right|_{\Gamma} = \left.\frac{df}{d\Gamma}\right|_{e} \tag{2.40}$$

In the double layer region of electrode-electrolyte interface, when no specific adsorption occurs, the behavior of the electrode-electrolyte interface is purely capacitive. That means the interface stores energy in the electric field of the double layer without any chemical or physical adsorption interactions complicating the system. Then the charge q is proportional to potential E, $q = C \cdot E$, for the whole interface acts as an ideal capacitor. When there is adsorption on the surface, the adsorbates contribute to the surface charge and affect the potential distribution across the interface. The variation of electronic charge on the surface is exclusively related to the variation of superficial excess, $\Delta\Gamma$. In other words, with adsorption occurring on the interface between electrode-electrolyte, the variation in the electronic charge on the electrode surface is no longer just a function of the potential E, but also related to the change in Γ, which links the charge density and the superficial excess of adsorbate via

$$dq = -zFd\Gamma \tag{2.41}$$

where the F is Faraday's constant and z is the valency of the adsorbates from electrolyte. This also links the electrode potential E and the chemical potential μ of the molecules in electrolyte

$$d\mu = -zFdE \tag{2.42}$$

From Langmuir isotherm model

$$\mu = \mu_0 + \Delta h_{\text{ads}} + RT\ln[\theta/(1-\theta)] \tag{2.43}$$

The chemical potential depends on the adsorption enthalpy Δh_{ads} , the chemical potential at reference state μ_0, and surface overage $\theta = \Gamma/\Gamma_{max}$, which is

$$\theta = (1 + \exp\frac{\mu - \mu_0 - \Delta h_{\text{ads}}}{RT})^{-1} \tag{2.44}$$

At a certain coverage, the adsorbate enthalpy stays constant. When we link to the surface adsorbate enthalpy to strain via the surface coverage, Γ sites per area, the function of the adsorbate enthalpy with strain can be obtained:

$$\zeta = \frac{d\Delta h_{\text{ads}}}{de} = \left.\frac{d\mu}{de}\right|_{\Gamma} \tag{2.45}$$

Now we take the first derivative of Equation 2.42 by strain, as required by Maxwell relation mentioned before, the relation between electrocapillary coupling coefficient and adsorbate enthalpy is inspected

$$\varsigma = -\frac{1}{ZF}\frac{d\Delta h_{\text{ads}}}{de} \tag{2.46}$$

From DFT study, the number of ς is evaluated to be -1.86V [104] on gold surface, which is in agreement with experimental data [68] and varies with the surface orientation.

2.4.5 Current-strain coupling response

During an electrochemical reaction process, the overall net current consists of both capacitive current (non-Faraday current or adsorption current) and reaction current (Faraday current) as introduced in chapter 2.1.2. For the non-faradic process, the charge density of both capacitive and pseudocapacitive processes is considered to store charges on the electrode interface and link to the excess of ions. We assume that the electrode is ideally polarized at equilibrium, the capacitance at constant strain is

$$c = \left.\frac{dq}{dE}\right|_{e} \tag{2.47}$$

and from the electrocapillary coupling coefficient Equation 2.39, according to [105]($\left.\frac{dx}{dy}\right|_{z} = -\left.\frac{dx}{dz}\right|_{y}\left.\frac{dz}{dy}\right|_{x}$), the charge variation with respect to strain variation at constant potential [106] is

$$\left.\frac{dq}{de}\right|_{E} = -\left.\frac{dq}{dE}\right|_{e}\left.\frac{dE}{de}\right|_{q} = -\varsigma c \tag{2.48}$$

Either charge or potential is held constant during the cyclic strain experiment on the polarizable electrodes near equilibrium. As the strain modulation with strain frequency is a sinusoidal function:

$$E = \hat{e}\sin(\omega t) \tag{2.49}$$

According to Equation 2.49, the current modulation at constant potential

$$j = -\varsigma c \omega \hat{e}\cos(\omega t) \tag{2.50}$$

So the whole system contains two current contributions is

$$j = \frac{dq}{dt} + j^{F}(E, e) \tag{2.51}$$

The first term of Eq 2.51 is the pseudo-capacitive current, and the second term responds the contributions from Faraday current. Now we assume that with strain modulation, the j^{F} changes much faster than the potential and strain cycles to reach to a new steady transitional state, then the reaction current, with respect to small external strain, is the sum of basic reaction current and strain modulated reaction current:

$$j^{F}(E, e) = j_{0}^{F}(E) + \iota e \tag{2.52}$$

ι is current-strain coupling coefficient, which is used to describe the Faraday current variation with strain at constant potential:

$$\iota = \left.\frac{dj^{F}}{de}\right|_{E} \tag{2.53}$$

An alternative current-strain coupling coefficient λ is also of interest to be investigated to measure the relative variation of the Faraday current[h]::

$$\lambda = \frac{1}{j^{F}}\left.\frac{dj^{F}}{de}\right|_{E} \tag{2.54}$$

$$j = j_{0}^{\mathrm{F}} - \varsigma c \omega \hat{e}\cos(\omega t) + \iota \hat{e}\sin(\omega t). \tag{2.55}$$

In this equation, the first term on the right-hand side of Equation (2.55) is the faradic reaction current at $e = 0$, the second term originates from pseudocapacitive processes, and the third term

---

[h] Recall that $d\ln x = x^{-1}\,dx$.

is the modulated reaction current. The lock-in amplifier of the DECMA experiment takes the second and third term as the imaginary and real parts, respectively, of the current modulation amplitude. We here refer to these signals, normalized by $\hat{e}$, as $\hat{\jmath}_{\mathrm{im}}$ and $\hat{\jmath}_{\mathrm{re}}$, respectively, and note that Equation 2.55 suggests

$$-\hat{\jmath}_{\mathrm{im}} = \varsigma c\omega \qquad \text{and} \qquad \hat{\jmath}_{\mathrm{re}} = \iota\,, \tag{2.56}$$

It is readily seen that the pseudocapacitive current is out-phase by a shift of 90° to the strain scales with strain frequency, whereas the reaction current is in-phase with strain and independent from strain frequency. This provide an important indication for the later data analysis to differentiate the two current contributions.

2.4.6 Resistance effect on the current-strain coupling response

In an electrochemical cell system, the existence of resistance is a natural fact as introduced in Section 2.1.3. This resistance affects not only the applied potential but also, in our case, the current-strain coupling coefficients.

In terms of the quantities defined above, when considering the effect from R in the electrochemical system, it is of necessary to stress out the relation between the experimental signature, namely λ_{app}, of the current-strain coupling, and the "true" (intrinsic) coupling parameter, λ. The apparent electrode potential, E_{app}, at a constant value is applied from the potentiostat in the DECMA setup. We allow for a substantial resistive potential drop in the electric conduction path from the reference electrode through the working electrode to the potentiostat. That potential drop accounts for electric resistance of two separate origins – firstly, the resistance in the solution between the RE and the WE ("uncompensated solution resistance", R_{sol}), and secondly, with attention to thin-film working electrodes, the electric resistance within the thin film, R_{film}:

$$R(e) = R_{\mathrm{sol}} + R_{\mathrm{film}}(e) \tag{2.57}$$

The true value, E, of the electrode potential may then differ significantly from E_{app}. Inasmuch as the electrode current, I, varies with e, we must also admit that the difference, $E - E_{\mathrm{app}}$, may vary as a function of e,

$$E_{\mathrm{app}}(E,e) = E + J(E,e)R(e) \tag{2.58}$$

With a constitutive assumption for the electrode current, J:

$$J = J(E,e) \tag{2.59}$$

That variation would then feed into the measurement of the current-strain coupling parameter, λ. In other words, the experimental, apparent value, λ_{app}, would differ from the true, intrinsic coupling parameter λ. Here, we derive a relation between λ and λ_{app} that allows the effect of the uncompensated resistance to be estimated and corrected, according to Eq 2.54, with $j = J/A$ the current density and A the area of the electrode. The apparent value of λ, as supplied by the experiment when the potential drop in the solution is ignored, is:

$$\lambda_{\mathrm{app}} = \left.\frac{d\ln j}{de}\right|_{E_{\mathrm{app}}} \tag{2.60}$$

The true value of a current-potential slope parameter, which is analogous to Tafel slope, but describe the current variation with a potential perturbance is:

$$\tau = \left.\frac{d\ln j}{dE}\right|_{e} \tag{2.61}$$

The apparent value of that parameter in an experiment that ignores the solution resistance is:

$$\tau_{\mathrm{app}} = \left.\frac{d\ln j}{dE_{\mathrm{app}}}\right|_{e} \tag{2.62}$$

The sensitivity parameter s describes the strain dependence of the resistance of a thin film according to

$$s = \frac{d \ln R_{\text{film}}}{de} \tag{2.63}$$

We take the film (the electrode) to be elastically isotropic and attached to a much thicker and also isotropic planar substrate. Poisson's ratios for the film and the substrate are ν_F and ν_S, respectively. The DECMA experiment works with a uniaxial load on the substrate, and the resulting biaxial strain in the substrate plane is imposed on the film. Furthermore, the film is stress-free along the direction normal to the substrate plane. The volume-specific resistivity can be assumed independent of the elastic strain (this assumption underlies the design of resistive strain gauges, widely applied in engineering technology and research), and the change in resistance then follows simply from the geometry change upon straining of the film. By virtue of Hooke's law in its tensor form, it is then readily shown that

$$s = \frac{1 + \nu_S + (1 - 2\nu_F)}{(1 - \nu_S)(1 - \nu_F)} \tag{2.64}$$

Starting with the definition of τ_{app} as given in Eq 2.4.6, we can apply the chain rule:

$$\tau_{\text{app}} = \frac{d \ln j}{dE_{\text{app}}}\bigg|_e = \frac{d \ln j}{dE}\bigg|_e \frac{dE}{dE_{\text{app}}}\bigg|_e = \tau \frac{dE}{dE_{\text{app}}}\bigg|_e \tag{2.65}$$

Now work out the last term on the right-hand side of the rightmost equation. By Eq 2.58 and Eq 2.61, we have

$$\frac{dE_{\text{app}}}{dE}\bigg|_e = 1 + R\frac{dJ}{dE}\bigg|_e = 1 + RJ\frac{d \ln j}{dE}\bigg|_e = 1 + RJ\tau. \tag{2.66}$$

By using this result along with Equation 2.65, it is readily found that

$$\tau_{\text{app}} = \frac{\tau}{1 + RJ\tau}. \tag{2.67}$$

Thus, the intrinsic value of τ is

$$\tau = \frac{\tau_{\text{app}}}{(1 - RJ\tau_{\text{app}})} \tag{2.68}$$

Now, we aim to evaluate the variation in current when the electrode is strained while the potentiostat controls the apparent electrode potential at a constant value. To achieve this, we consider a small variation, δe, in strain and model the consequences in terms of a two-step process. Step 1, the electrode is strained at a constant value of the true electrode potential E. That will change both the current j and, thereby, the apparent electrode potential E_{app}. The variations in current, resistance, and potential are as follows:

$$\delta_1 J = J\lambda\delta e, \tag{2.69}$$

$$\delta_1 R = sR_{\text{film}}\delta e, \tag{2.70}$$

$$\begin{aligned}\delta_1 E_{\text{app}} &= \delta_1(RJ) \\ &= R\delta_1 J + J\delta_1 R \\ &= J(\lambda R + sR_{\text{film}})\delta e.\end{aligned} \tag{2.71}$$

Next, in Step 2, the strain remains constant while E_{app} is adjusted back by $\delta_2 E_{\text{app}} = -\delta_1 E_{\text{app}}$. This leads to the current variation

$$\delta_2 J = -J\tau_{\text{app}}\delta_1 E_{\text{app}} = -J^2(\lambda R + sR_{\text{film}})\tau_{\text{app}}\delta e. \tag{2.72}$$

By adding up the current variations, $\delta J = \delta_1 J + \delta_2 J$, dividing by the strain variation δe, taking the limit of infinitesimal strain, and accounting for Equation 2.72, we find that

$$\frac{dJ}{de}\bigg|_{E_{\text{app}}} = J\lambda - J^2\tau_{\text{app}}(\lambda R + sR_{\text{film}}). \tag{2.73}$$

or equivalently

$$\left.\frac{d\ln j}{de}\right|_{E_{\text{app}}} = \lambda - \tau_{\text{app}} J(\lambda R + sR_{\text{film}}). \tag{2.74}$$

and then (in view of 2.67)

$$\left.\frac{d\ln j}{de}\right|_{E_{\text{app}}} = \lambda_{\text{app}} = \lambda\frac{1}{1 + \tau RJ - s\tau R_{\text{film}} J(1 + \tau RJ)}. \tag{2.75}$$

In other words,

$$\lambda = \lambda_{\text{app}}(1 + \tau RJ) + \tau s R_{\text{film}} J. \tag{2.76}$$

2.5 Heterogeneous electrocatalysis

2.5.1 Methanol oxidation reaction (MOR)

Mechanism and possible pathways of MOR in alkaline environment

The mechanism of methanol oxidation on Pt surface has been extensively studied over decades. However, until today, there is no consistent conclusion regarding the exact mechanism of methanol oxidation on Pt. Methanol oxidation is a complex multi-step reaction, and the specific mechanism may vary depending on the experimental conditions, such as pH [107], concentration of methanol [108], temperature [109, 110], as well as the nature of the electrode surface state [111, 112].

Here, as a brief summary of the reaction mechanism, all the main pathways and possible intermediates of methanol oxidation are collected from literature [110, 113–117] and shown as Figure 2.14 and list with their chemical names as Table2.5.1.

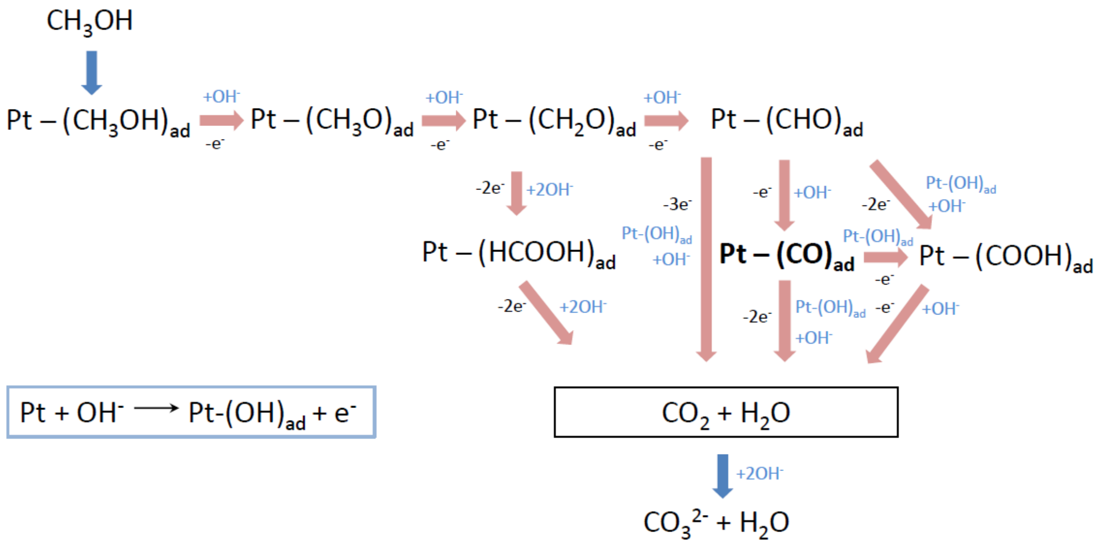

Figure 2.14: detailed methanol oxidation reaction pathways in alkaline solution. The red arrow represents the processes with electrons transfer and blue arrows represent the processes without electronics transfer, such as weak adsorption\desorption or solvation process.

Condensed formula	Chemical names
H_3COH	methanol
H_2COH	hydroxymethyl
HCOH	hydroxymethylene
COH	hydroxy
CO	carbon monoxide
CO_2	carbon dioxide
CH_3O	methoxy
CH_2O	formaldehyde
HCO	formyl
HCOOH	formic acid
HCOH	dihydroxymethylene
$C(OH)_2$	dihydroxycarbene
$HC(OH)_2$	hydrated formaldehyde
H_2COOH	methanediolate

Methanol oxidation reaction occurring on Pt electrode performs more readily in alkaline than in acid solution with an increasing kinetics [108, 118, 119]. The overall reaction formula of methanol oxidation in alkaline environment can be written as Formula 2.77, with totally six electrons transfer during the process.

$$CH_3OH + 6OH^- \longrightarrow CO_2 + 5H_2O + 6e^- \tag{2.77}$$

From the total reaction formula it can be seen that the prerequisite of methanol oxidation is the OH^-, either in the electrolyte environment or adsorbed on Pt surface above a certain potential. That is also the reason why pH of the electrolyte plays an important role [107, 108, 110].

$$Pt + OH^- \longrightarrow Pt\text{–}OH_{ad} + e^- \tag{2.78}$$

Reaction 2.78 with one electron transfer is the initial stage of Pt surface oxidation and followed by Pt oxide formation at higher potential region [120–122]. These $Pt-OH_{ad}$ sites are active and can facilitate methanol oxidation during the entire methanol oxidation process. The coverage of $Pt-OH_{ad}$ as well as its oxide are governed by the applied potential. With increasing overpotential, $Pt-OH_{ad}$ is oxidized further into Pt oxide (PtO) with additional one electronic transfer as Formula.2.79. When the surface active sites are blocked by a certain coverage of Pt oxide at high anodic potential, methanol oxidation is inhibited.

$$Pt\text{–}OH_{ad} + OH^- \longrightarrow PtO + H_2O + e^- \tag{2.79}$$

The initial stage of methanol adsorption is the process of methanol dehydrogenation on Pt surface as Reaction 2.80, to form adsorbed methoxyl then dehydrogenate from the methyl. The methanol molecules adsorption has been proved to take place in the region of hydrogen under potential deposition (HUPD) region. Since for methanol adsorption, which is less competitive compared to hydrogen adsorption on the surface, noticeable adsorption of methanol begins when there are free spots released by hydrogen desorption. The alkaline media is highly reactive towards facilitating the hydrogen removing process. All possible theoretical dehydrogenation processes of methanol on Pt surface are listed as following

$$Pt + CH_3OH \longrightarrow Pt\text{–}(CH_3OH)_{ad} \tag{2.80}$$

$$Pt\text{–}(CH_3OH)_{ad} + OH^- \longrightarrow Pt\text{–}(CH_3O)_{ad} + H_2O + e^- \tag{2.81}$$

$$Pt\text{–}(CH_3O)_{ad} + OH^- \longrightarrow Pt\text{–}(CH_2O)_{ad} + H_2O + e^- \tag{2.82}$$

$$\mathrm{Pt{-}(CH_2O)_{ad} + OH^- \longrightarrow Pt{-}(CHO)_{ad} + H_2O + e^-} \tag{2.83}$$

Several intermediates, such as formaldehyde (HCHO), formic acid (HCOOH), formate ($HCOO^-$), carbon monoxide (CO) and carbon dioxide (CO_2), are formed during this process and can be either soluble and diffuse into electrolyte or further oxidized. The formation of several carbonaceous intermediates adds complexity to the mechanism of this electrocatalytic reaction. The presence of these intermediate adsorbates were confirmed by different techniques. Such as differential electrochemical mass spectrometry (DEMS) [110], thermal desorption mass spectrometry (TDMS) [123], and the surface sensitive technique, *in situ* Fourier transform infrared spectroscopy (*in situ* FT-IR) [112, 124].

Among these intermediates, CO is considered as the most important one and has been a subject of debate for many years regarding its strong adsorption effect on the Pt surface. Two distinct viewpoints have emerged over the years: one considers CO as a poisoning intermediate that can block the Pt surface and inhibit the further oxidation of methanol or methanol intermediates. And in an extensive study, a dual pathway mechanism was brought up, which has been a widely accepted as the mechanism of methanol oxidation process on Pt [125]. With adequate hydroxyl, the oxidation of $Pt-(CHO)_{ad}$ can proceed directly into CO_2 or go through this "dual pathway" to form the poisoned intermediate CO, as Reaction 2.84 and 2.85. In this "dual pathway" mechanism, CO is considered as poisoning intermediate. But on the other hand, some argue that CO is actually a promoter that can be oxidized by adsorbed OH on the surface especially in alkaline environment:

$$\mathrm{Pt{-}(CHO)_{ad} + OH^- \longrightarrow Pt{-}(CO)_{ad} + H_2O + e^-} \tag{2.84}$$

$$\mathrm{Pt{-}(CO)_{ad} + 2\,Pt{-}(OH)_{ad} \longrightarrow 2\,Pt + CO_2 + H_2O + 2\,e^-} \tag{2.85}$$

Other pathways involving formic acid or formate are also suggested in many studies [126–130]. Further possible parallel step pathways are shown as below:

$$\mathrm{Pt{-}(CHO)_{ad} + 3\,OH^- \longrightarrow Pt + CO_2 + 2\,H_2O + 3\,e^-} \tag{2.86}$$

$$\mathrm{Pt{-}(CHO)_{ad} + 2\,OH^- \longrightarrow (Pt{-}COOH)_{ad} + 2\,H_2O + 2\,e^-} \tag{2.87}$$

$$\mathrm{(Pt{-}COOH)_{ad} + OH^- \longrightarrow Pt + CO_2 + H_2O + e^-} \tag{2.88}$$

In alkaline solution, the final product in electrolyte is in form of carbonate (${CO_3}^{2-}$):

$$\mathrm{CO_2 + 2\,OH^- \longrightarrow {CO_3}^{2-} + H_2O} \tag{2.89}$$

Overall, the mechanism of methanol oxidation on Pt in alkaline solutions needs to be discussed in a more careful way and one has to be aware of that different experimental setups and surface states of the Pt electrode can lead to varying reaction pathways and outcomes. More in-depth investigations are needed to elucidate the specific details of the reaction pathway and the influence of intermediates on the overall electrocatalytic process.

Chapter 3

Experimental procedure

This work utilizes two experimental setups to investigate the electrocapillary coupling coefficients at the interface. The first setup is the dynamic electro-chemo-mechanical analysis (DECMA), which is a method that was established in out team, specifically designed to quantify these coupling coefficients. DECMA allows for the in-situ measurement of strain-potential and strain-current coupling parameters during electrochemical reactions. By employing DECMA, valuable insights into the electrocapillary behavior can be obtained.

The second experimental setup applied in this study is the cantilever bending setup, a well-established and widely used tool for measuring surface stress evolution. This setup offers exceptional sensitivity and resolution, enabling the accurate monitoring of mechanical changes during reaction processes. The cantilever bending setup provides valuable in-situ mechanical information, complementing the insights gained from DECMA measurements.

Both experimental setups are accompanied by their respective sample and electrochemical cell configurations, which are detailed extensively in this chapter. Through the combined application of DECMA and the cantilever bending setup, this work aims to enhance the understanding of electrocapillary phenomena and provide comprehensive insights into the electrochemical reactions with strain modulation occurring at the electrode-electrolyte interface.

3.1 Samples fabrication and characterization

In this work, two types of Pt thin film samples were used in the two different experimental setups, each equipped with their own *in situ* electrochemical cells. Both of them were sputtered by magnetron sputtering deposition onto different substrates according to the distinct configuration of each cell and individual experiment request. For the DECMA experiment, thin films were deposited onto a Kapton polyimide foil, whereas for the cantilever bending device, polished silicon(100) wafer were used as substrate.

3.1.1 Samples preparation

Magnetron sputtering deposition process

The physical vapor deposition (PVD) technique is widely applied for sputtering thin metal films onto various substrates. As one specific type of PVD, magnetron sputtering deposition uses a voltage on magnetically enhanced argon (Ar) plasma to achieve deposition and is employed for sample preparation in this work. The photo of sputtering device is shown in Figure 3.1 (BESTEC company). In the sample preparation experiment, all substrates were cleaned thoroughly in ethanol using a ultra sonic bath for at least 15 minutes for removing any grease or organic substances on the substrates. After cleaning, the substrates were air-dried, followed by the use of an air blow gun to remove any remaining dusts. Prior to the deposition process, the substrates were cleaned in an argon plasma etching chamber with an Ar pressure of approximately 3.6×10^{-4}

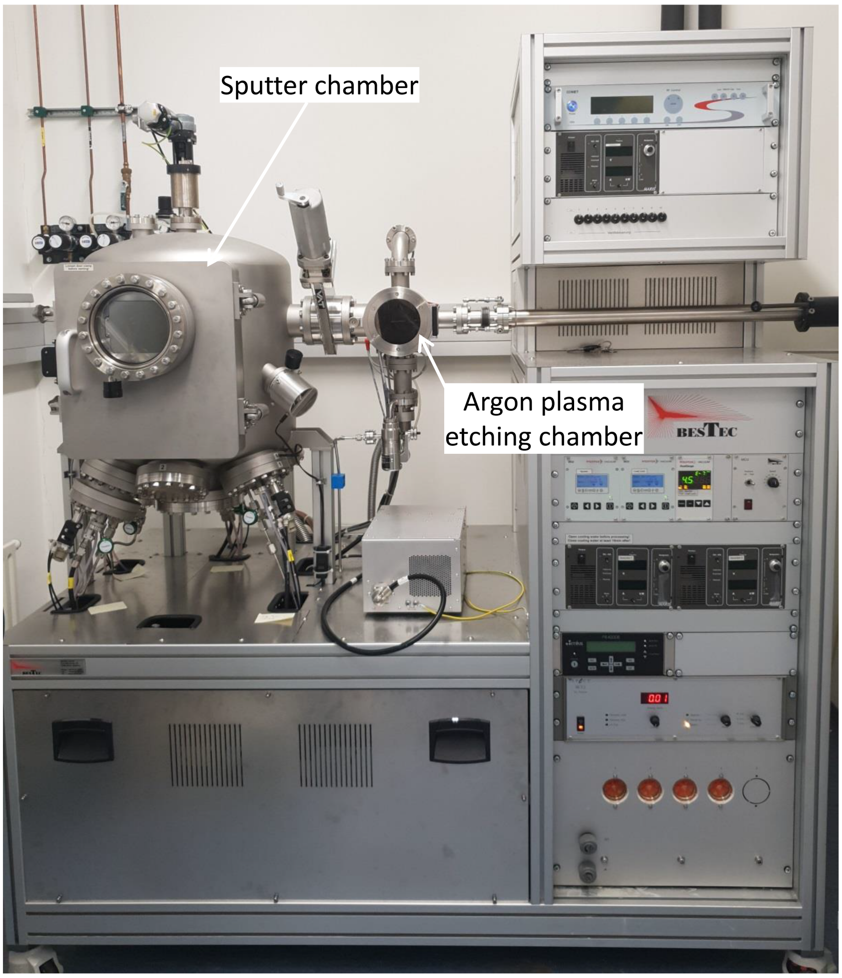

Figure 3.1: Photo of magnetron sputtering device, consists of one main sputter chamber with four ultra-high vacuum (UHV) compatible magnetron sputter sources and a load-lock with an integrated argon plasma etching device.

mbar for 10 minutes. Following the cleaning process, the samples were transferred to the sputter chamber under a high vacuum atmosphere. The base pressure in the sputtering chamber was maintained below 1×10^{-7} mbar.

A titanium layer with a thickness of approximately 8-10 nm was first sputtered onto the substrate as an adhesion promoter, then followed by the deposition of platinum of approximately 80 nm thickness. In this work, the sputtering power applied was 100 W for titanium and 50 W for the platinum target. The distance between the target and the substrate, referred to as the target-substrate distance, was approximately 10 cm for titanium and 12 cm for platinum. The stage rotation rate during deposition was set at 50 rpm. The working pressure in the sputtering chamber was 5.8×10^{-3} mbar. The sputtering rates were approximately 2 nm/min for titanium and 8 nm/min for platinum.

Pt on polymide substrate for DECMA experiment

In the DECMA experiment, a polyimide foil with a thickness of 75 µm was used as the substrate. A mask was place on top of the substrate sheet to ensure a specific geometric sputtered area. The sample geometry is shown in Figure 3.2 a. The entire disc area serves as the working electrode surface, which comes into full contact with the electrolyte meniscus. The diameter of the sample circle is 8 mm.

In order to measure the strain during following DECMA experiment, a strain gauge (HBM

1-LD20-10/120) was carefully attached to the back side surface of substrate. The strain gauge was firmly bonded using a rapid adhesive superglue (HBM Z70), which is specifically designed for strain gauge installation. Typically, it takes at least 30 minutes for the adhesive glue to be completely dry.

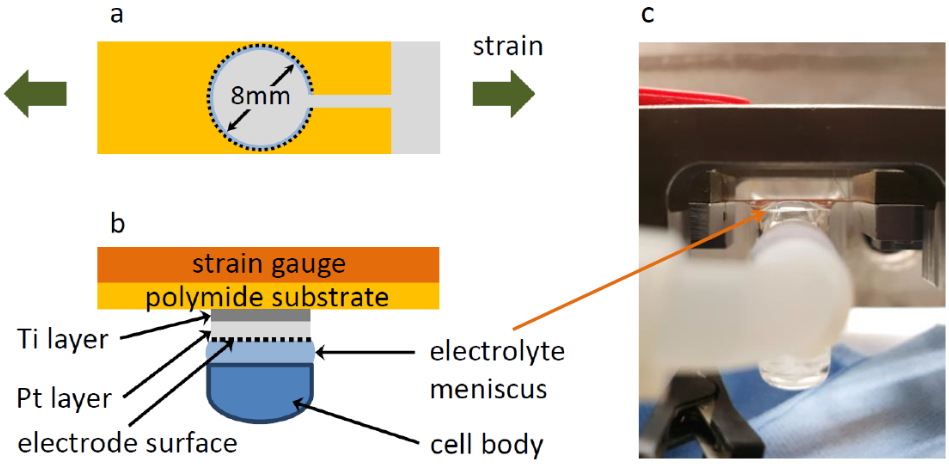

Figure 3.2: The illustration of a) and b) are top view and side view of the sample geometry: Pt thin film on a Kapton polyimide foil with a thin Ti layer on top of the substrate as an adhesive layer. The diameter of working electrode contact area is 8 mm. This specific shape of the sputtered thin film area was achieved using a mask over the substrate during the sputtering process. This design enables the working electrode to connect to the main electrical circuit through a gold wire, which is positioned between the clips and the side part of the thin film. c) the side view photo of the electrode-electrolyte interface with an electrolyte meniscus, which fully encompasses the working electrode area.

Pt on (100) silicon wafer for cantilever bending experiment

In the cantilever bending measurement experiment, silicon wafers with (100) orientation and a thickness of 100 µm (CrysTec company, S6406, p-type) were used as the substrate. The silicon wafers were cut using a diamond cutter into rectangular shapes with a width of 8 mm. The length of the substrate wafer varied depending on the mounting position and was measured using a micrometer each time after mounting. Typically, the length is within the range of 38 ± 2 mm. The illustration of the sample is shown as in Figure 3.10.

Annealing process

After the sputtering process, both types of samples were subjected to an annealing treatment at 350°C for 1.5 hours in an Ar atmosphere with a purity of 99.99%. A horizontal Miniature Tube Furnace (MTF 12/38/400, Carbolite) was employed for annealing. It is important to anneal the Pt thin film in an inert atmosphere and avoid high temperatures (above 400 ℃), because in such condition, the surface of platinum is not expected to form platinum oxide.

The main objective of the annealing treatment was to reduce the stresses within the thin films and to reduce the surface roughness of the samples. This process aimed to optimize the film's structural integrity and improve its overall performance. But it is worthy to note that annealing the Pt thin film samples can also cause an increase in the film resistance [131, 132].

3.1.2 Samples characterization

Atomic Force Microscope

For the characterization of surface topography and roughness, Atomic Force Microscopy (AFM) experiments were conducted using a JPK Instruments NanoWizard in AC mode. AFM is a powerful technique enabling high-resolution imaging and analysis of surface features at the nanoscale. By utilizing Gwyddion software [133] for AFM image processing, the AFM data can be further analyzed and quantitatively characterized, providing valuable insights into the surface morphology, roughness parameters, and other relevant features of the samples.

X-ray Diffraction

To examine the texture of sputtered Pt thin film electrodes on both substrates, X-ray diffraction (XRD) analysis was employed. A $\theta - \theta$ diffractometer, specifically the Bruker D8 Advance, was utilized for this purpose. The diffractometer operated in Bragg-Brentano reflection geometry, using Mo $K_{\alpha_{1/2}}$ radiation. A linear position-sensitive detector with high energy resolution (Lynxeye XE-T) was employed. This detector allowed for precise energy analysis of the diffracted X-ray signals. By measuring X-ray diffraction patterns and analyzing peak intensities and positions, valuable information regarding the crystallographic orientation and preferred crystallographic directions of the platinum films can be obtained.

3.2 Electrochemical systems

In this work, two *in situ* electrochemical cells were employed, each tailored to a specific experimental setup based on individual configurations. One reference electrochemical system was assembled by a commercial polycrystalline Pt tip electrode within a standard electrochemical cell.

To thoroughly characterize each electrochemical system, several key parameters were measured as listed in the table 3.1. Here, we denote the sputtered Pt thin film on Si wafer substrate for cantilever bending setup as $\mathrm{Pt_w}$, sputtered Pt thin film on polymide foil substrate for DECMA experiment as $\mathrm{Pt_p}$, and the Pt tip electrode in standard electrochemical cell as $\mathrm{Pt_t}$. $\mathrm{A_g}$ is geometric electrode surface area, $\mathrm{d_{w-r}}$ is the distance between working electrode and reference electrode, $\mathrm{V_c}$ is the volume of cell, $\mathrm{IR_{drop}}$ is the uncompensated IR drop measured via EIS, and $\mathrm{R_c}$ is connection resistance of Pt working electrode, more specifically, it is measured from the geometric center of the sample to the contact lead.

Table 3.1: Electrical properties of different electrode types

electrode type	$\mathrm{A_g}$ (cm^2)	$\mathrm{d_{w-r}}$ (mm)	$\mathrm{V_c}$ (ml)	$\mathrm{IR_{drop}}(\Omega)$	$\mathrm{R_c}(\Omega)$
$\mathrm{Pt_w}$	3.04	15 ± 2	115 ± 5	11.7 ± 1.2	10.5
$\mathrm{Pt_p}$	0.53	10 ± 1	20 ± 3	61 ± 2	30.5
$\mathrm{Pt_t}$	0.07	10 ± 2	35 ± 3	71 ± 3	<1

3.2.1 Electrolytes and electrodes

All experiments in this study were conducted in a base alkaline solution of 0.1 M KOH at room temperature (20 ℃). Methanol was added to the solution at various concentrations, ranging from 0.02 M to 1 M. All electrolytes were prepared with ultra-pure water with a resistivity of 18.2 MΩ·cm (Sartorius, Germany). To ensure the absence of oxygen, all electrolytes were purged with Ar gas (99.99%) for a minimum of 2 hours prior to conducting the measurements. This process effectively removed any potential solvable oxygen in the electrolyte.

The sputtered Pt thin film samples mentioned above serve as the working electrode (WE) in each system. A gold thin plate with a sufficiently large surface area was employed as the counter electrode (CE). The reference electrode (RE) utilized was a commercial mercury-mercuric oxide (Hg/HgO) electrode (RE-61AP, from BAS Japan), specifically designed for use in strong alkaline solutions, with a relative potential to a reversible hydrogen electrode (RHE) of approximately 835 mV. All potentials in this study were converted to RHE to facilitate comparison with experimental data from other studies.

3.2.2 Electrochemical techniques

All electrochemical measurement in this work were conducted by using a high performance potentiostat (Autolab PGSTAT302N, Metrohm) equipped with a linear scan generator, a staircase module for precise electrode potential control, and an impedance module for electrochemical impedance measurements. The software used for procedure programming and data analysis is NOVA (Metrohm, versions V1.10 and V2.10). The coupling signals were connected to the front panel of the potentiostat as external signals and presented in the same interface simultaneously with the current.

Cyclic voltammetry

In this work, two types of voltammetry were applied employed to investigate the electrochemical interface behaviour during methanol oxidation reaction process. One is the classic staircase DC cyclic voltammetry (Nova, V1.10), and the other is the AC cyclic voltammetry (Nova, V2.10). The step potential in DC cyclic voltammogram was set to 2.5 mV for a finer resolution of the current response, and the potential scan window and the scan rates were varied depending on different experimental scenarios.

In AC cyclic voltammetry measurements, the DC step potential was set to 12 mV, and the applied potential waveform was sinusoidal with modulation amplitude of 5 $\mathrm{mV_{RMS}}$, the frequency was chosen to be the same as the external applied strain frequency.

Electrochemical impedance spectroscopy (EIS)

Electrochemical impedance spectroscopy (EIS) tests were conducted in this study to characterize the electrochemical behavior of the samples. The tests were performed over a frequency range of 0.1 Hz to 100 kHz with a sinusoidal voltage with an amplitude of 10 mV.

3.2.3 Resistance measurement

To measure the contact resistance of WE in the electric circuit, a four-point technique was employed. This technique is universally used to provide a precise measurement of the resistance with minimizing the influence of contact resistance and lead resistance. This four-point technique involves four probes with equal intervals as shown in Figure 3.3. A DC current flows between probe 1 and 4, and a sensitive voltmeter is placed in between probe 2 and 3. In practical, this measurement was done by single instrument (Model 2450 System SourceMeter, Keithley), which can source and measure both current and voltage and can be configured to display the resistance.

For the two types of thin film samples mentioned, multiple spots on each sample surface were tested, with the exact contact points illustrated in Figure 3.4. The measured resistance includes both the intrinsic sample resistance and the circuit connection resistance. Since the sample resistance is geometry dependent, the average resistance from different contact points was calculated.

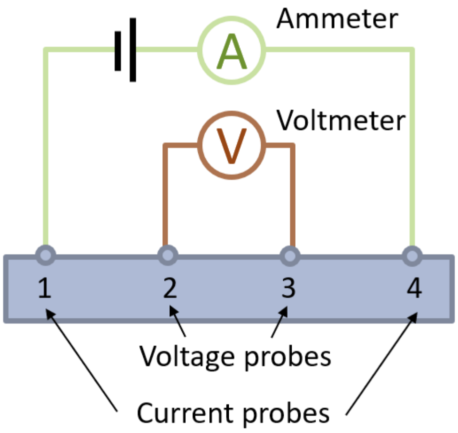

Figure 3.3: A schematic diagram of a four-point probe on sample surface. The four probes have equal spacing. A current flows through the circuit via probe 1 and probe 4, whilst the voltage is measured between probes 2 and 3.

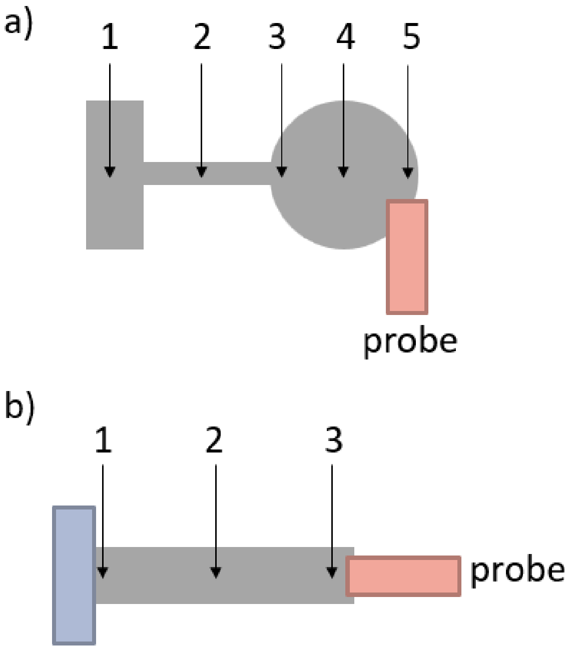

Figure 3.4: The connection positions of probes on the sample surface. a) Pt sample for DECMA with five positions. b) Pt sample for cantilever bending experiment with 3 positions

3.3 Dynamic electro-chemo-mechanical analysis (DECMA)

3.3.1 Configuration of DECMA setup

Mechanical framework

Figure 3.5 displays the photograph of all components of DECMA setup. The mechanical framework part is situated inside a sealed chamber. This sealed chamber can be connected to a vacuum pump and supplied with different gases, such as argon or oxygen, according to the experimental requirements.

One end of the sample is fixed to a piezo (P-844.30, Physik Instrumente) and securely held in place, while the other end can be positioned within a short and adjustable distance range. Buckling of the electrode was avoided by applying slight pretension, typically less than 1% static tensile strain. This level of strain was determined by monitoring the imposed load on the substrate through the piezo-actuator. Importantly, the thin metal film adhered strongly to the substrate during entire measurement under this slight pretension.

Typical displacement amplitudes ranged from 10 to 20 µm, resulting in cyclic strain amplitudes on the order of 10^{-4}. To facilitate straightforward pre-strain adjustment, a small screw micro-manipulator was employed to ensure the entire sample maintained a slight tautness. This approach ensured a consistent strain state throughout the experiment.

In situ electrochemical cell of DECMA setup

The electrochemical cell is purposefully constructed to partition the working electrode and the counter electrode into two distinct compartments. This segregation serves to prevent any potential cross-contamination of reactions between the two electrodes. Furthermore, the application of a luggin capillary serves to position the reference electrode in close proximity to the working electrode, thereby enhancing the accuracy of the reference measurement and minimizing uncompensated solution resistance.

During the assembly of the thin film sample, a thin gold wire is positioned between the clips to serve as an electrical connector. In the enlarged photograph, it is evident that the electrochemical cell is positioned beneath the working electrode. For a detailed depiction of the electrode-electrolyte interface, please refer to Figure 3.2, which provides a side view of the specific connections. The connection was via an electrolyte formed meniscus, which covers the whole WE surface area. Such connection was stable enough to survive even long time measurements.

3.3.2 Electronic devices connection circuit

The sketch of whole DECMA setup connection to a potentiostat is described as Figure 3.6, and is consisted of following electronics components: potentiostat, lock-in amplifier, piezo actuator, piezo controller, strain measurement amplifier and external resistance. The piezo actuator is connected to the oscillation output port of the lock-in amplifier, enabling operation within an effective frequency range of 1 Hz to 180 Hz. A strain measuring amplifier (HBM, QuantumX MX410B) is connected to the strain gauge as the input, amplifying the strain signal proportionally as the output. This output is then connected to the reference input of the lock-in amplifier as the reference signal. An external resistance is strategically employed at various points with predefined values to facilitate the conversion between two coupling parameters. The diagram elucidates the interconnections and arrangement of components tailored to each coupling parameter experiment.

Potential-strain coupling coefficient measurement

In the strain-potential coupling coefficient measurement experiment, there are two input ports on front facet of lock-in amplifier, port A was connected to the working electrode and port B

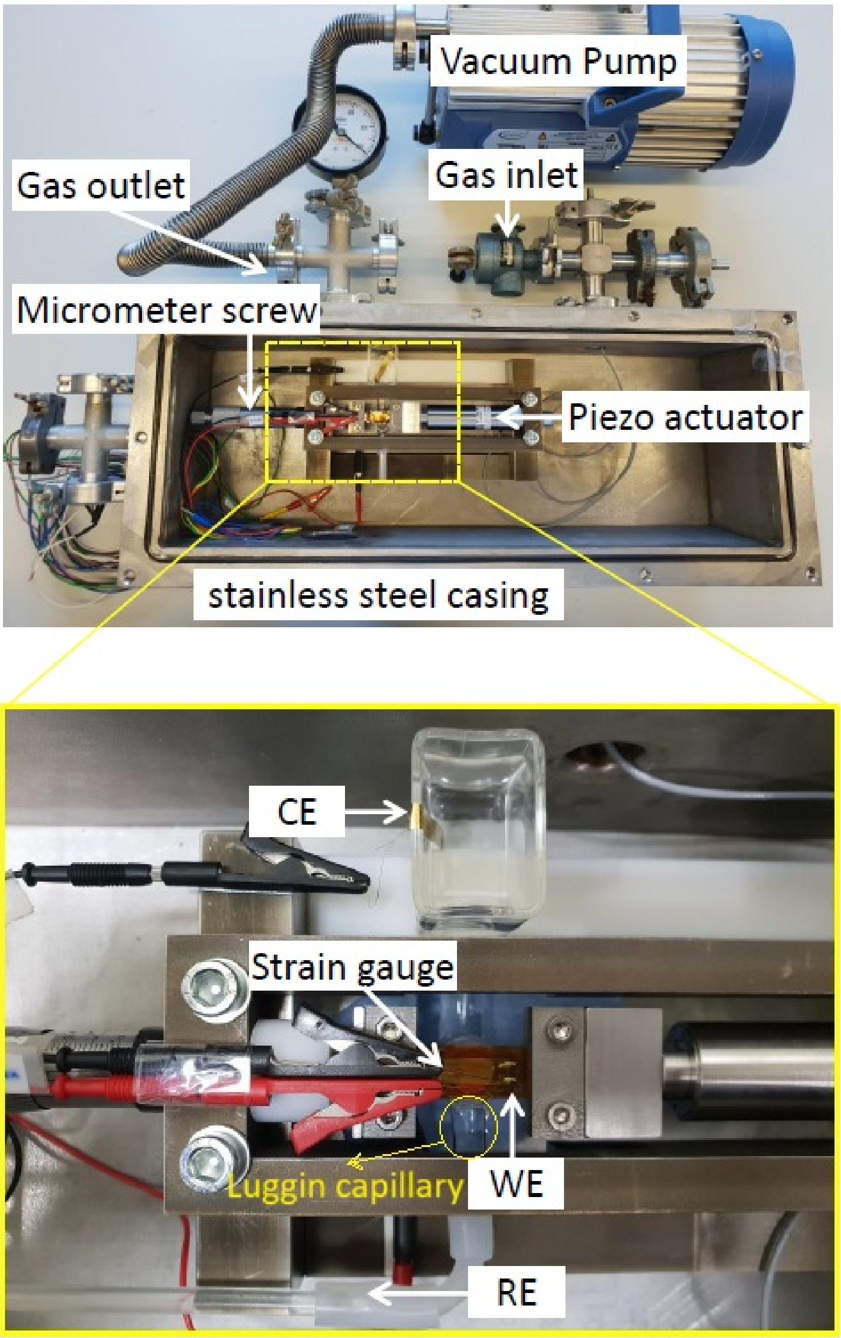

Figure 3.5: In-situ DECMA setup: a) the mechanical frame part is placed inside of a stainless steel casing for conducting experiment in a certain atmosphere. b) electrochemical cell with three electrodes: working electrode (WE): Pt thin film on polymide foil substrate with strain gauge glued on the back of substrate; counter electrode (CE): gold thin plate; reference electrode (RE): mercury/mercury oxide (Hg/HgO).

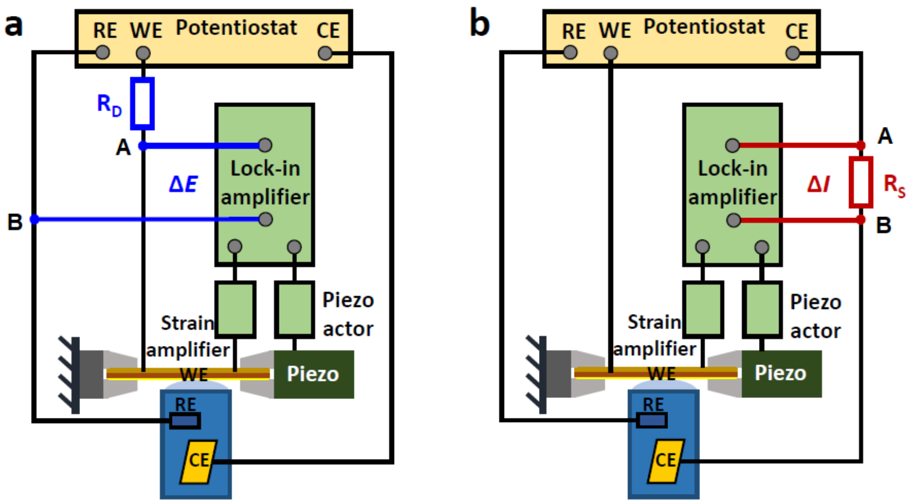

Figure 3.6: Schematic diagram illustration of the setup circuit connection for DECMA experimental configuration. Two different connection methods are depicted to facilitate the measurement a) strain-potential coupling coefficient b) strain-current coupling coefficient.

was connected to the reference electrode. A resistance delay (R_D = 5 kΩ) is placed between the potentiostat and working electrode, and it is crucial to maintain a constant charge density environment during the measurement, ensuring that the current flowing through the electrode remains negligible within a strain cycle. However, it is important to note that even with negligible current, a significant potential drop can occur in the circuit due to the large resistance. Therefore, when plotting cyclic voltammetry and potential-strain coupling coefficient graphs with the potential of the electrode as the abscissa, a correction of the real working electrode potential needs to be applied as following:

$$E_{\mathrm{WE}} = E_{\mathrm{applied}} - (IR_{\mathrm{D}}) \tag{3.1}$$

Current-strain coupling coefficient measurement

In the strain-current coupling coefficient measurement experiment, in order to measure the strain-induced current amplitude, a small resistance, R_s, was added in series with the counter electrode, as depicted in Figure 3.6 b. The current variation caused from strain modulation was recorded as the potential drop across this shunt resistance, which is 50 Ω. The direction of the current flow in this setup followed the convention used in the potentiostat. Specifically, port A was connected to the counter electrode, and port B was connected to the potentiostat. Therefore, the current flowed from the counter electrode towards the potentiostat, or from port A to port B.

3.3.3 Lock-in technique

The lock-in amplifier (Ametek, Model 7265) serves as a critical component within the entire setup. Its primary role entails extracting and amplifying weak AC signals embedded within a noisy environment. The operation of a lock-in amplifier involves phase-sensitive detection (PSD), which allows for the selective amplification of signals with a specific frequency [134]. It essentially "locks in" to the desired signal by synchronizing its reference oscillator with the input signal. The lock-in amplifier multiplies the input signal with the reference oscillator then passes it through a low-pass filter to extract the desired frequency component, as shown in Figure 3.7.

The reference signal can originate from either the internal oscillation generator within the lock-in amplifier or an external signal provided as input to the lock-in amplifier. In this work, the reference signal is provided externally from the strain gauge via a strain measurement amplifier,

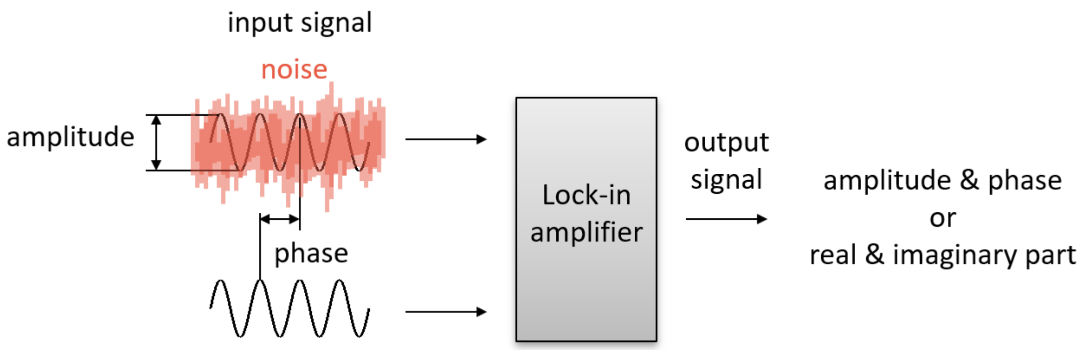

Figure 3.7: Lock-in amplifier function: filtering the information of a sinusoidal signal relative to a defined reference signal, even in the presence of noise

which supplies the *in situ* sinusoidal strain signal with frequency ω and amplitude (R). This configuration ensures that the lock-in amplifier synchronizes its phase with the strain-induced signal, enabling accurate detection and analysis of the strain-related phenomena.

When dealing with sinusoidal signals, there are two common methods for representation: magnitude and phase shift, or complex numbers. A phase shift (θ) typically exists between the reference signal (externally provided strain signal) and the input signal (modulated potential or current signal). When $\theta = 0$, the output signal is referred to as the in-phase or real part signal ($X = E\cos\theta$). Conversely, when $\theta = \pi/2$, the output signal is considered the out-of-phase or imaginary part signal ($Y = E\sin\theta$).

During cyclic voltammetry, both the real and imaginary output analog signals are simultaneously recorded and converted into voltage form. Consequently, the lock-in amplifier enables the recording of four signals in total. The relationship between these signals can be described by Equation 3.2.

$$\begin{aligned} R &= (X^2 + Y^2)^{\frac{1}{2}} = E \\ \theta &= tan^{-1}\left(\frac{Y}{X}\right) \end{aligned} \tag{3.2}$$

By recording and analyzing these signals, valuable information regarding the electrochemical response and its relationship with the applied strain can be obtained.

3.3.4 Strain measurement

Strain gauges are commonly used device to precisely measure the strain of a specimen. To measure strain *in-situ* by using a bonded resistance strain gauge, it needs to be connected to an electrical circuit capable of detecting the small changes in resistance that correspond to strain [135]. Typically, strain gauge transducers employ four strain gauge elements that are electrically connected to form a Wheatstone bridge circuit [136, 137].

The strain gauge measured axial strain ($\frac{\Delta L}{L_0}$) was then calculated into areal strain according to Equation 3.3.4:

$$\varepsilon = (1 - \nu_{\mathrm{p}})\frac{\Delta L}{L_0} \tag{3.3}$$

where ε represents the areal strain, ν_p is the Poisson ratio of the kapton polyimide film, ΔL is the change in length, and L_0 is the original length. The Poisson ratio of the kapton polyimide film is reported to be 0.35 at room temperature [138]. So the estimated value for areal strain in this work is around $2 \pm 0.2 \times 10^{-4}$ at room temperature with a prestrain.

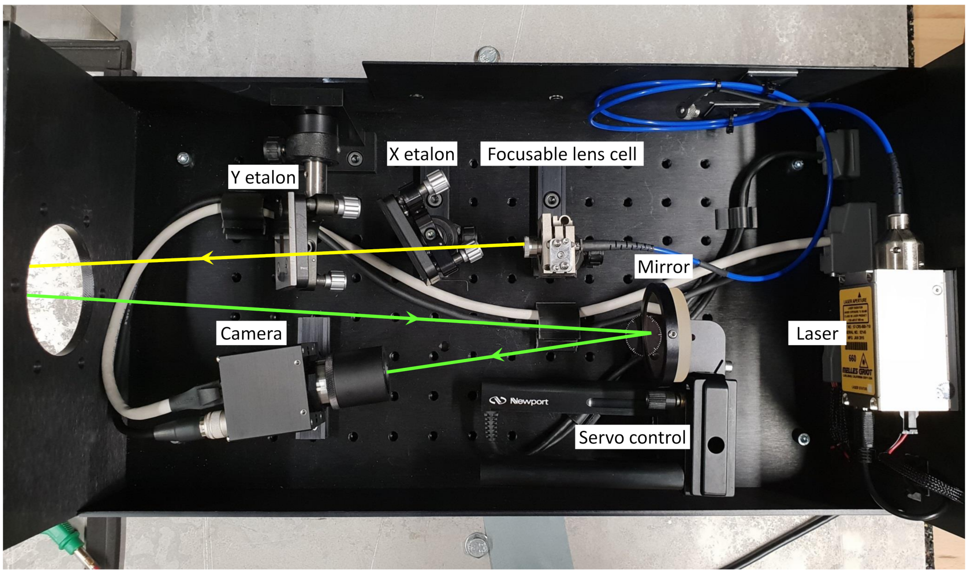

Figure 3.8: A photograph of multi-beam optical system (MOS) device in cantilever bending experiment. The laser path is from the He-Ne laser generator through a focusable lens cell, then passing through x etalon and y etalon. The laser reflected off the sample surface is subsequently collected by a CCD camera which faces a mirror, the position of which can be adjusted finely by using a servo control system.

3.4 Cantilever bending experiment

3.4.1 Configration of cantilever bending setup

Multi-beam optical system (MOS)

In this work, the cantilever bending setup was employed to investigate the *in situ* evolution of surface stress during the potential cycles of cyclic voltammetry. It is a well-established method for measuring surface stress variation by applying a multi-beam optical system (MOS). The MOS system consists of an array of parallel laser beams and a charge-coupled device (CCD) area detector. By monitoring the curvature (k) of the wafer substrate, the surface stress of the sample can be determined. Figure 3.8 illustrates the optical components included in the MOS system implemented in this work.

The incident beams are generated by splitting a laser beam through two intersecting etalons, which strike the metal-coated face of the thin film sample, as shown in Figure 3.10. The reflected beams from the sample are subsequently reflected by a small mirror then captured by the CCD camera, allowing for real-time image analysis. The curvature of the sample is acquired from the spacing variation of the reflected beams according to Equation 3.4.

$$\Delta\kappa = \left(\frac{\delta d}{d_0}\right)\frac{\cos\alpha}{2L} \tag{3.4}$$

d_0 is the origin distance and δd is the distance variation caused by surface stress state changing. L is the distance between sample surface to camera and α is the angle between sample surface and the beam array (3 × 3), as shown in Figure 3.9. In our setup setting, the distance L is about 110 ± 2 cm, and α is 3°. The minimum resolvable curvature is $4\times10^{-6}\,\mathrm{m}^{-1}$ or a maximum radius of curvature of 250 km.

The well-known Stoney's equation provides the surface stress variation calculation equation, Equation 3.5, from the curvature variation $\Delta\kappa$ of substrate [96].

$$\Delta f = \frac{1}{6}\Delta\kappa M_s h_s^2 \tag{3.5}$$

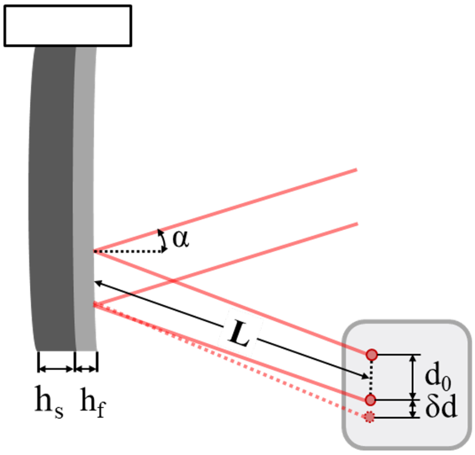

Figure 3.9: Schematic of the change in spacing (δd) between initially parallel laser. h_s and h_f denote the thickness of the Si wafer substrate and the sputtered thin film. L is the distance between sample surface to camera and α is the angel between sample surface and laser beam array.

M_s is the bi-axial modulus of the substrate and h_s is the silicon substrate thickness. To enhance the sensitivity of the signal, we utilized 100 μm thick and (100)-oriented Si wafer as substrate. A thinner substrate offers a higher resolution for the measured signal. Due to the significant difference in thickness between the substrate and the thin film, the thin film is compelled to adopt the strain experienced by the substrate, and is simply estimated by the bulk Young's modulus of the silicon(100) wafer substrate, represented as Y, Y = 130.2 Gpa [139], thus the bi-axial modulus is calculated as:

$$M_s = \frac{Y}{1-\nu_s} \tag{3.6}$$

and $\nu_s = 0.279$ is the Poisson ratio of the Si wafer substrate [140]. Combined above calculations, the surface stress variation is known to be proportional to the measurable distance variation $\left(\frac{\delta d}{d_0}\right)$ of the deflected beams, which can be described as:

$$\Delta f = \left(\frac{\delta d}{d_0}\right)\frac{M_s h_s^2 \cos\alpha}{12L} \tag{3.7}$$

To enhance the accuracy of the measurement, the laser array was placed at the end of the cantilever, as the laser beams interact with the cantilever in a region of free biaxial bending [141]. In other words, the free biaxial bending is expected when the distance is longer than the wafer length.

In situ electrochemical cell of cantilever bending setup

Figure 3.10 presents a schematic representation of the configuration of the electrochemical cell and three electrodes, including detailed information about the sample. The cantilever was fully immersed in the electrolyte to eliminate artifacts originating from capillary forces at the solid-liquid-gas triple junctions. The dimensions of the electrochemical cell are approximately 93 × 57 × 128 mm. The working electrode, which was clamped by a 1-2 mm wide short edge with the sputtered platinum side facing the laser beam, was positioned in the middle of the cell. A thin gold plate used as the counter electrode, and a Hg/HgO reference electrode was situated on the opposite side.

When analyzing the curvature in an electrolyte, it is essential to consider the refractivity of the aqueous electrolyte. The refractive index of a medium affects the propagation of light through it and can introduce changes in the observed curvature measurements. To accurately analyze the curvature in the electrolyte, it is necessary to consider the refractive index n of the

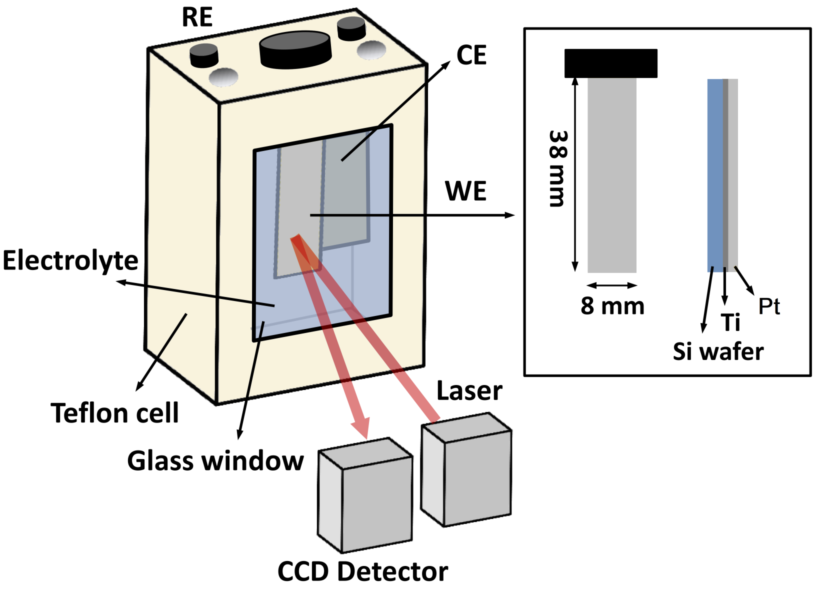

Figure 3.10: Sketch of the experimental electrochemical cell of cantilever-bending setup.The whole cell body is made from Teflon. A glass was placed and faces the laser.

aqueous electrolyte to account for the refractive effects. When the concentration of alkaline and methanol containing electrolytes are relatively low, it is common to use the refractive index of water ($n = 1.33$) for the refractive index of the electrolyte. And the final formula for surface stress variation calculation is shown as below:

$$\Delta f = \left(\frac{\delta d}{d_0}\right) \frac{M_s h_s^2 \cos\alpha}{12Ln} \tag{3.8}$$

Chapter 4

Results

4.1 Characterization of platinum thin film electrodes

4.1.1 Atomic force microscope (AFM) and roughness factor

Figure 4.1 shows the surface topology characterization by atomic force microscope on two Pt thin film electrodes with different substrates. Both of them were subjected to annealing heat treatment at 300 ℃ for 1.5 hours. The surface roughness factor, which is calculated according to

$$\rho = \hat{A}/A_{eff} \tag{4.1}$$

$\hat{A}$ is the actual surface area measured at the atomic scale and A_{eff} is the projected macroscopic surface area [70], which is usually considered as the ideally flat surface without asperities. The roughness factor of each as determined from images (1 µm ∗ 1 µm) show in Figure 4.1 are 1.032 for sample with silicon(100) wafer substrate and 1.020 for the one with Kapton substrate. The values of ρ were obtained by analyzing the AFM data with the Gwyddion software [133].

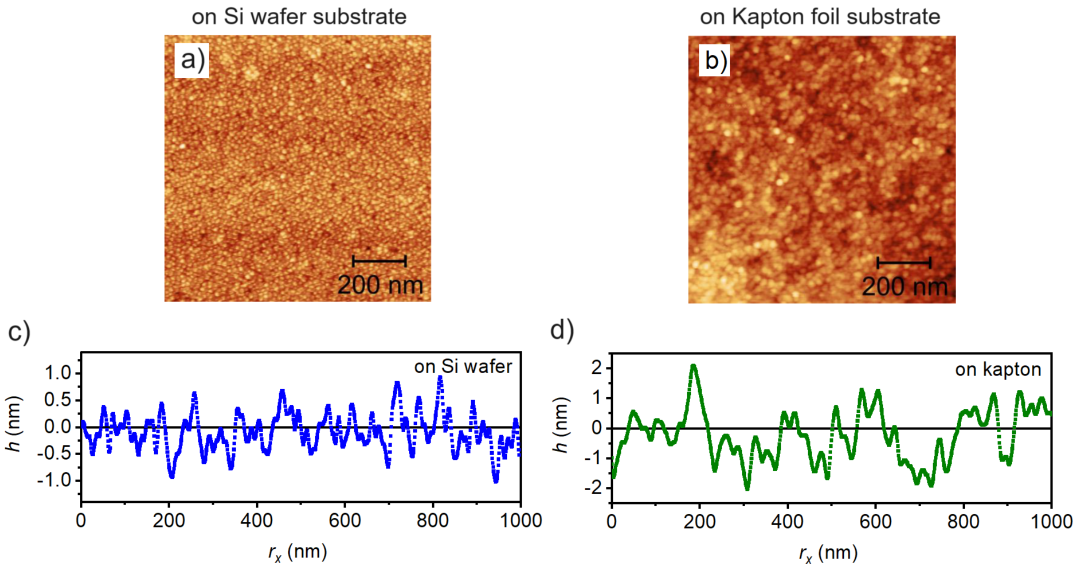

mt

Figure 4.1: a) Surface topology photo from AFM of sputtered Pt thin film on a 100 µm thick silicon wafer as substrate and applied in cantilever bending experiment. b) Surface topology photo from AFM sputtered Pt thin film on a 75 µm thick kapton film as substrate and applied in DECMA experiment. c) surface height profile measured in above area of a). d) surface height profile measured in above area of b). Images of 1µm ∗ 1µm area with 1024 ∗ 1024 resolution.

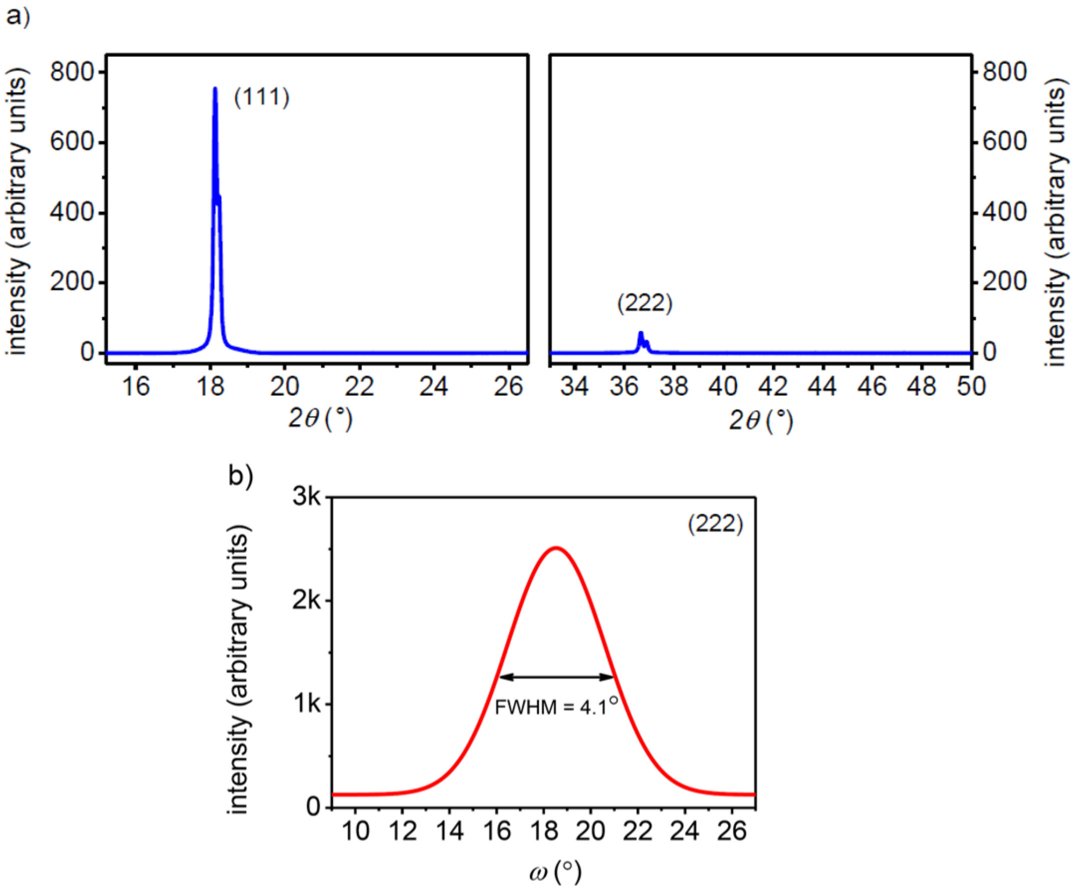

Figure 4.2: X-ray diffraction characterization and rocking curves of Pt thin film on silicon(100) water substrate. a) the diffraction data featured only the (111) reflection and indicated no obvious trace of the (200) or (220) ones. b) shows a rocking curve with (222) reflection. The 2nd order reflection was chosen because it afforded a higher range in the misorientation angle ω than (111). The full width at half maximum (FWHM) is 4.1°. Such quite small angular spread suggests that the exposed electrode surface is predominantly of (111)-type.

4.1.2 X-ray diffraction characterization

The texture of the Pt electrodes on both substrates was investigated by means of X-ray diffraction. We used a $\theta - \theta$ diffractometer (Bruker D8 Advance) with Mo $K_\alpha 1/2$ radiation in Bragg-Brentano reflection geometry, along with a linear position-sensitive detector with high energy resolution (Lynxeye XE-T). The X-ray diffraction characterization of Pt deposited on (100) silicon wafer is shown as Figure 4.2a. The peak appearing at around 18° indicates a strong (111) orientation of this thin film sample, and Pt(222) appears at around 36.7°. No other potential Pt orientations were found during this wide scan range (a discontinuous scan range is because a strong silicon(100) peak appears there). A rocking curve was also measured to detect possible misorientation, which produced a sharp peak with a full width at half maximum (FWHM) of 4.1°. Above characterization methods indicate a smooth surface texture with predominately (111) crystallographic orientation. Very similar surface topology was found on the Pt thin film sample with kapton foil substrate as shown in Figure 4.3. The surface preferred orientation is still (111) but a wider peak with a FWHM of 10.23° was observed. These two samples followed the same sputtering conditions.

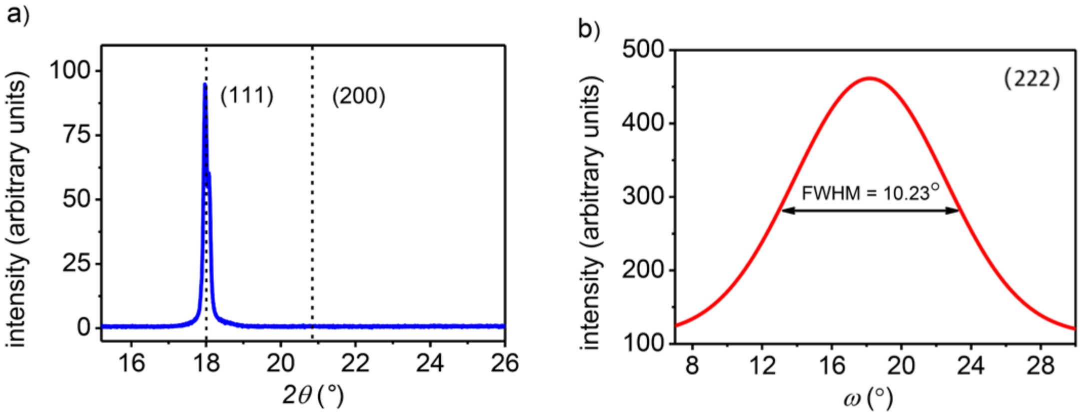

Figure 4.3: X-ray diffraction characterization and rocking curves of Pt thin film on Kapton foil substrate. a) the diffraction data featured only the (111) reflection and indicated no obvious trace of the (200) or (220) ones. b) show the analogous rocking curve for the Kapton-supported film, but the FWHM is here wider, 10.2°. This suggests a somewhat higher incidence of non-dense-packed surface facets or of defects, yet the predominant surface character is still expected to be (111).

4.1.3 Electrochemical characterization and analysis of electrochemical systems

To ensure a consistent and comparable electrochemical environment, CVs were measured under the same electrochemical condition in each *in-situ* electrochemical cell. This involved using the same counter electrode, reference electrode, and electrolyte for each measurement, which helps eliminate potential sources of variation and ensures that any observed changes in the CV profiles are due to the specific properties of the sample being investigated, rather than external factors related to the experimental setup.

Figure 4.4a shows the results of the CVs comparison with normalized current density amplitude in the electrolyte containing 0.1 M methanol within a 0.1 M KOH supporting electrolyte at room temperature. Notably, all CVs display the typical features of methanol oxidation peaks in both the anodic and cathodic directions. The tafel slope of the anodic and cathodic methanol oxdation peaks indicates slight differences in kinetics on different electrodes, this is attributed to individual nature of the electrode surface states, such as surface roughness, crystalline orientation and electrochemical active surface. The one with strongest (111) orientation surface, namely sputtered Pt on wafer (blue curve) shows the highest tafel slope among three electrodes. This observation confirmed that the (111) orientation is less favorable and demonstrates lower activity in methanol oxidation in alkaline solution [142], which is due to the presence of fewer defects and domain boundaries compared to polycrystalline Pt.

To provide a more detailed characterization of the two main *in situ* electrochemical cells, the EIS measurement was conducted in each electrochemical system. Figure 4.5a and c show the Nyquist and Bode plots for the Pt thin film on the Si wafer substrate used in the cantilever bending setup, while Figure 4.5b and d show the Nyquist and Bode plots for the Pt thin film on the Kapton foil substrate used in the DECMA setup. In practical circumstances, the high-frequency intercept of the Nyquist plot on the real axis represents the sum of the uncompensated resistance and any additional contributions from other elements in the system, such as electrode resistance and contact resistance. From the Figure 4.5a and b, the uncompensated resistance of two electrodes are 11.7 Ω and 61 Ω respectively. It is important to stress that all EIS data shown in Figure 4.5 were presented without geometrical area normalization. Therefore, during IR drop compensation calculation, the current without geometrical area normalization was employed to ensure an accurate IR drop correction. Namely, a high compensated resistance does not necessarily result in a high uncompensated potential, particularly if the electrode surface is sufficiently small [143]. From the Bode plots in Figure 4.5c and d, we observe very similar electrode behavior

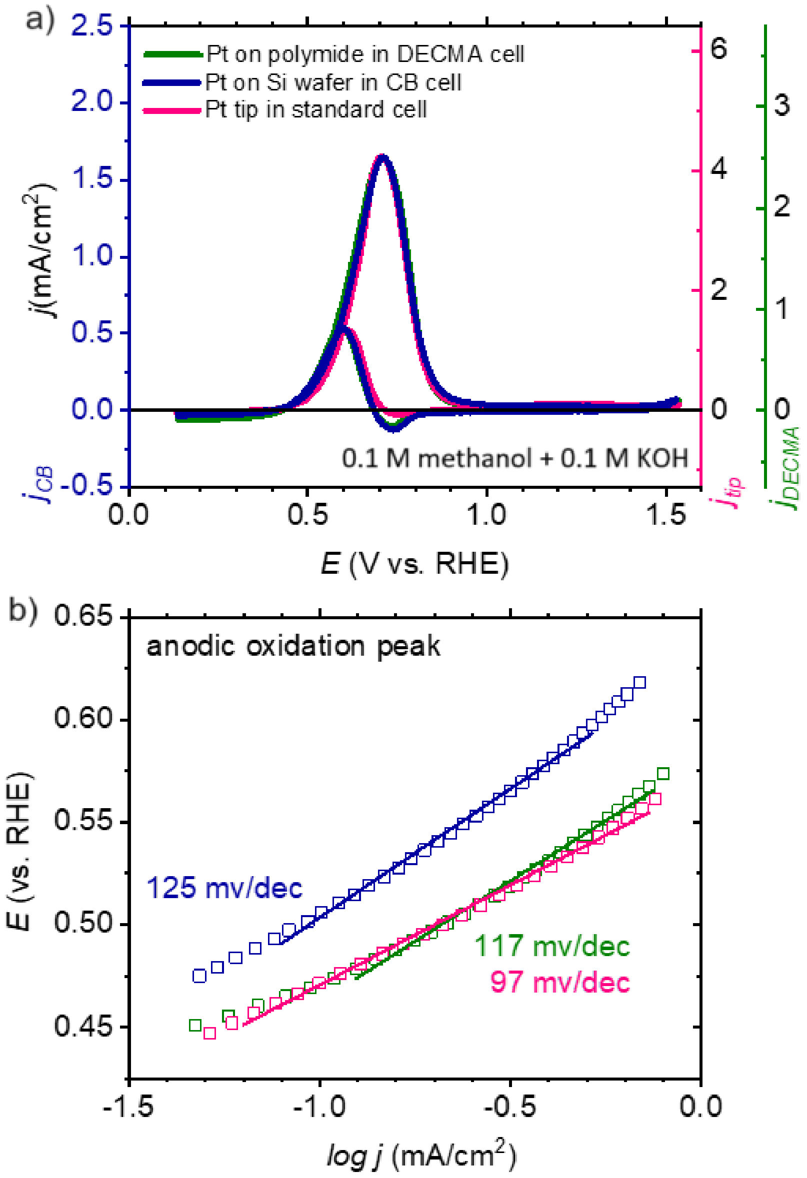

Figure 4.4: Cyclic voltammograms measured in two *in situ* electrochemical cells employing in cantilever bending and DECMA setups, alongside a standard electrochemical cell. a) current density,j, versus potential on three electrodes: j_{wafer} on a Si wafer substrate, j_{poly} on a kapton foil substrate, and j_{tip} on a polycrystalline Pt tip electrode. b) the Tafel slope of the anodic methanol oxidation peak, derived from panel a). The scan rate was 20 mV/s.

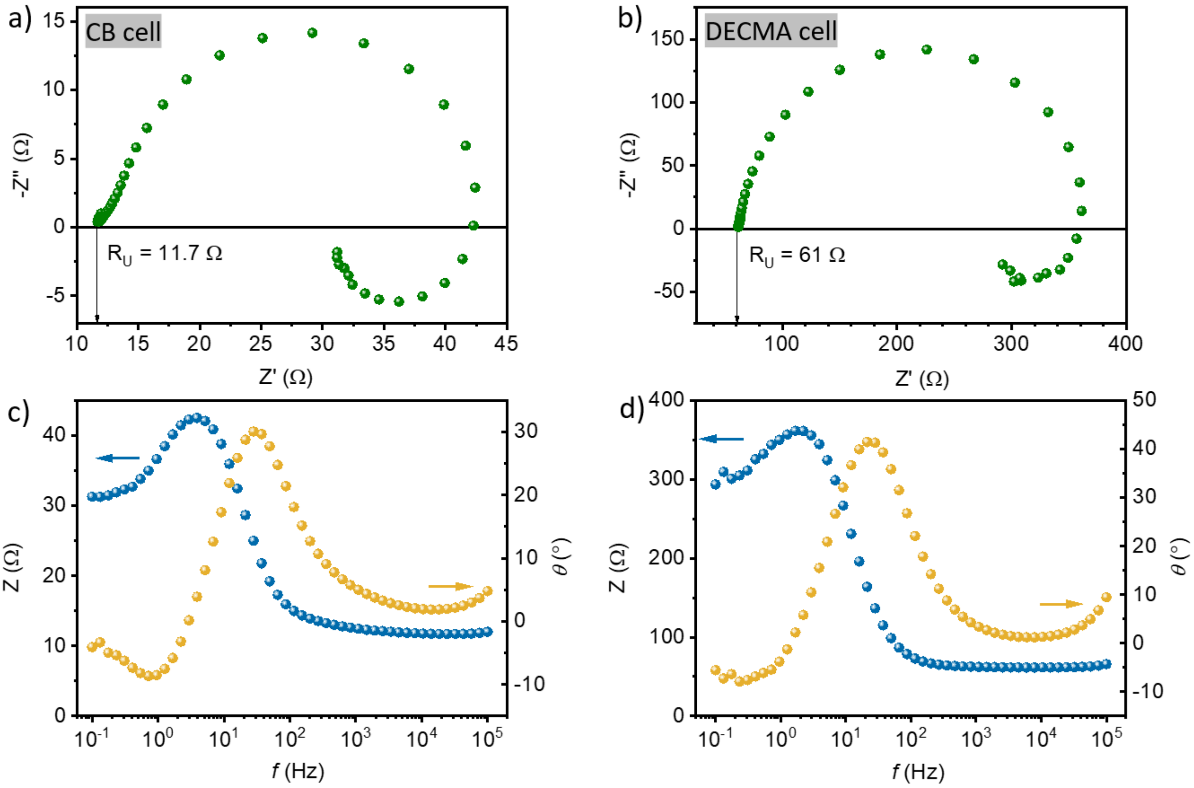

Figure 4.5: Nyquist and Bode polts obtained from EIS measurement on Pt electrodes in two electrochemical systems. The left column (a and c) is on a wafer substrate in cantilever bending setup *in situ* cell, and the right column (b and d) is on Kapton foil substrate in DECMA setup *in situ* cell. The frequency range was from 100 kHz to 0.01 Hz at the potential of 0.635 V.

profiles, including the positions of the peaks and the overall trends of impedance and phase shift, suggesting comparable electrode reactivities. In the higher frequency region, the resistance is mainly represented by the real part, with a phase shift close to zero, which is an alternative way to determine the uncompensated resistance. More detailed EIS results at different potentials can be found in the subsequent section 4.2.2.

4.2 Methanol oxidation reaction (MOR) on Pt electrode

To comprehensively understand the mechanism of methanol oxidation reaction, the behavior of Pt was initially investigated in a KOH supporting electrode without methanol involvement. This aims to establish foundational knowledge and insights into the Pt electrochemical behavior before delving into the complexities of the methanol oxidation reaction.

4.2.1 Pt performance in supporting alkaline solution

Figure 4.6 shows the typical CV profile of surface oxidation on a sputtered Pt thin film electrode in 0.1M KOH solution with five consecutive scans, which was measured in the *in situ* electrochemical cell in cantilever bending setup, showing a pretty good consistence with CVs found in literature [144–146]. It is important to note that the first scan in all cyclic voltammograms shown in this thesis is excluded, the CV was only recorded after a series of consecutive identical CVs, which are stable with reproducibility.

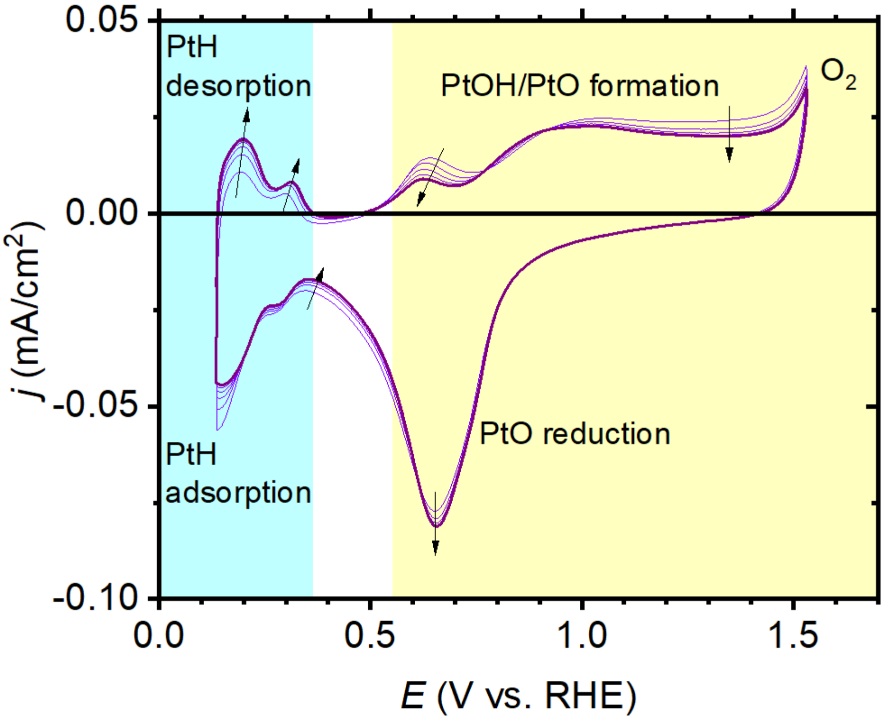

Figure 4.6: Cyclic voltammogram of oxidation and reduction on a sputtered Pt thin film electrode in 0.1 M KOH electrolyte with consecutive 5 cycles. From lower to higher potential along the scale, the hydrogen adsorption/desorption region (light cyan area), double layer region (white area) and surface oxidation/reduction region (light yellow area). The small black arrows indicate from the second scan to the last scan (thicker solid line). Scan rate was 20 mV/s.

Hydrogen and oxygen evolution regions can be readily distinguished from CV with a short double layer region in between, spanning from 0.38 V to 0.55 V, as shown in the white area in Figure 4.6, different regions are divided by different colors. Starting from the cathodic vertex, namely the hydrogen region where the E is below 0.38 V (light cyan area in Figure 4.6), various

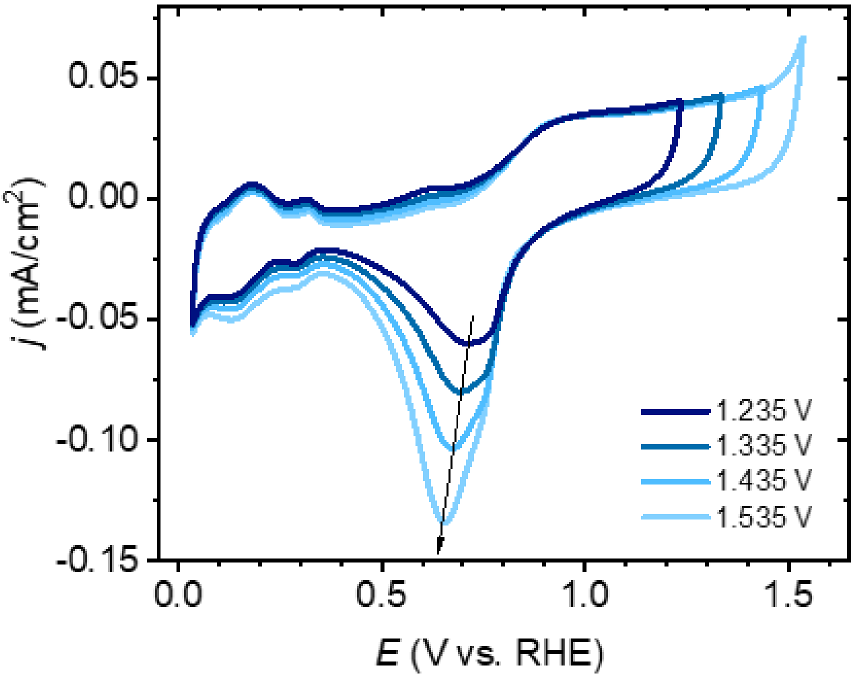

Figure 4.7: CV of Pt measured in 0.1 M KOH with different anodic potential scan limit. The scan rate was 20 mV/s.

small hydrogen adsorption and desorption peaks can be observed. These features are often used to identify specific surface sites on the electrode [147–151]. A systematic downward shift of the current in this HUPD region suggests a noticeable oxygen reduction reaction current. This arises from molecular oxygen that is generated near the anodic vertex of the CVs which cannot be removed completely in this situation, as our *in situ* cell is not compatible with flowing inert gas for oxygen removal. With increasing potential, when the potential is over 0.65 V, the surface starts to adsorb OH and form an oxide layer on the surface during this oxidation process (light yellow area in Figure 4.6):

$$\mathrm{Pt} + \mathrm{OH}^-_{\mathrm{sol}} \longrightarrow \mathrm{Pt{-}OH}_{\mathrm{ads}} + \mathrm{e}^- \tag{4.2}$$

and from $E = 1$ V, the further oxidation of the surface occurs with increasing anodic potential to form Pt oxides [152, 153]:

$$\mathrm{Pt{-}OH}_{\mathrm{ads}} + \mathrm{OH}^-_{\mathrm{sol}} \longrightarrow \mathrm{Pt{-}O}_{\mathrm{ads}} + \mathrm{H_2O} + e^- \tag{4.3}$$

This process is known for surface roughening or irreversible surface reconstruction [146, 148, 149, 154], which is caused by a quite low kinetic of initial reduction of Pt oxides. From the potential around 1.4 V, molecular oxygen starts to be formed on the electrode surface from the adsorbed surface oxides and dissolved in electrolyte, which is an irreversible process. During the cathodic scan, the surface under oxidized state begins reduction process at $E = 0.85$ V. After the surface oxygen species have been lifted, the clean surface adsorbs hydrogen from electrolyte till the vertex of negative potential.

More dynamic information of surface state variation can be found from the evolution of CV by analysis of consecutive scans. Different surface states exhibit distinct CV profiles in the HUPD region, where the hydrogen adsorption and desorption peaks are strongly related to the electrode surface crystal orientation [155]. In this region, the two hydrogen adsorption/desorption peaks, represent the sorption on (111) oriented surfaces and become more prominent during scans, which agrees well with literature [148]. As learned from the X-ray diffraction data, the surface of sputtered Pt thin films is (111) dominated but not exclusively, the trace of (100) peak already

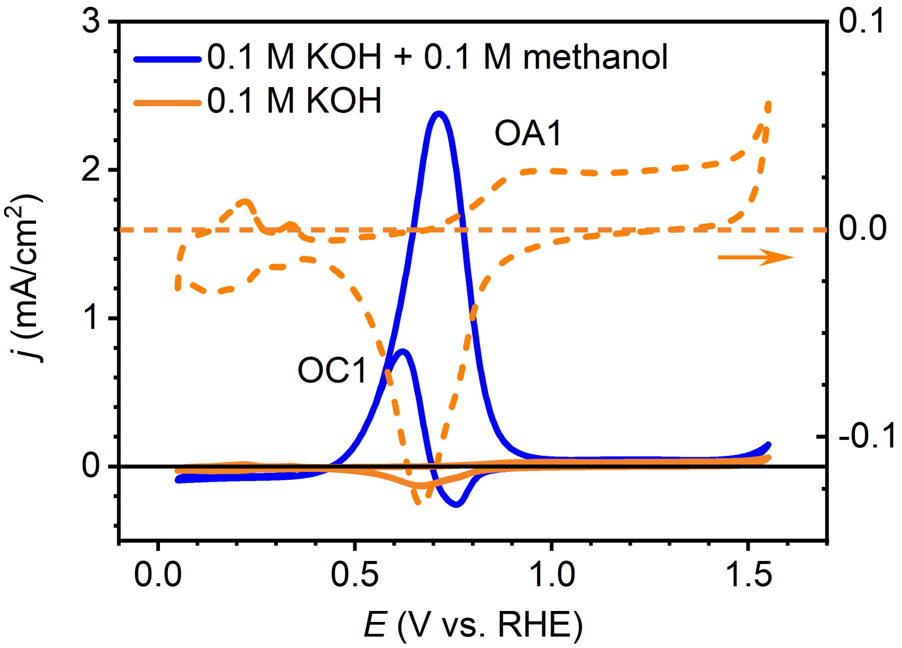

Figure 4.8: CVs of Pt in 0.1 M KOH supporting electrolyte (orange solid line, enlarged in orange dash line) and with added 0.1 M methanol electrolyte(bule solid line), scan rate of 20 mV/s

appears after the second scan. The first OH adsorption peak, which appears in the potential range of 0.65 - 0.7 V is the OH adsorption on (111) sites and gradually diminishes during subsequent scans. Following more than five repeated scans, all irreversible changes tend to diminish, reaching to a pseudo stable state on the surface. The representative CV of this steady state is depicted by the thicker solid line in Figure 4.6.

Figure 4.7 shows a series of CV measured in a KOH electrolyte, with a varying anodic potential limit of 1.235 V, 1.335 V, 1.435 V, and 1.535 V. As the anodic potential limit increases, a larger cathodic peak is observed, indicating oxygen reduction activity is related the surface oxidation extent. This suggests that oxygen is produced or adsorbed on the electrode surface during the anodic scan and subsequently reduced upon the cathodic sweep. The dependence of the cathodic peak intensity on the anodic potential limit further supports the idea that the oxygen species responsible for ORR are generated electrochemically at the electrode interface.

4.2.2 Methanol oxidation reaction on platinum surface

The mechanism of methanol oxidation reaction on Pt surface in alkaline electrolyte was investigated by using cyclic voltammetry (CV) and electrochemical impedance spectroscopy (EIS). Some experimental parameters were varied to provide more insights into the reaction mechanism, including the potential scan window of MOR, the voltage sweep rate and direction, the anodic and cathodic sweep vertex, and the methanol concentration.

Figure 4.8 shows the CVs measured on a polycrystalline Pt tip electrode with (blue solid line) and without (orange solid line, enlarged in orange dash line) 0.1 M methanol in 0.1 M KOH electrolyte. The methanol adsorption on Pt surface starts from a low potential within the double layer region around E = 0.42 V. The current increases dramatically during the initial stage of OH adsorption process and reaching peak at E = 0.72 V during the anodic scan. Following this peak, reactivity gradually decreases until it is completely vanished upon oxidation of the Pt surface. During the reverse scan direction, the partial reduction peak of Pt oxides can be observed at around the same potential, E = 0.8 V, as in supporting KOH electrolyte. Then this reduction peak was overlapped with the cathodic methanol oxidation peak. The concurrent peak was found at around $E = 0.6\,\mathrm{V}$, then superposed with the anodic methanol oxidation peak. Those characteristics are well-documented for the methanol oxidation reaction on Pt in alkaline solutions [20, 156, 157].

Figure 4.9 shows the results of adding an even smaller amount of methanol into 0.1 M KOH supporting electrolyte. During the positive scan, the reaction starts right after hydrogen desorption at around $E = 0.3\,\mathrm{V}$. The currents in the hydrogen region (enlarged area in Figure 4.9) decrease with increasing concentration of methanol. With more methanol in the electrolyte, the adsorption of methanol interferes with the hydrogen adsorption/desorption, resulting that the characteristic hydrogen peaks discussed before are inhibited. The methanol oxidation reaction is found to start earlier than OH adsorption, reaching maximum during the early stage of OH adsorption. When the Pt surface is fully covered by OH, the surface starts to form Pt oxides which shut down the reaction reactivity completely. During the backward scan, it is hard to determine the start potential of the cathodic methanol oxidation as it overlaps the reduction peak of Pt oxides which start from $E = 0.8\,\mathrm{V}$. The peaks of cathodic methanol oxidation reaction show up at the end of the reduction process, around $E = 0.55\,\mathrm{V}$, and it is the summation of both positive methanol oxidation current and negative oxygen reduction current. Thus, with higher methanol concentration, the cathodic methanol oxidation current is higher, but always smaller than the anodic methanol oxidation current during forward scan.

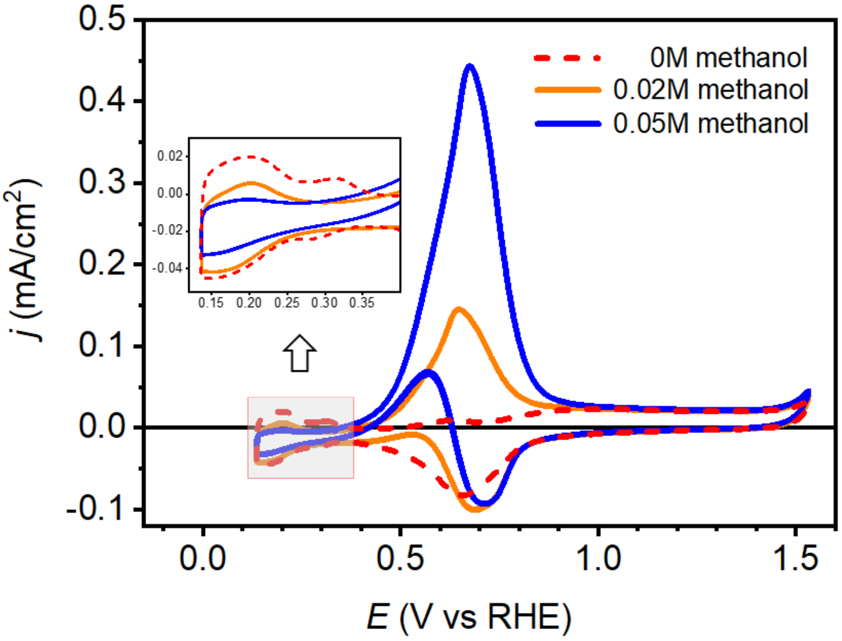

Figure 4.9: Cyclic voltammograms of methanol oxidation in 0.1 M KOH with small amount of methanol with scan rate of 20 mV/s.

Figure 4.10a presents the CVs of methanol oxidation reaction in the same condition as in Figure 4.8 but with varying scan rates. As the scan rate increases, both the anodic (OA1) and cathodic (OC1) oxidation peaks show a rise in the current density amplitude. However, OA1 and OC1 exhibit different kinetic processes as the ratios between peak current and scan rate are different, indicating a different surface state for these two methanol oxidation reactions. The scan rate has negligible effect on the positions of both peaks within this potential window. Notably, the current in the anodic potential region (OA2), where the surface with OH adsorption undergoes oxidation into Pt oxides, scales with the scan rate, while the current in the negative vertex region are independent of the scan rate.

Moreover, the potential difference between the two peaks ($E_{OA1} - E_{OC1}$) differs from that observed in Figure 4.8. To further explore this discrepancy, a similar scan rate dependency experiment was conducted across a broader potential range, as shown in Figure 4.10b. Methanol oxidation is intricately related to the degree of surface oxidation, influenced by both the upper limit of the anodic scan potential during the positive sweep and the processes of OH desorption and reduction of surface oxides during the negative sweep. In Figure 4.10b the anodic scan limit is set at 1.435 V, at this potential, according to Figure 4.6, the surface is fully oxidized and entering the initial stage of oxygen evolution reaction. With increasing scan rate, OA1 and OA2 increase with increasing scan rates. However, in contrast to the observations in Figure 4.10a, the cathodic peak (OC1) decreases with increasing scan rates. This discrepancy suggests that the surface states of the cathodic methanol oxidation are different and depend on the surface oxidation extent. In order to better understand the origin of this cathodic methanol oxidation peak, the scan limits in the anodic and cathodic scan directions were investigated individually.

It was observed that as the anodic potential limit was increased, more Pt surface was oxidized, resulting in a reduction in the current of the methanol oxidation peak (OC1). The forward methanol oxidation peak (OA1) remained independent of the varied anodic potential limit. However, the OC1 peak during the backward scan decreased with higher anodic potential limits. Additionally, the OC1 peak potential shifted negatively with increasing anodic scan limit. The upper potential limit determines the surface oxidation state, the higher potential, the surface is covered with more oxides, as a consequence, more negative potential is needed to provide a surface with enough active spots after surface oxides reduction.

Different from the anodic scan limits, all the methanol oxidation peaks are independent from the starting potential, namely the cathodic scan limit, as shown in Figure 4.11b. Different starting potentials result in the same oxidation current amplitude in both scan directions. This suggests that the hydrogen desorption process has minimal impact on the both oxidation currents, while the Pt surface OH adsorption and surface oxides formation processes are more relevant.

Figure 4.12 shows the results of methanol oxidation with different scan direction. Typically, the scan direction starts from a lower potential to a higher potential, noted as the anodic scan or forward scan, while the reverse scan direction is from a higher potential to a lower potential, so called as the cathodic scan or backward scan. From Figure 4.12, the CVs completely overlap during both forward and backward scans, indicating the methanol oxidation peak during backward sweep is unrelated to the residual intermediate which are formed during forward scan. In other words, these two methanol oxidation peaks are independent from the possible transition product of each other.

Electrochemical impedance spectroscopy (EIS) of methanol oxidation on Pt

EIS was carried out at different potentials to identify processes during methanol oxidation reaction by applying sinusoidal signals with a wide range of frequencies (different time constants). EIS was also employed simultaneously with CV, also known as Dynamic Electrochemical Impedance Spectroscopy (DEIS) or AC voltammetry. In Figure 4.13a, six different potentials were selected to conduct impedance measurement at a steady state. Label A is at $E = 0.435\,\mathrm{V}$, the beginning stage of methanol oxidation reaction. From Figure 4.13b, the large semicircle in this region indicates an adsorption process, also a nearly 80 degree phase shift in 4.13c, which facilitates this capacitive behavior, ions accumulate at the interface such as the methanol dehydrogenation and its adsorption according to reaction 4.4

$$\mathrm{Pt{-}(CH_3OH)_{ad} + OH^- \longrightarrow Pt{-}(CH_3O)_{ad} + H_2O + e^-} \tag{4.4}$$

When the potential is increased to the half peak position at point B (E= 0.635 V), significant changes are observed in both the Nyquist plot and the Bode plot. In Figure 4.13 d, a second semicircle emerges in the low-frequency region, resulting in a pseudoinductive behavior where two distinct semicircles (a large one in the high-frequency region and a small one in the low-frequency region) coexist in the Nyquist plot. The semicircle in the high-frequency region becomes much smaller compared to the one at point A, showing a decrease in impedance with

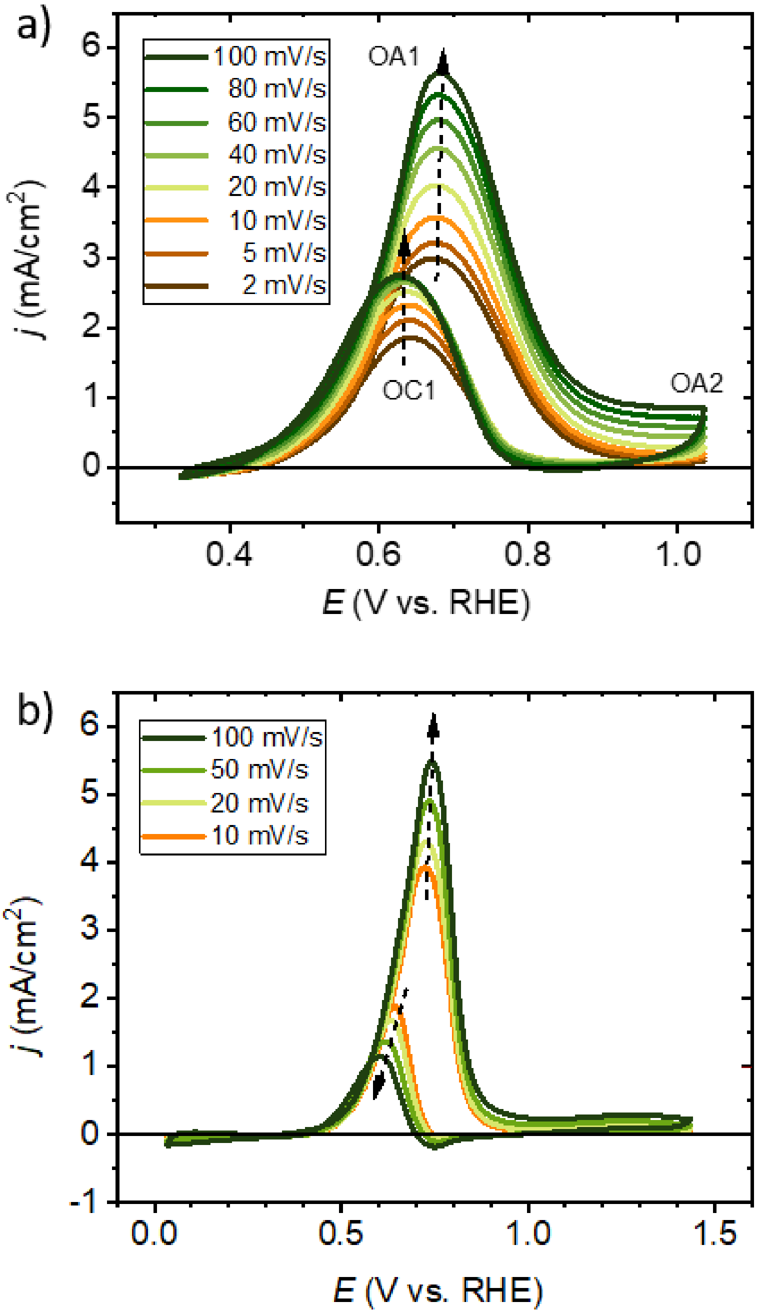

Figure 4.10: a) Cyclic voltammogram of methanol oxidation reaction with different scan rates in 0.1 M KOH with 0.1 M methanol electrolyte, from 2 mV/s to 100 mV/s, in a small potential window (without the region of surface oxidation processes and HUPD region.) b) CV measured on the same sample and electrolyte as a), scanned from 10 mV/s to 100 mV/s, but in a wider potential window (including the region of surface oxidation processes and HUPD region)

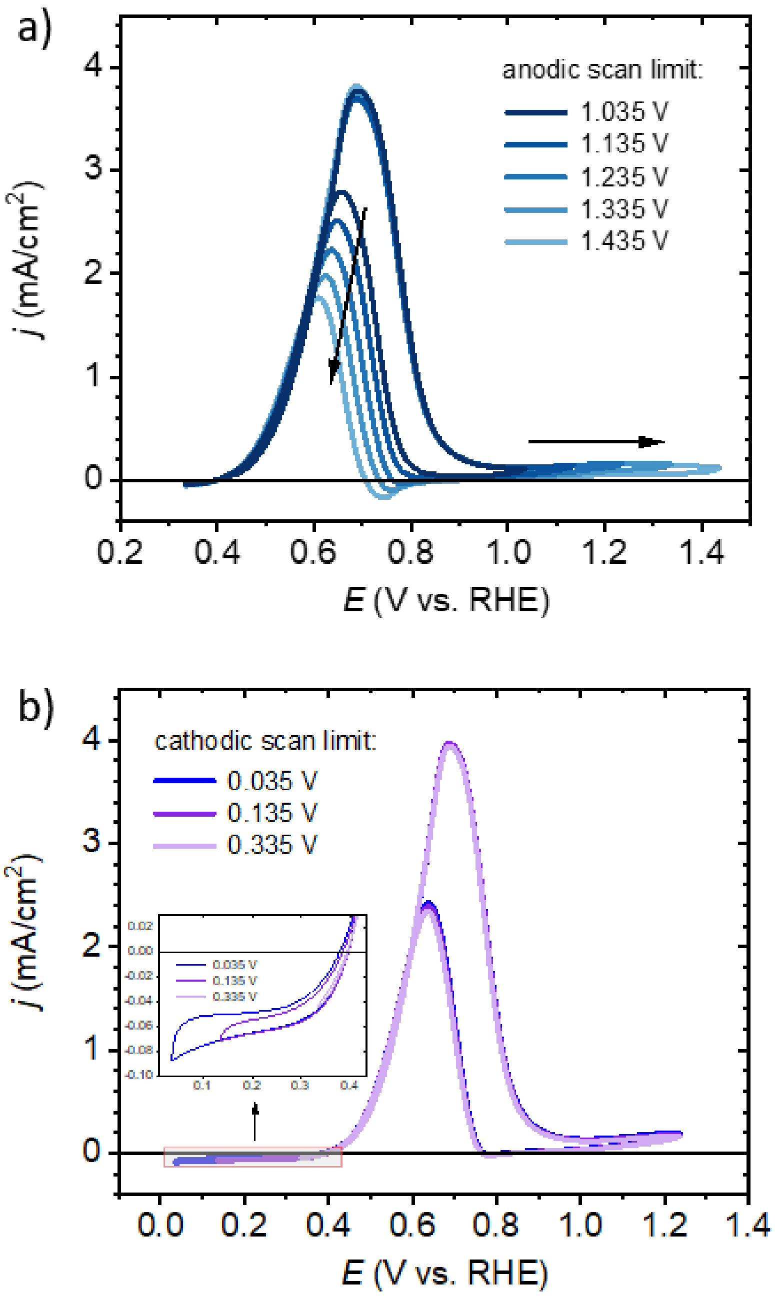

Figure 4.11: a) Cyclic voltammogram of methanol oxidation reaction with the same cathodic vertex but different anodic potential scan limit in 0.1 M KOH with 0.1M Methanol electrolyte. b) CV measured in the same condition as a), but with different cathodic potential scan limit and the same anodic limit in 0.1 M KOH with 0.1 M ethanol electrolyte.

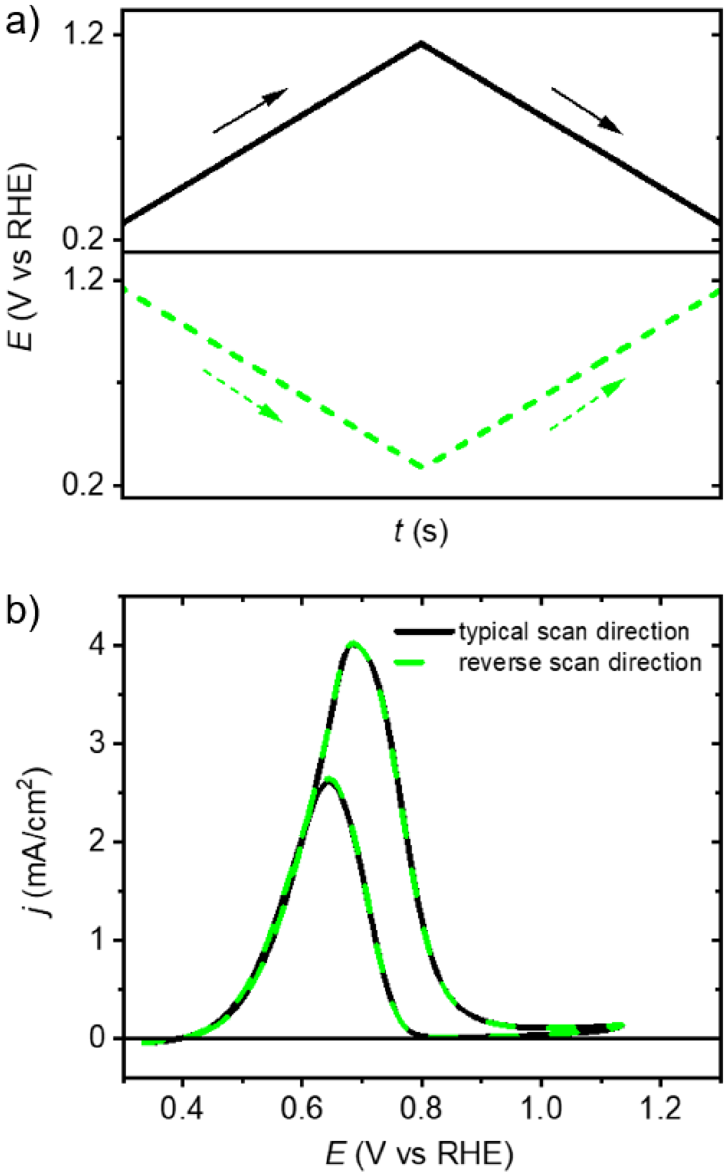

Figure 4.12: Cyclic voltammogram of methanol oxidation reaction with different scan direction in 0.1 M KOH with 0.1 M Methanol electrolyte. The black line shows the forward scan direction from 335 mV to 1135 mV, the green line is the opposite scan direction.

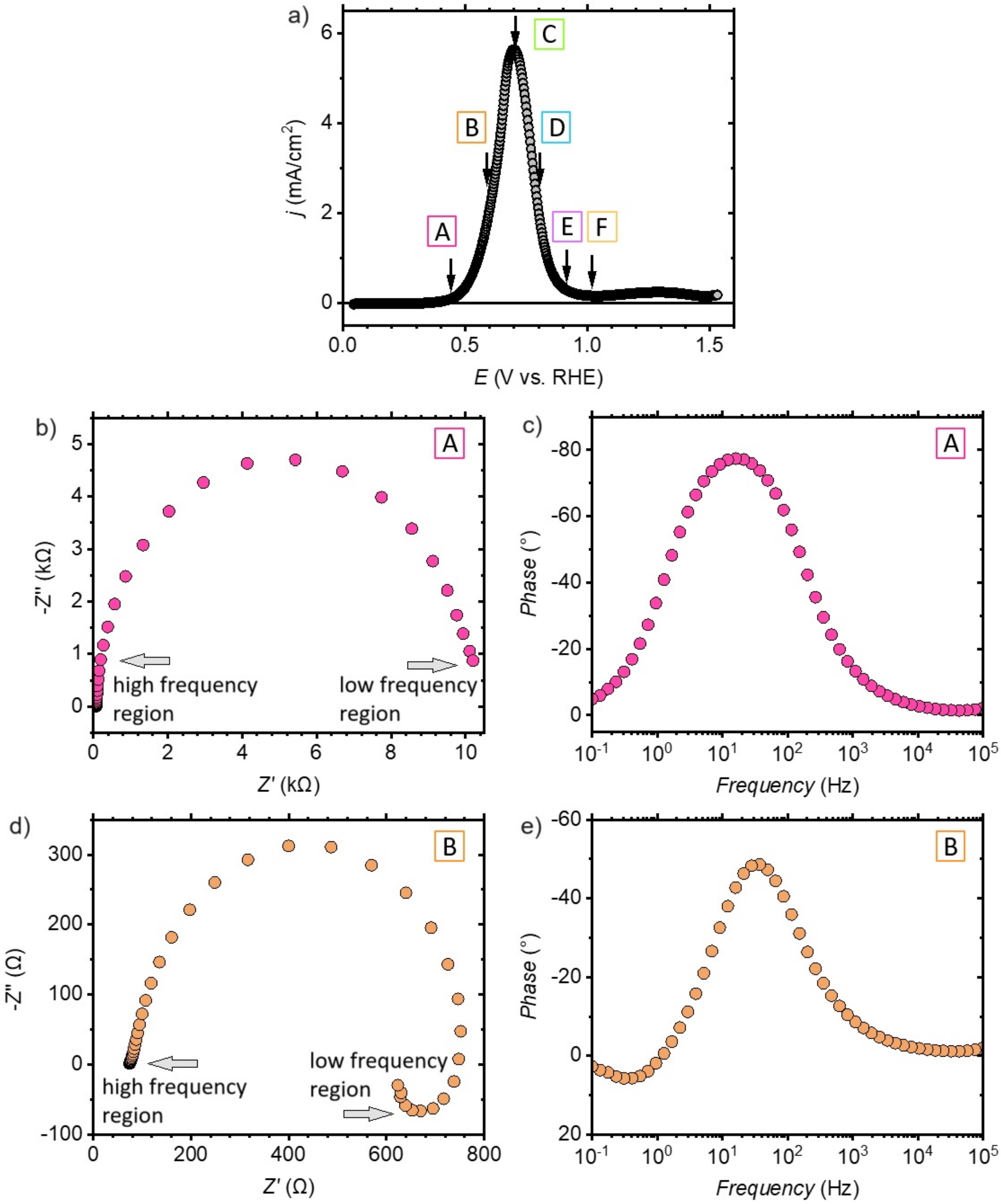

Figure 4.13: (a) current density versus potential on Pt in 0.1 M KOH with 0.1 M methanol. (b) (c) are the Nyquist plot and Bode plot measured at the potential of 0.435 V and indicated in (a) as A. (d) (e) are the Nyquist plot and Bode plot measured at the potential of 0.635 V and indicated in (a) as B. Frequency range is from 100k Hz to 0.1 Hz with amplitude of 10 mV.

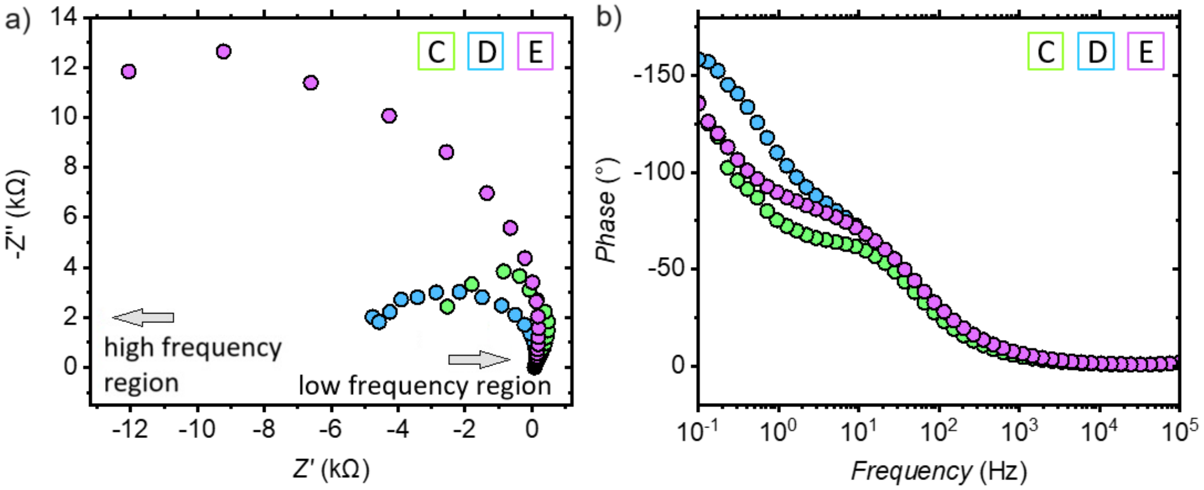

Figure 4.14: (a) is the Nyquist plots and (b) is the Bode plots measured at the potential of 0.735 V, 0.835 V, 0.885 V individually and indicated in Figure 4.13(a) as C, D, E.

increasing potential, indicating more efficient charge transfer process. The second smaller semicircle in the low frequency region shows a typical inductive behavior, which is known for the reactions through intermediates [158–160]. Consequently, an increase in current is observed in the CV, which is attributed to the oxidation of methanol intermediates at the electrode surface.

This pseudoinductive behavior, characterized by an inductive response in the EIS measurement, is well-known for reactions involving intermediate species. In such cases, the rate-determining step is the conversion of intermediate species to product. The appearance of small semicircle in the low-frequency region indicates the involvement of this intermediate species in the reaction pathway. It also worthy to note that no track of diffusion effects are observed in the impedance data for the concentration of methanol used. Also in the Bode plot, with increasing potential, the peak of phase angle decreases down to about 50 degree and shifts to high frequency. As the potential increases, the surface coverage of adsorbed OH increases, inducing an enhanced process from intermediate to product and leading the system to transition to a state where charge transfer resistance becomes more prominent, which reduces the capacitive behavior.

At even higher potentials 0.735 V, 0.835 V, and 0.885 V (point C, D, E respectively), a notable change occurs in the primary semicircle of the Nyquist plots comparing to lower potentials, as it flips from the first quadrant to the second quadrant within a narrow potential range, as shown in Figure 4.14a. This behavior is typical in methanol oxidation at these potentials and has been reported in several studies [158–162]. The arcs reverse while the reaction current is going down, moving into the second quadrant, and their diameters increase as the potential continues to rise. In this region, with increasing potential, at least three step reactions are processing at the same time. One reaction is the process of OH adsorption leading to an increasing coverage of PtOH. Then at higher potential, the adsorbed PtOH is oxidized into PtO. The third one is the oxidation of the intermediates. In Figure 4.14a, the size of the arc increases with higher potentials, indicating an increase in impedance as the potential is raised, resulting in a declined current in this region. The high resistance at point E implies that the electrochemical system is experiencing sluggish kinetics or that there is significant impedance from the adsorbed intermediates such as adsorbed OH groups or other factors at this higher potential. Additionally, in Figure 4.14b, the appearance of peaks shifts to the low-frequency region indicates changes in the characteristic frequencies of the electrochemical processes. A clear transition state can be found around potential D in small frequency range in the Bode plots of Figure 4.14. With increasing potentials, the coverage of adsorbed OH continuously increases, and the reaction of intermediates turning into products is no longer the rate-determining step. Large negative phase angles at C,D,E at lower frequencies, namely a high delay in current response relative to voltage,

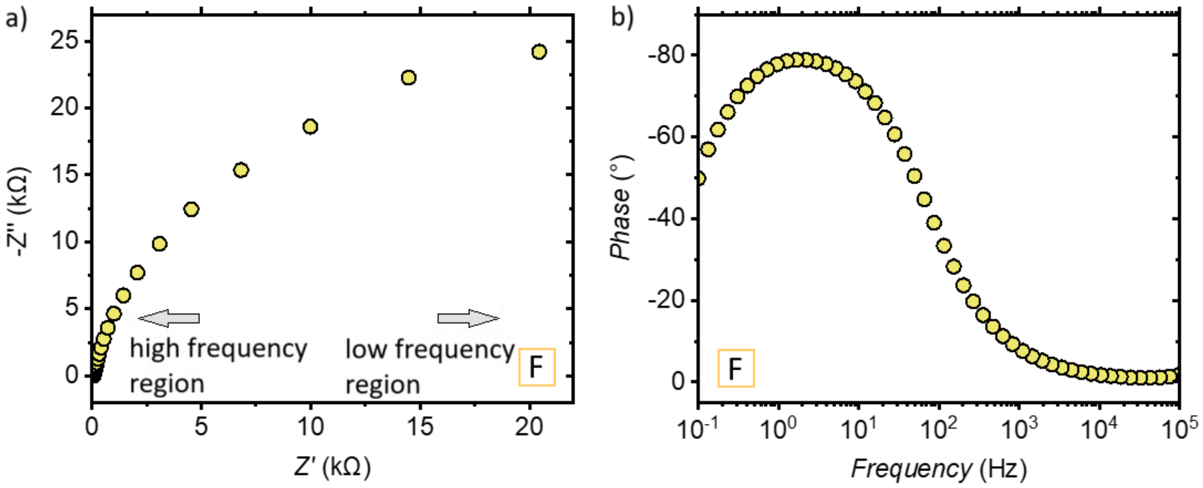

Figure 4.15: (a) is the Nyquist plot and (b) is the Bode plot measured at the potential of 1.035 V and indicated in Figure 4.13 (a) as F.

suggests complex impedance behavior that could be related to adsorption/desorption processes at the electrode surface and caused by the buildup and transformation of intermediates on the electrode. As a result, the process of methanol being oxidized into intermediates becomes the limiting factor for the MOR.

At a potential of 1.035 V, as depicted in Figure 4.15, the methanol oxidation process is concluded, and no further oxidation current from methanol is observed. At this potential, the surface is dominated by the Pt oxides species, which is believed the reason to shut down the whole oxidation reaction. The PtO formation from PtOH at or above 0.96 V has been confirmed through *in situ* X-ray absorption structure analysis [163]. A new arc with larger diameter emerges in the first quadrant of the Nyquist plot, suggesting the initiation of a different electrochemical reaction process on the electrode surface. A similar pattern is discernible in the Bode diagrams, where a resistive behavior emerges at high frequencies, peaking at intermediate frequencies.

4.3 Surface stress variation on Pt

4.3.1 In base electrolyte

The cantilever bending technique was employed to evaluate the surface stress of the Pt electrode during electrochemical reactions in electrolytes. *In-situ* measurements of surface stress, denoted as Δf, were conducted on an 80 nm thick Pt film deposited onto a 100 µm thick silicon substrate in a 0.1 M KOH solution at a scan rate of 20 mV/s.

Figure 4.16 illustrates the current density j, and the variation, Δf, in surface stress which was measured simultaneously with the CV of Figure 4.16a in 0.1 M KOH, and the result is shown in Figure 4.16b. It is important to note that only changes, not absolute values of f can be measured, and the cathodic vertex was set to zero as a reference starting point. Figure 4.16 presents the records of six continuous scanning loops, revealing that from the second round, the surface entered a quasi-steady state, both CV and stress variation curves remain reproducible behaviors during scans. The scan directions are indicated by black arrows in Figure 4.16b. The systematic downward shift of the CV at $E < 0.5$ V suggests a noticeable oxygen reduction reaction current. This arises from molecular oxygen that is generated near the anodic vertex of the CVs and that cannot be removed here since our *in situ* experiments are not compatible with bubbling. The CVs exhibit only small drift, suggesting essentially stable behavior of the thin-film electrodes under repeated potential cycles.

The surface stress evolution shows characteristic behaviors in the three regions: in HUPD

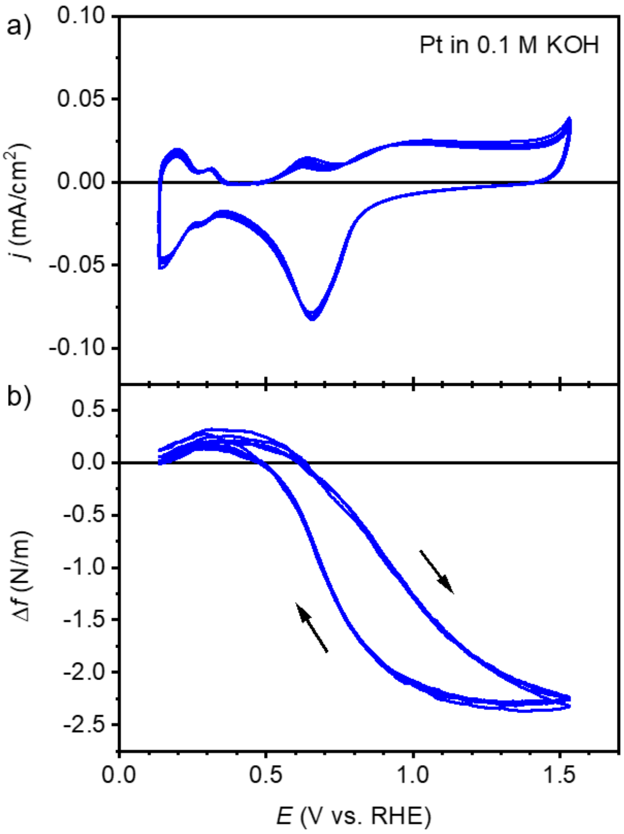

Figure 4.16: Results of *in situ* cantilever bending experiment on Pt in 0.1 M KOH. a) Cyclic voltammogram of Pt on Si substrate at a scan rate of 20 mV/s. b) Simultaneous measurement of surface stress variation, Δf, with the CV in a). Black arrows indicate the scan directions.

region (from cathodic vertex to 0.35 V), during anodic scan, the surface becoming more tensile stress; in double layer region (from 0.35 V to 0.5 V), the surface stress exhibits a maximum at around $E = 0.36$ V, which is in an agreement with literature [164]; in the surface oxidation region (above $E = 0.5$ V), a change of compressive surface stress observed in the oxide formation region starting at 0.3 V with a much higher total variation of surface stress value (about 2.5 ± 0.1 N/m) than the total tensile surface stress (around 0.3 ± 0.1 N/m) in HUPD region, which is also in a good agreement with findings from previous studies [165, 166]. In the cathodic scan, f initially varies slowly. Upon oxygen desorption, f recovers rapidly to the positive value in approach to the cathodic vertex, with a final drop upon HUPD. The hysteresis in the surface stress reflects the oxygen species adsorption/desorption hysteresis of the CV.

Importantly, Figure 4.16b qualifies the drift in the surface stress isotherm as negligible over repeated cycles. That confirms the reversibility of the electrode processes, and specifically it rules out the conceivable growth and gradual thickening of an irreversibly deposited surface oxide layer during the recording scans.

It is important to note that for films that exhibit anisotropic behavior and develop a biaxial stress state with principal stresses σ_x and σ_y oriented along the horizontal and vertical axes respectively, the curvature may differ in these two orthogonal directions. Figure 4.17 illustrates the signals obtained from the horizontal direction and vertical direction. The close overlap between these signals suggests minimal interference from the mounting process. Additionally, over the cyclic scanning, only the first scan is about removing potential contaminates thus exhibiting a slight higher signal, the residual scans showing consistent and stable behavior without drifting during the oxidation and reduction processes. This indicates that the there is no irreverible increase in the oxygen coverage on the electrode surface, in any potential regime.

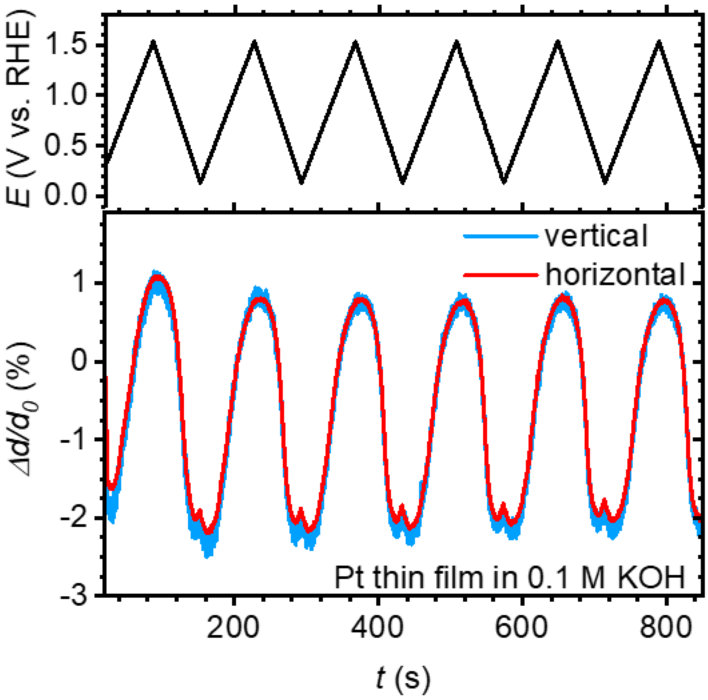

Figure 4.17: Cyclic potential scanning of the electrode and the variation of the differential spot spacing, which is measured simutaneously over time.

4.3.2 In lower concentration of methanol electrolyte

In Figure 4.18 and 4.19, CVs and corresponding surface stress variations are presented for electrolytes with different concentrations of methanol. Figure 4.18 shows the case with lower

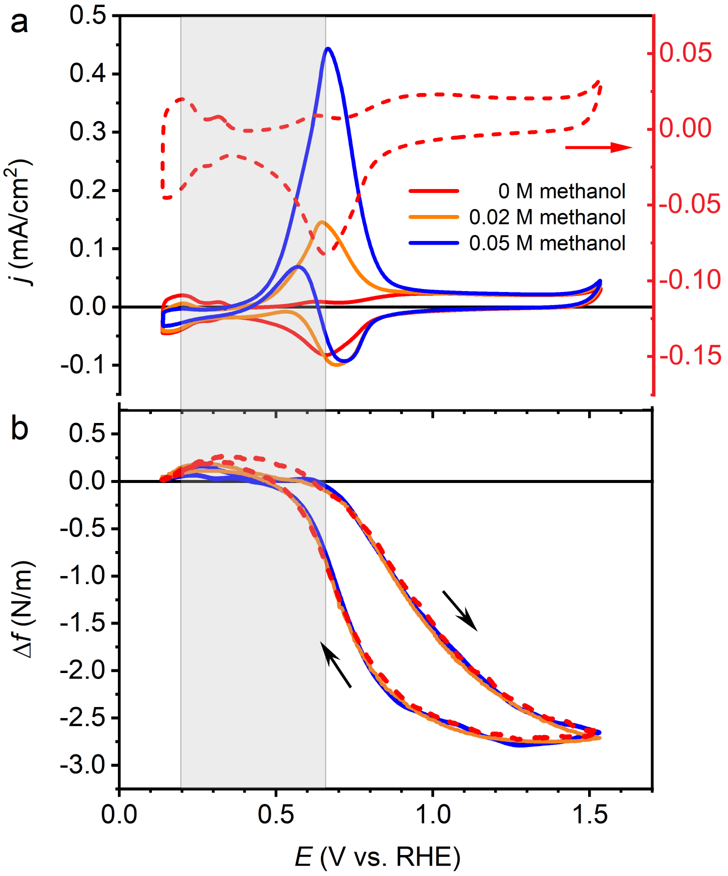

Figure 4.18: Results of *in situ* cantilever bending experiment on Pt electrode in the electrolyte with different concentration of methanol from 0 M to 0.05 M, as indicated in legend. a) cyclic voltammograms of current density, j versus applied electrode potential, E (vs. RHE), b) surface stress, Δf versus electrode potential measured simultaneously with the CVs in a), red dashed lines in both are the ones measured in 0.1 M KOH solution without methanol as base solution.

methanol concentration, specifically at 0.02 M and 0.05 M, while Figure 4.19 is about higher methanol concentration, ranging from 0.1 M to 0.5 M. All electrolytes are in a base solution of 0.1 M KOH.

Figure 4.18a illustrates that CVs with varying methanol concentrations exhibit typical characteristics. On top of that, it also shows the influence of methanol concentration on HUPD region currents. Higher methanol concentrations lead to smaller hydrogen adsorption/desorption currents, as methanol adsorption competes for active sites with hydrogen adsorption. The magnitude of the reaction current increases with higher methanol concentrations in both the anodic and cathodic scan oxidation peaks. The cathodic oxidation peak in 0.02 M methanol containing electrolyte is negative, as it partially overlapped with the oxygen reduction current, and showing an overall negative current due to a small methanol concentration. The potential of the maximum reaction current remains constant as methanol concentration increases. The currents associated with oxygen adsorption/desorption in higher potential windows remain consistent across all electrolytes, regardless of methanol concentration.

In Figure 4.18b, surface stress in methanol-containing electrolytes initially shows a small increase, showing a similar early stages of the HUPD lifting signature observed in base KOH electrolyte. However, the most positive values of Δf remain below those in KOH. With methanol, surface stress data shows a short plateau of surface stress until the potential reaches the peak current at approximately $E = 0.68\,\mathrm{V}$, indicating that during methanol oxidation, a distinct phase occurs within a narrow potential range until reaching the potential of the current peak, beyond which the overall surface behavior aligns with that of the methanol-free electrolyte. There is no distinct transition point between the dehydrogenation of methanol and the adsorption of these intermediates. During the cathodic scan, there are no significant changes in surface stress observed in the methanol-containing electrolyte. Although it was expected that a similar behavior would occur, with surface stress remaining at zero during the second methanol oxidation peak, the very small currents in the cathodic scans make it challenging to precisely determine the starting potential of the cathodic methanol oxidation peak based on the surface stress variation data.

4.3.3 In higher concentration of methanol electrolyte

Figure 4.19a presents the CVs with higher concentrations of methanol in the electrolyte. The characteristics of the CVs closely resemble those discussed previously. Additionally, there is a clear positive shift of the oxidation peaks during the anodic scan, a distinct feature compared to lower methanol concentrations. For $c_{\mathrm{Methanol}} = 0.1\,\mathrm{M}$, the cutoff potential is less pronounced compared to higher concentrations but aligns with the initiation of oxygen sorption in the supporting electrolyte.

From Figure 4.19b, near the cathodic vertex of the CVs, the surface stress variation is similar to that for the lateral concentrations. Again, the onset of the MOR does not exhibit a distinct signature in the surface stress graph. The trend for the drop in surface stress shifts to more positive potentials as c_{meth} increasing and becomes even more pronounced. Significantly, f is seen to drop precisely onto the graph for the base electrolyte and to then continue in agreement with that latter graph. Apparently, the reaction continues to efficiently consume all adsorbed oxygen species up until the reactivity has completely ceased. During methanol oxidation peaks, the stress variation remains consistent, suggesting either an insignificant coverage of adsorbed methanol intermediates or a weak bond between the surface Pt atoms and the adsorbed methanol intermediates.

During the cathodic scan, the $f(E)$ curves for all three electrolytes follow a consistent trend, overlapping in the oxygen reduction region. This overlap persists until the potential at which the methanol cathodic oxidation reaction starts. A minor shift in $f(E)$ occurs around $E = 0.6\,\mathrm{V}$, corresponding to the cathodic methanol oxidation peaks seen in Figure 4.19a. At this point, the surface stress reverts to the plateau region before rejoining the curve corresponding to the

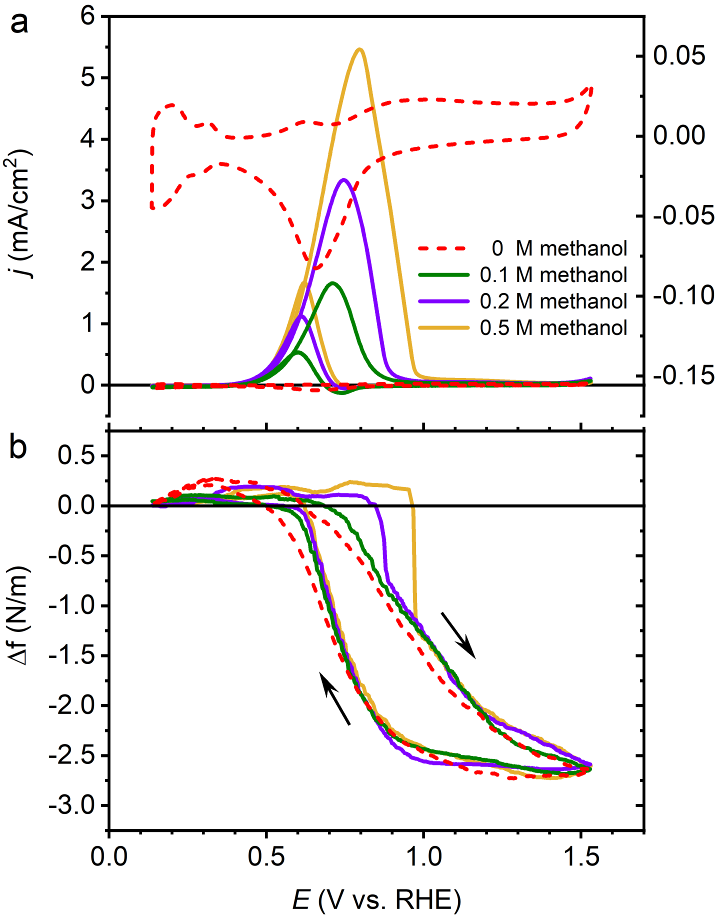

Figure 4.19: Results of *in situ* cantilever bending experiment on a Pt electrode in the electrolyte with different concentration of methanol from 0.1 M to 0.5 M, as indicated in legend. a) cyclic voltammograms of current density, j versus applied electrode potential, E, b) surface stress, Δf versus electrode potential measured simultaneously with the CVs in a).

supporting electrolyte.

Above, we have suggested that the CVs for the highest methanol concentrations in our study may contain artifacts from an incomplete uncompensated resistance correction, owing to the very high currents. It is therefore important to re-emphasize that current and surface stress were measured simultaneously in all our experiments. Features in the graphs of those two quantities can therefore be correlated one-to-one, irrespective of a possible distortion of the CV due to the uncompensated resistance.

4.4 Dynamic Electro-Chemo-Mechanical Analysis (DECMA) on Pt electrode

Strain effect on Pt surface oxidation and reduction in alkaline electrolyte

DECMA has been proved to be an effective method to investigate strain effect on electrocatalytic reactivity during electrochemical reactions. Before exploring the strain effect on the methanol oxidation process, the impact of strain on Pt during surface oxidation and reduction was examined first to investigate the coupling between strain and adsorbed surface oxygen molecules. Additionally, the oxygen reduction reaction (ORR) was conducted to gain deeper insights into the strain modulated oxygen adsorption and desorption processes.

Oxygen reduction reaction(ORR) is the most important cathodic reaction of many fuel cell devices. In the ORR, molecular oxygen is electrochemically reduced by four protons and electrons to form water, which is accompanied by generation of an electrical potential. There are, in general, two pathways to reduct the oxygen in alkaline environment. One is the the direct way, which contains four electrons transfer:

$$O_2 + 2H_2O + 2e^- \longrightarrow 4OH^- \tag{4.5}$$

the other one is through the indirect pathway with two electrons transfer at each sub reactions:

$$O_2 + H_2O + 2\,e^- \longrightarrow H_2O^- + OH^- \tag{4.6}$$

$$H_2O^- + H_2O + 2\,e^- \longrightarrow OH^- \tag{4.7}$$

Figure 4.20 shows the results of CV and current-strain coupling coefficient of ORR on Pt electrode. In Ar, during OH adsorption process, $\hat{\jmath}$ increases and reaches to peak at $E = 0.78\,\mathrm{V}$. When the surface is fully covered with oxides, $\hat{\jmath}$ still remains positive but decreases till right before oxygen evolution reaction. External tensile strain induces a positive modulation current during the whole oxidation process, in other words, enhancing the surface oxygen adsorption in terms of the PtOH at lower overpotential and PtO at higher overpotential. During the initial reduction process (from anodic vertex), the oxidized surface stay inert towards external strain modulation.

A similar behaviour was found in oxygen as well, as the surface oxidation state does not depend on atmosphere. During the oxygen reduction process, which happens during backwards scan, from $E = 0.8\,\mathrm{V}$, the cathodic current increases dramatically and $\hat{\jmath}$ starts to increase and stays positive until the end of ORR. Thus, tensile strain is confirmed to exhibit a positive effect on ORR process on Pt electrode. This is a promising sign to look into more details about the tensile strain effect on ORR reaction.

Strain effect on electrocatalytic oxidation of methanol on Pt

Figure 4.21 shows the CVs and DECMA results on Pt electrode subjected to an external sinusoidal strain signal of 20, 30, 40 Hz in 0.1 M KOH and 0.1 M methanol electrolyte. The three CVs in Figure 4.21a overlap quite precisely, indicating a steady state electrode behavior during

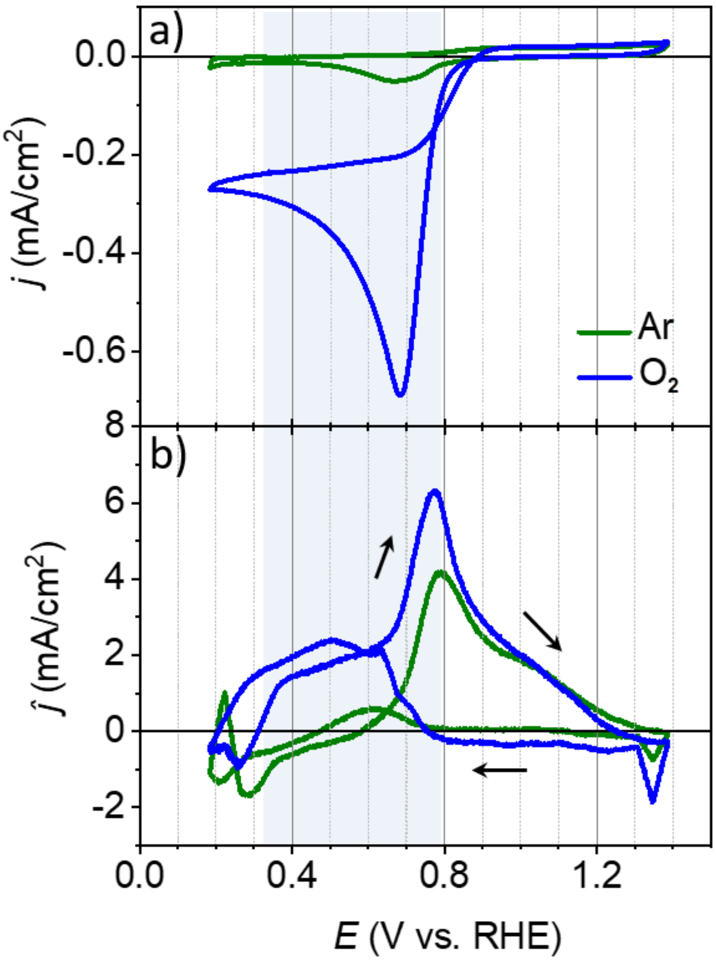

Figure 4.20: a) Cyclic voltammogram of Pt electrode in 0.1 M KOH electrolyte in different atmosphere. The green one is in Ar, and blue one is in O_2. Scan rate is 20 mV /s. b) results of current-strain potential response which was *in situ* measured with CV at frequency of 20 Hz. Arrows indicate the scan direction.

the whole measurement. Figure 4.21b shows the real part, $\hat{\jmath}_{\mathrm{re}}$, of the current-strain response. As the most significant observation, $\hat{\jmath}_{\mathrm{re}}$ is negative-valued in the region of the main anodic methanol oxidation peak. In other words, tensile strain reduces the catalytic activity of Pt for the methanol oxidation reaction, with this effect peaking near a potential of 0.78 V during the latter stages of the oxidation process. In the main methanol oxidation regime, there is no noticeable frequency dependence, confirming that the signal can be identified with a strain dependence of the reaction current. Moreover, in Figure 4.21c, the magnitude, $|\hat{\jmath}|^2 = (\hat{\jmath}\mathrm{re})^2 + (\hat{\jmath}\mathrm{im})^2$, of the complex current-strain response signal closely exhibits the similar features of the real part, suggesting that the real part is indeed the dominant signal. Given that the real part reflects the reaction current-strain response according to $\iota = dj^F/de$, this observation further validates the DECMA data as indicative of the current-strain coupling for the methanol oxidation reaction.

The current-strain response appears negligible in the extended potential above 0.9 V, suggesting that strain modulation in this potential regime does not couple significantly to either Faraday or pseudo-capacitive processes. This aligns with the dominance of oxygen species adsorption and the observed strong hysteresis for oxygen adsorption on Pt, indicating that adsorbed oxygen species, which drive surface stress towards more negative values in this potential range, do not couple to strain at the frequency of strain modulation. The methanol oxidation current peaks in the cathodic scan are accompanied by a slight excursion of the current had and strain response graphs towards negative. This is consistent with the sign of the response that is observed during the anodic scan. Here again, the maximum of the response is only found when the reactivity already decays.

Figure 4.22 presents the results from the AC voltammetry measurement, which was studied for facilitating the analysis of the DECMA data with an effect of resistance variation during the strain modulation. Here, we mainly study the main MOR peak during the anodic scan direction, as it demonstrates a notable strain-induced effect on current response. Impedance measurements were conducted at a frequency of 20 Hz, which is the same as the external applied strain frequency. It can be seen in the Figure 4.22b that the real part of impedance (resistance component associated with Faraday processes) becomes dominate from the early stage of the MOR, around $E = 0.5\,\mathrm{V}$, and showing the highest resistance around $E = 0.62\,\mathrm{V}$. This increase in resistance is evidently attributed to the methanol reaction resistance, agrees well with our EIS data. When the Pt surface starts to adsorb OH at around $E = 0.74\,\mathrm{V}$, namely the later stage of the reaction, the resistance stays nearly constant. The imagery part of the impedance decreases during the methanol oxidation current, and showing a shoulder at $E = 0.63\,\mathrm{V}$, then reaching minimum at the $E = 0.78\,\mathrm{V}$. Accordingly, in Figure 4.22c, at the frequency of 20 Hz during the main MOR process, the real part of AC current is dominate and reaching maximum at the potential about 0.78 V, which shows a very similar tendency as the DECMA current-strain response result. Also, the imagery part of AC current stays much less prominent as expected.

Figure 4.23 shows the result of the current-strain coupling parameters with consideration of the uncompensated resistance effect in the electrochemical system as introduced in Chapter2.4.6. The τ_{re} and τ_{im} are derived from the currents of AC voltammetry in Figure 4.22c. The peak value of the τ_{re} at $E = 0.72\,\mathrm{V}$ was used for the correction calculation of intrinsic value of λ in Figure 4.23b. Despite corrections, the general trend remains consistent, with no alteration in the positions of sign-changing points. However, the maximum value experiences a slight negative shift of 0.1 V, alongside an approximate 7.9% increase in amplitude.

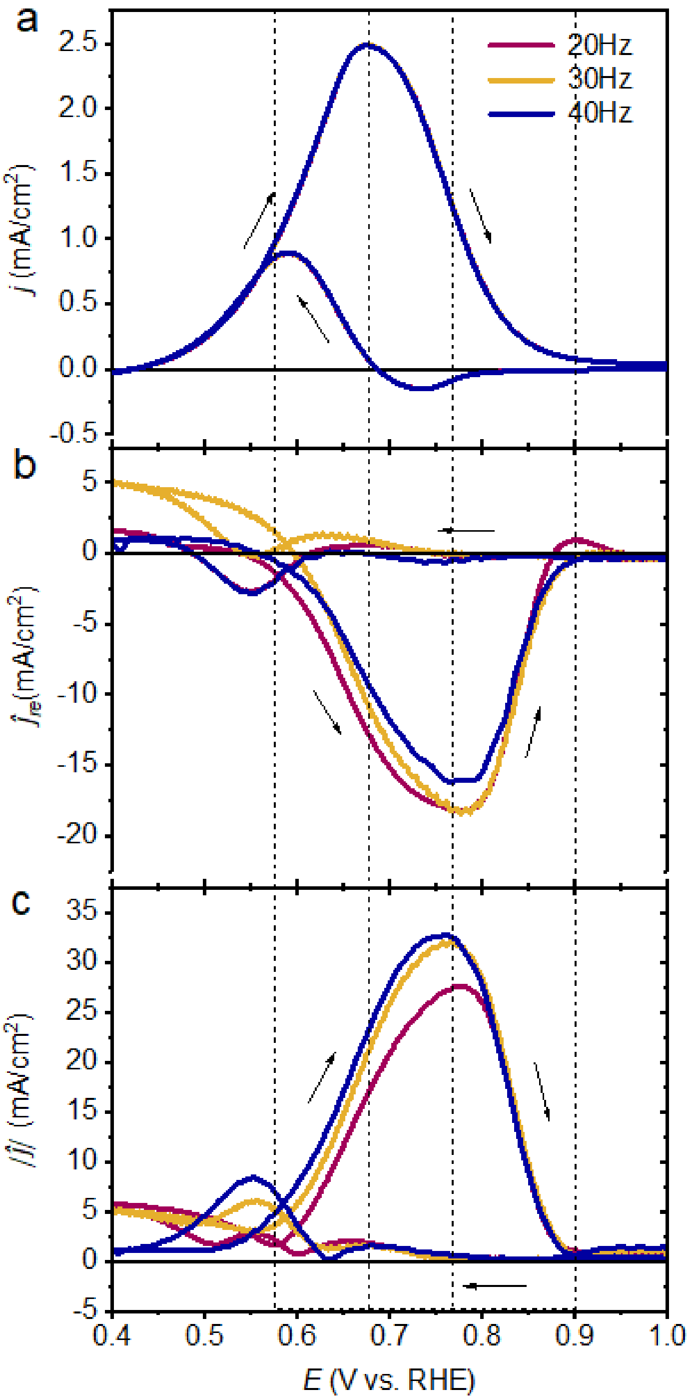

Figure 4.21: Results from Dynamic-Eelectro-Chemo-Mechanical Analysis (DECMA) with external strain frequencies of 20, 30, 40 Hz on Pt electrode in 0.1 M KOH with 0.1 M methanol. a) CVs of MOR at different strain frequencies, with a scan rate of 20 mV/s. b) The real part of the current-strain response, denoted as $\hat{j}_{\mathrm{re}}$, obtained from the lock-in amplifier, simultaneously measured with the CV scans in panel a). c) Magnitude of the current-strain response, $|\hat{j}|$. Scan directions are indicated by black arrows in all Figures.

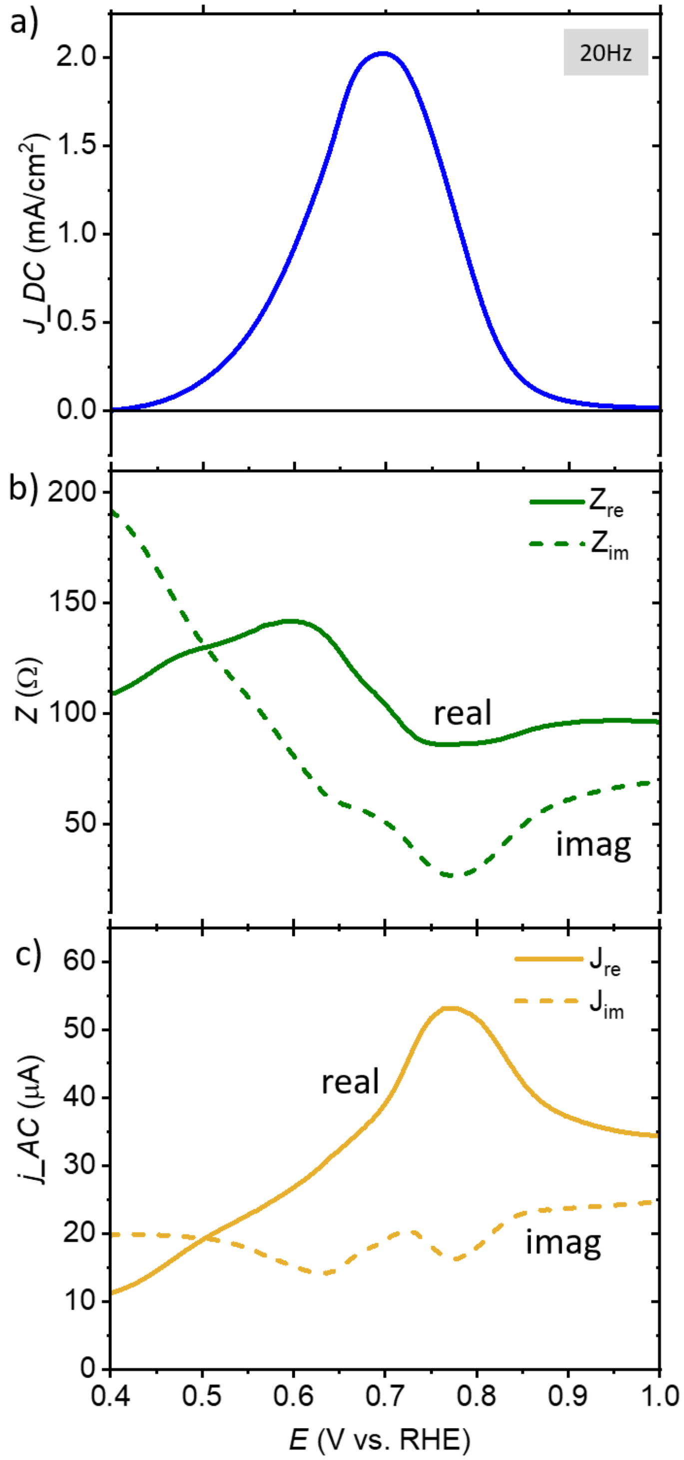

Figure 4.22: a) base current density, j, versus potential during anodic scan. b) The real and imagery parts of impedance measured under the perturbation voltage. c) The real and imagery parts of the alternative current caused by the AC voltage. The applied perturbation voltage was with a frequency of 20 Hz and a modulation amplitude of 0.005 V_{RMS}. The scan rate was 5 mV/s.

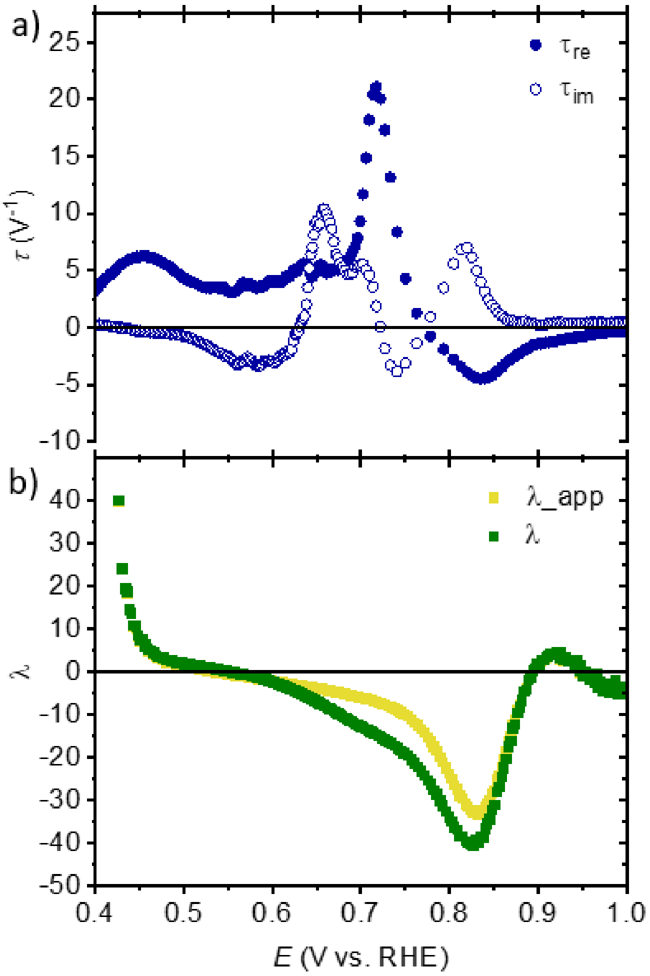

Figure 4.23: The results of current-strain response parameters and the IR correction of it. a) the current response to applied perturbation voltage in the form of $\tau = \mathrm{d}\ln j/\mathrm{d}E$. b) The current strain response with IR correction from Equation 2.76

Chapter 5

Discussion

5.1 Mechanism of methanol oxidation reaction on platinum in alkaline solution

5.1.1 Methanol oxidation process during anodic scan

The electrochemical mechanism for methanol oxidation is complex with six electrons transfers in total, and containing several step reactions as introduced in the theory chapter (Equation 2.77), and is also illustrated with CV as shown in Figure 5.1. The theoretic reaction pathway includes methanol adsorption, dehydrogenation and formation of carbon-containing intermediates, and the final production of carbon dioxide.

The first step of methanol oxidation is the adsorption of methanol molecule on Pt surface, which has been proved, also in this study, to happen at a very early stage of the potential window. In an alkaline electrolyte, where hydrogen concentration is relatively low, methanol adsorption becomes more prominent in the HUPD region. As a result, the adsorption and desorption peaks of hydrogen diminish at higher methanol concentrations. This indicates that methanol adsorption selectively suppresses strongly bound hydrogen species in an alkaline solution while having less impact on weakly bound hydrogen on the Pt surface.

Following methanol adsorption, the oxidation process is triggered by the adsorption of OH species, which plays a critical role in the overall reaction mechanism. The adsorption of OH not only facilitates the dehydrogenation of methanol but also regulates the reaction rate. Importantly, this step can be modulated by external strain on the Pt surface, which influences OH adsorption and, consequently, the overall methanol oxidation reaction rate. This insight represents a key conclusion of this thesis and will be further discussed in the final section of this chapter.

The main anodic oxidation current starts rapidly once OH species adsorbed onto the Pt surface, then methanol typically dehydrogenates into formaldehyde and formate in alkaline environment, which can be further dissociated to CO_2 and ${CO_3}^{2-}$ (in solution). Even though CO is often considered as a poisoning byproduct during this process, in most cases in alkaline electrolyte, it can also be oxidized by adsorbed OH and continue to be consumed according to the following equation: $CO_{ads} + 2OH^- \longrightarrow CO_2 + 5H_2O + 2e^-$.

MOR activity is highly affected by CO adsorption, and the removal of CO_{ads} depends on the OH concentration in electrolyte. Higher concentration of OH can help oxidize CO and accelerate the reaction rate [167], however, excessively high concentrations of OH in DMFCs can reduce efficiency due to the blocking of surface active sites. The whole anodic methanol oxidation reaction shuts down when there are no longer active sites for OH adsorption on the surface available, in other words, methanol oxidation on Pt only takes place in the presence of adsorbed OH with a proper coverage instead of surface oxides. The adsorbed OH is proved to be involved in more than one step [20, 110, 145, 168], and the reaction rate is also dependent on the OH

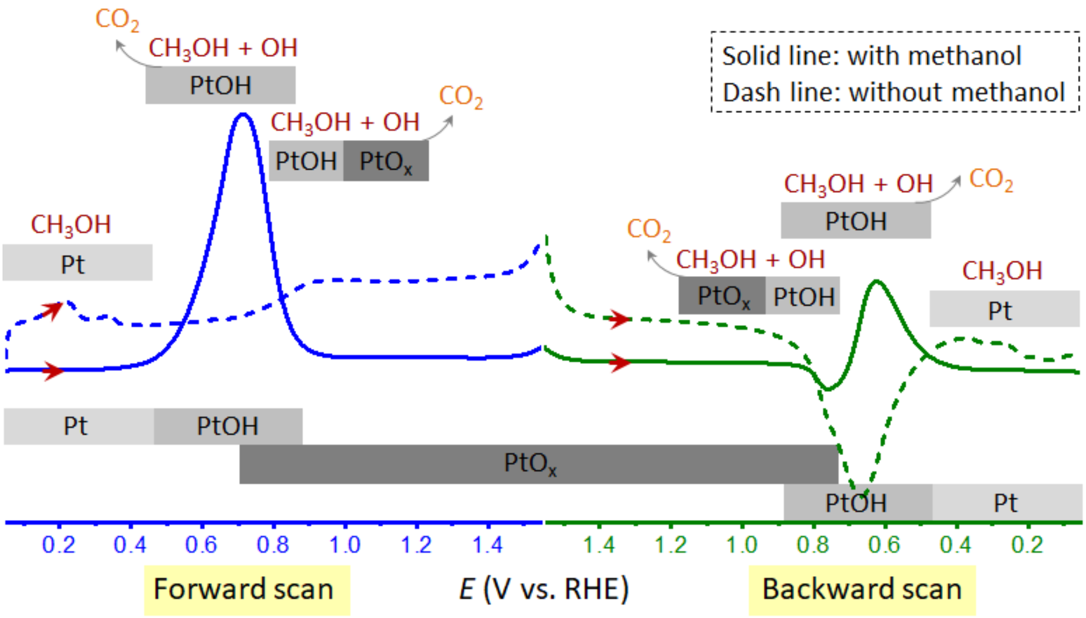

Figure 5.1: Cyclic voltammogram of MOR on Pt with detailed surface step features illustrating the reaction mechanism. The CV data are adopted from Figure 4.8, showcase the MOR process on Pt, highlighting the role of surface step features. Each CV is presented with independent current scales for clarity.

concentration, especially in dilute electrolyte [156, 167]. The MOR process is strongly related to the surface oxidation state of Pt in both forward and backward scan [158, 169]. Effective MOR requires a delicate balance where surface oxides are present to assist in intermediate oxidation but not so extensive as to inhibit the overall reaction by blocking active sites.

5.1.2 Methanol oxidation process during cathodic scan

The cathodic methanol oxidation peak is investigated by the methods of increasing the anodic and cathodic scan limits and reversed sweep directions. As the cathodic oxidation peak always seems to be smaller and distorted in most cases than anodic oxidation peaks, there are some arguments about the origin of this cathodic methanol oxidation peak: whether it is from methanol readsorption from electrolyte or some methanol intermediates continue to oxidize, such as CO, which are formed and remain on the surface during the anodic scans.

First, from Figure 4.12, CV scan starts from two vertex potentials then sweep positively and negatively. These two CV profile are precisely overlapping in both scan direactions, which reveals that the cathodic methanol oxidation peak is not related to the methanol intermediates that were formed during the previous forward scan. In other words, the source of this methanol oxidation current comes from the adsorption of methanol from electrolyte and is independent from the previous scans. This result is in agreement with the work from other groups [158, 170].

Then, from Figure 4.11, the cathodic oxidation peaks were influenced significantly by increasing the anodic scan limits. Increasing anodic scan potential leads to higher coverage of surface oxides on Pt surface. Consequently, during the backwards scans, more negative potentials are required to reduce the surface oxides, thus resulting in a less positive onset reduction potentials of cathodic oxidation current peaks. As discussed before, the second methanol oxidation peak primarily depends on the available active surface spots after removal of the surface oxide species. With decreasing potential, although more free sites become available, there is also less PtOH available to facilitate methanol oxidation. This results in a decrease in the methanol oxidation current peak value. Again, the adsorbed hydrogen species act as spectators without interfering with the cathodic MOR, as all currents reach zero at the same potential.

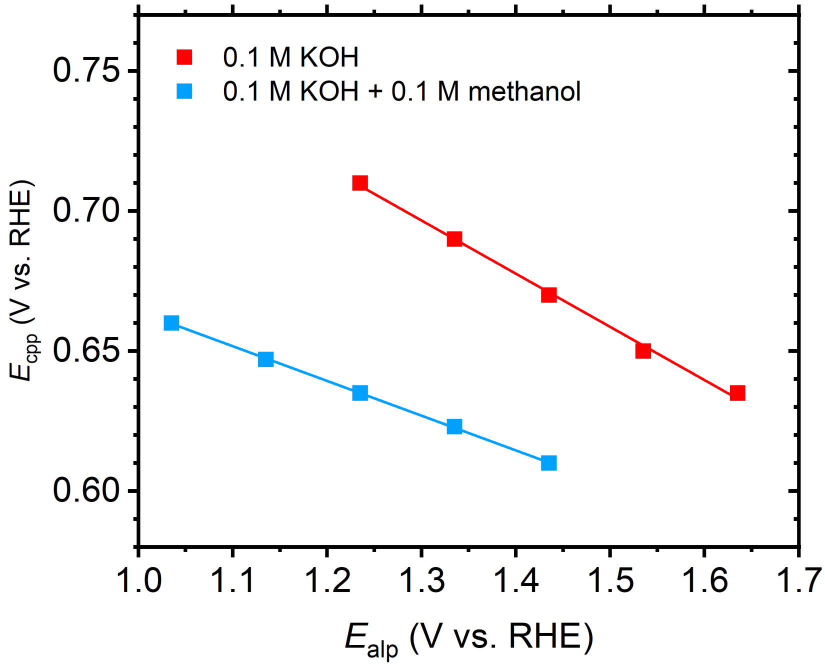

Figure 5.2: Plots of the cathodic peak potential (E_{cpp}) versus the anodic scan limited potential (E_{alp}) in 0.1 M KOH and 0.1 M KOH + 0.1 M methanol with the same experimental conditions as described in Figure 5.2 and Figure 4.11.

The potentials of cathodic peaks in both 0.1 M KOH and 0.1 M KOH + 0.1 M methanol electrolytes are plotted versus the potentials of anodic scan vertex as shown in Figure 5.2. The comparison of the plots in Figure 5.2 highlights the difference in behavior between oxygen reduction in two electrolytes. The smaller slope for the methanol-containing solution suggests that the anodic limit potential (E_{alp}) is not the primary factor governing the shift in cathodic peak potential (E_{cpp}) in this case. Instead, poisoning intermediates formed during methanol oxidation likely adsorb on the electrode surface, blocking active sites and limiting the cathodic peak shift. This behavior suggests that while the anodic limit potential influences oxygen reduction in the supporting electrolyte, the presence of methanol introduces additional surface interactions that dominate the potential shift.

5.1.3 Methanol concentration effect

Investigating methanol oxidation with different methanol concentrations provides valuable insights into the fundamental kinetics of the electrochemical process and the underlying reaction mechanisms. The rate of methanol oxidation is known to vary with methanol concentration [156, 167], and this variation can significantly impact the performance of electrochemical systems. At low methanol concentrations, the MOR is often limited by the availability of methanol molecules on the catalyst surface, while at high methanol concentrations, the MOR can be limited by the rate of methanol oxidation, the accumulation of reaction intermediates and Pt oxides on the catalyst surface.

Experimental studies have shown that the MOR on Pt catalysts exhibits a volcano-shaped dependence on the methanol concentration [108, 156], with an optimal methanol concentration for the maximum reaction rate. At low methanol concentrations, the reaction rate increases with increasing methanol concentration, as more methanol molecules are available for reaction on the

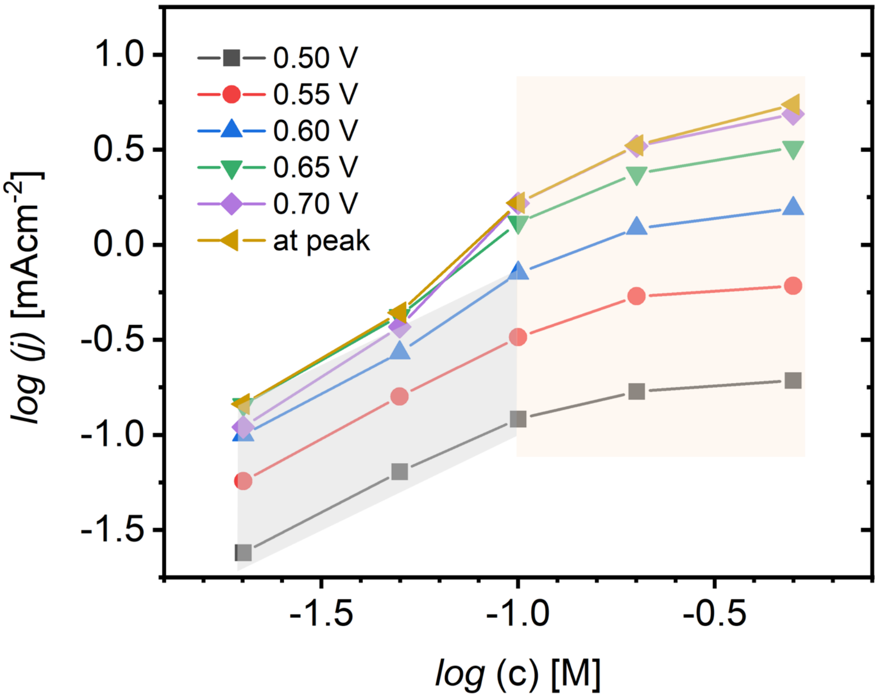

Figure 5.3: Plots of log j versus log of methanol concentration for anodic peak currents at different given potentials.

Pt surface. However, at high methanol concentrations above the optimal range, the reaction rate starts to decrease due to the accumulation of reaction intermediates on the Pt surface such as the formation of CO and CO_2 by-products.

Figure 5.3 shows the plots of logarithm of current density at a given potential versus the logarithm of different methanol concentrations. When the concentration is below 0.1 M, (with the ratio of methanol to KOH being less than 1, the gray area in Figure 5.3), a linear increase in current density with methanol concentration is observed. In this region, the reaction is potential-independent before reaching the potential of the current peak, which also indicates that the reactivity is free from transportation limitations. However, when the methanol concentration exceeds 1 M (the light orange area in Figure 5.3), the increase in current density slows and tends toward saturation. This behavior can be attributed to the partial poisoning of the Pt surface by adsorbed oxygen species. These adsorbed species decrease the reactivity by blocking active sites, thereby limiting the further increase in current despite higher methanol concentrations.

As methanol concentration increases, the methanol oxidation peaks exhibit higher magnitudes while remaining around the same peak potentials. Active methanol intermediates are known to be more sensitive to concentration than electrode potential. With a higher concentration of methanol in the electrolyte, increased reaction current at a certain potential is attributed to a higher coverage of methanol intermediates, suggesting that the rate-determining steps are the dehydrogenation of methanol and the adsorption of methanol intermediates, particularly at lower methanol concentrations.

Many research work suggested that when the electrolyte containing higher concentration of methanol, the reaction mechanism is no longer the same as in the lower concentration (ratio of methanol to KOH is below 1), moreover, an optimal ratio (around 1:1) of adsorbed methanol to hydroxyl was proposed, at which the reaction rate reaches maximum [21, 108, 156, 167]. In cases with higher methanol concentrations, oxides formation is the only reaction to shut down MOR. However in lower methanol concentration electrolyte, the reaction turned down before the onset of considerable amount of oxides formation, suggesting that lack of enough methanol mass transfer is the RDS.

With increasing c_{meth} in the same pH base solution, the ratio between adsorbed methanol and hydroxyl ion increases, which has an influence on the coverage of both methanol intermediates and oxides, thus impacting the overall reaction rate [156, 167]. With a surplus of methanol in the electrolyte, an increased amount of adsorbed hydroxyl is needed for methanol oxidation. This causes the reaction peaks to shift towards more positive potentials, as shown in Figure 4.19a, facilitating interaction with more adsorbed hydroxyl, as hydroxyl adsorption is a potential-dependent process. However, at higher potential range, the surface adsorbed hydroxyls turn into oxides, which block the surface thus decrease the reactivity of methanol oxidation, then the whole reaction shuts down.

5.2 Dual role of oxygen in MOR on Pt in alkaline electrolyte

Oxygen species on the Pt surface exhibit a dual role as both promoters and inhibitors of electrochemical reactions. Pt oxidation is an important process occurring on Pt electrode surface and has a strong impact on the Pt performance in terms of electrochemical catalytic reactivity. At lower potentials, the adsorbed hydroxide ions on Pt (PtOH) can increase the MOR activity and selectivity by promoting the formation of active intermediates, such as methoxyl (CH_3O) and formate ($HCOO^-$). However, at higher potentials, it can also act as inhibitors, blocking active spots and consequently reducing electrode surface area, thereby decreasing catalytic activity.

So far, it is generally believed that the onset potential of OH adsorption on Pt electrode is above $E = 0.5$ [171]-0.55 [168] V (vs. reversible hydrogen electrode). On Pt(111) in alkaline environment, the adsorption of OH happens from a lower potential. From our CV result of Figure 5.4a, which clearly shows that significant oxidation current already can be recorded before OH adsorption peak around $E = 0.55\,\mathrm{V}$. And the oxidation current reaches to peak at around $E = 0.65\,\mathrm{V}$, where the surface is only partially covered by adsorbed OH. Also, from the surface stress variation results, which showed a maximum value at around $E = 0.4\,\mathrm{V}$, from this potential, the surface stress state changed from H adsorption induced tensile stress into OH adsorption caused compressive surface stress. All these experimental results show that the OH adsorption facilitates the oxidation process and resulting in increasing the current at lower potentials in alkaline electrolyte.

In order to determine if the OH adsorption or desorption is affected by methanol adsorption or oxidation, another CV profile was obtained by subtracting the CV of 0.1 M KOH supporting electrolyte from the one of 0.1 M KOH + 0.02 M methanol electrolyte as shown in Figure 5.4b. The overall shape of CV has all the typical MOR features as in larger methanol concentration electrolyte (such as the CV of 0.05 M methanol present in Figure 4.9), especially the same onset potentials of both anodic and cathodic oxidation peaks as well as an intact cathodic MOR current peak with hysteresis. This demonstrates that the OH adsorption and desorption processes are not interfered by the existence of methanol molecule or related intermediates in electrolyte.

5.3 Adsorption and surface stress coupling on electrode surface

5.3.1 Pt surface stress variation in KOH

The surface evolution on Pt surface in 0.1 M KOH is firstly discussed to establish a baseline for understanding surface oxidation and reduction-induced surface stress changes without involving methanol adsorption and oxidation. Surface stress variations were measured during electrode potential cycling, with the cathodic vertex serving as the starting point. The positive change in surface stress variation is usually taken as tensile stress, namely a positive slope of Δf, and negative value of this variation means a compressive surface stress ($\Delta f < 0$).

The initial electrode process–the adsoprtion and desorption in HUPD region–is reversible and accompanied by an increase in f, that reflects the well-established positive value of the

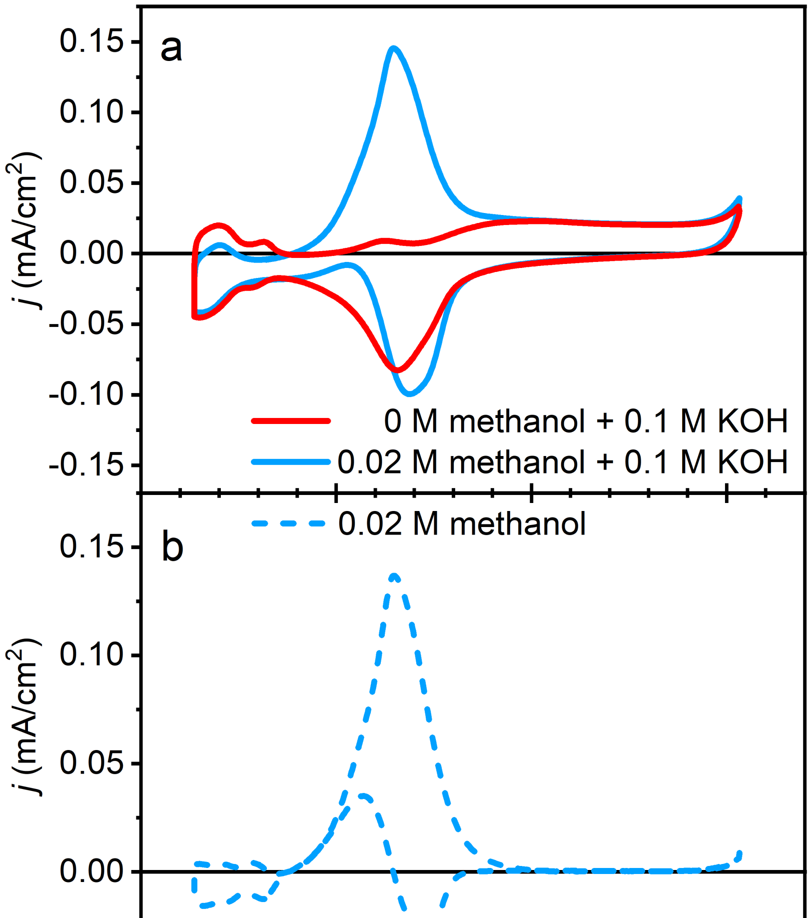

Figure 5.4: Cyclic voltammogram profile of Pt electrode a) in 0.1 M KOH, and 0.1 M KOH + 0.02 M methanol. b) subtraction of CV profiles in a). Scan rate: 20 mV/s

electrocapillary coupling parameter for hydrogen electrosorption on Pt [165, 172–175].

In the electrical double layer region, the surface stress reaches maximum [164] and does not change significantly in the vicinity of the peak potential (between $E = 0.3 - 0.4\,\mathrm{V}$), especially in the anodic scan direction.

In contrast to hydrogen region, the surface oxidation and reduction by OH species cause a more significant and irreversible compressive stress on electrode surface. The hysteresis of Δf is caused by the surface oxide formation during anodic scan and incomplete reduction during cathodic scan. Also, the potential of the Δf maximum during cathodic scan is a bit shifted to cathodic direction than that during anodic scan, which is consistent with the finding of other research work [164, 176], providing one more hint to the fact that oxidation and reduction of OH is an irreversible process on Pt electrode surface. Also, the desorption of Pt is completed even though there is hysteresis, as the surface stress value return to the same as initial value, namely there is no noticeable building up Pt oxides during the cyclic scanning.

5.3.2 Adsorption of methanol and methanol intermediates

The sorption-strain coupling for methanol

Now it is discussed the situation when there is methanol with different concentrations added to the base electrolyte. Methanol oxidation can be influenced by HUPD due to the competitive adsorption between hydrogen and methanol. Actually, it has been indicated that the initial methanol adsorption is rather dependent on hydrogen coverage, which can be influenced by methanol concentration, than potential. This is also observed in our CV results (Figure 4.9), where a smaller UPD current is observed due to the presence of methanol in the electrolyte. Even when there is a saturation coverage of hydrogen on Pt electrode, methanol still can be placed on top of the hydrogen layer [177]. Methanol adsorbs on the electrode even when the surface is fully covered with hydrogen at lower potentials, the weaker interaction between methanol and adsorbed hydrogen keeps the methanol molecules at a distance (approximately 1 Å) from the surface, preventing them from participating in initial methanol oxidation. DFT results also suggest that the methanol adsorption on Pt(111) is rather weak, which is indicated by the long PtO bonding distance (2.43 Å [178] - 2.59 Å [179]). As a consequence, the reaction can only start when the surface coverage of hydrogen is low enough. This also explained the same stress variation caused by adsorption of H at the beginning, before $E = 0.2\,\mathrm{V}$ in lower methanol containing electrolyte. As the methanol concentration increases, methanol adsorption begins at $E = 0.2\,\mathrm{V}$, creating a plateau due to the weak interaction between methanol and the Pt surface.

The stress variation data suggests that the sorption-strain coupling parameter ζ for methanol on Pt is small. For a quantification of ζ, we note that Figure 5.5 suggests f to vary by $|\Delta f| \lesssim 0.1\,\mathrm{N/m}$ when methanol adsorbs. The specific excess in methanol may be estimated based on experiments in vacuum, which suggest a saturation coverage of 0.5 methanol per surface platinum atoms on a dense-packed Pt surface [180], hence $\Gamma_{\mathrm{MeOH}} \approx 7.5\,\mathrm{nm}^{-2}$. With Equation 2.40 and 2.45, this suggests $|\zeta| \lesssim 0.08\,\mathrm{eV}$. For comparison, the same figure gives $\Delta f = -2.6\,\mathrm{N/m}$ for oxygen species adsorption, and with one oxygen per platinum in a dense packed monolayer we have $\Gamma_{\mathrm{O}} = 15.0\,\mathrm{nm}^{-2}$. Hence, $\zeta = -1.1\,\mathrm{eV}$ for oxygen electrosorption on platinum, which is substantially larger than for methanol adsorption.

Methanol intermediates adsorption

The intermediates formed during the methanol conversion process can adsorb on the Pt catalyst surface and affect the reaction rate and selectivity. The discussion of the surface methanol dehydrogenation intermediates are divided into CO and non-CO adsorbates, such as extensively studied formaldehyde and product of it, formate, which can adsorb on Pt surfaces through their carbonyl groups and are believed to occur through a combination of physisorption and chemisorption mechanisms. The physisorption is due to weak Van der Waals forces between the

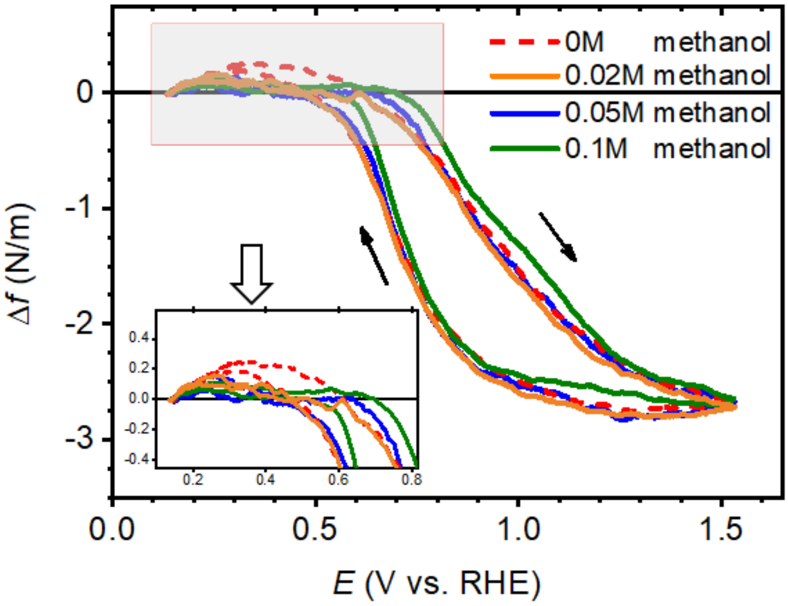

Figure 5.5: Results of *in situ* cantilever bending experiment on a Pt electrode in the electrolyte with different concentration of methanol from 0 M to 0.1 M, as indicated in legend.

formaldehyde molecule and the Pt surface, while the chemisorption is a result of the formation of a covalent bond between the carbonyl group and the Pt surface.

The first step of the oxidation of methanol is the reaction between absorbed methanol and adsorbed oxygen [20, 110]. It has been shown that an essentially saturated methanol adsorbate layer on Pt forms immediately once the HUPD layer is lifted [129, 142]. The alkaline solutions of our experiment contain methoxy (MeO^-), which may be expected to contribute to the adsorption process. Remarkably, these adsorption processes leave no signature in the $f(E)$ graph of our experiments. Such weak adsorption of methanol intermediates was also indicated from rotating disk electrode experiment, that with increasing rotating rate, the reaction current is actually decreasing [156].

CO adsorption in alkaline electrolyte

As previously mentioned, CO is the most important intermediate during methanol oxidation process and it has been long considered as the primary cause of poisoning the surface activity [20, 110]. Once CO forms and adsorbs onto the electrode surface, it occupies and blocks active sites, preventing the adsorption and reaction of other reactants or intermediates that could otherwise potentially be further oxidized.

The adsorption of CO is a displacive reaction and the kinetics of this adsorption process have been shown to be relatively slow [181–183]. The CO oxidation reaction can also help to remove the adsorbed CO species from the Pt surface, restoring the activity of the active sites for methanol oxidation. And the kinetic process of CO oxidation is much faster than CO adsorption, which means if the coverage of CO is sufficient to poison the surface, it has to leave trace on the surface stress. And it is worth to note that the behavior of CO adsorption on Pt surface gives rise to a compressive (negative) surface stress [175, 181, 182], which is similar to OH adsorption. In other words, the oxidation of CO (CO desorption process) on Pt induces tensile strain on the surface, countering the compressive stress from OH adsorption. Thus, the observation of a plateau in surface stress indicates the absence of significant CO accumulation. This implies that CO oxidation is continuously occurring, preventing CO build-up and maintaining the stress plateau. If CO oxidation were not happening, the surface stress would be predominantly compressive due to the accumulation of both CO and OH.

Also, either existence of CO or OH adsorption can give rise to a compressive surface stress, the plateau rules out poisoning effect from both molecules during the main methanol oxidation potential range. Namely, under such positive potential, the CO is oxidized into CO_2 and promptly leaves the surface. This conclusion is likely specific to methanol oxidation in alkaline solution, where OH^- adsorption occurs at a relatively low potential, facilitating the oxidation of CO and preventing its accumulation for causing significant coverage with poisoning effect.

5.3.3 Sorption-strain coupling of oxide species

The surface process of oxide formation and reduction clearly plays an important role in the methanol oxidation reaction as much research has been investigated on this topic for years. The surface oxides can affect both the onset of CO oxidation and the hysteresis of second methanol oxidation peak found during the cathodic scan sweep of cyclic voltammograms. With an increase of the oxide coverage, the role it plays can change from a reactant into a hindrance. The coverage of surface oxides is related to the electrode potential, methanol concentration, pH and the reaction intermediates as well.

During the anodic sweep scan, the sharp decreasing of methanol oxidation current is from the metal oxide formation poisoning. A higher concentration of methanol can remove more PtOH to form reaction intermediates, as shown in Figure 4.19a, where the current ceases at a higher potential with increased methanol concentration. These intermediates may also react with PtO [169], thereby delaying Pt oxide formation. And in cathodic sweep process, it can be observed from cyclic voltammograms that the reduction of oxide is overlapped with second methanol oxidation (cathodic methanol oxidation) peak as discussed previously. And with higher concentration of methanol, the oxidation occurred more positive accordingly. This is due to the less extent of surface oxide coverage during anodic oxidation process and thus reduction of oxide within higher concentration of methanol started early. In other words, once this poisoning product started to be reduced, the surface can regain active sites to conduct methanol oxidation again.

Oxygen alone cannot be the poisoning agent. The surface stress data also shed light on the role of oxygen as a possible poisoning agent for the reaction. That role is suggested specifically for methanol oxidation in alkaline media [110]. In our data, the discontinuous drop in the reactivity coincides with a discontinuous variation that brings f down to precisely the value of the oxygen-species-covered surface of platinum in the supporting electrolyte at the respective potential. For electrolytes that are dilute in methanol, the surface stress value at that point implies that the surface is only partly covered with oxygen. As the reactivity is completely shut off while the oxygen coverage is incomplete, oxygen alone cannot be the poisoning agent. The above argument is further supported by inspecting the cathodic scan. Here, the surface stress suggests that a major fraction of the adsorbed oxygen species has already desorbed at the time when the reactivity comes back on.

The surface stress data further confirms that the surface is fully covered with oxygen at the anodic vertex of the CV and during the initial millivolts of the cathodic scan. Under these conditions, the MOR current is negligible, indicating that the fully oxygen-covered surface is inactive.

The surface stress measures the oxygen coverage. Contrary to methanol adsorption, the electrosorption of oxygen species has a strong coupling to the strain, with negative-valued ς and ζ [165, 172, 173, 184]. This is clearly born out by f continuously becoming more negative as oxygen adsorbs from the supporting electrolyte. The overall magnitude of the surface stress change during oxygen electrosportion and the hysteresis in our data are both consistent with previous experiments [184–186].

Remarkably, our surface stress values in all electrolytes agree sensibly at the positive vertex. This suggests that the surface coverage, θ_{ox}, with oxygen species is identical there. The consistency in the f data implies that the surface stress may be taken as a direct measure for θ_{ox}.

Especially upon the reduction process, the surface stress at the cathodic vertex return to the initial value, indicating that the surface is reduced to the original state even with hysteresis.

The oxygen coverage remains negligible while the reaction is on. The electrolytes with methanol have a constant f throughout the potential range of high methanol oxidation rate. This suggests that θ_{ox} remains very small throughout the state of high reactivity. This observation is consistent with the notion that adsorbed oxygen is immediately consumed by the reaction. In fact, our *in situ* surface stress data presents a particularly direct and compelling evidence for that fact. In other words, the extend of coverage of adsorbed OH is the RDS during main MOR process.

5.4 Elastic strain effect on MOR reactivity

5.4.1 External strain effect on the reactivity at low potentials

From the previous discussion on the adsorption processes of different adsorbates on Pt surface via cantilever bending experiment, the methanol adsorption does not induce a significant surface stress variation especially comparing to OH adsorption. Thus, such weak coupling indicates that, in return, the methanol coverage is also indifferent towards the external strain modulation. Upon the tensile strain, calculations [71] and experiments [71, 75] have shown that the energy required to adsorb hydrogen atoms decreases (i.e., binding becomes stronger) on Pt(111) surface. However, as discussed before in the MOR mechanism section, even though the competitive adsorption effect between hydrogen and methanol molecules, the available free spots on Pt surface in alkaline electrolyte for methanol is superfluous. Namely, there are enough methanol species available to be oxidized and it can be excluded as the RDS at the initial stage.

Now we simplify the step reactions of MOR process for a better discussion of the external strain effect. Based on previous discussion, the main processes of MOR can be considered to happen through two groups of intermediates, as CO and non-CO intermediates (noted as Methanol' in the following reaction equations), and their further oxidation by adsorbed OH.

$$\mathrm{CH_3OH + n\,OH^- \longrightarrow M' + ne^-} \tag{5.1}$$

$$\mathrm{CH_3OH + 4\,OH^- \longrightarrow CO + 4\,e^-}, \tag{5.2}$$

Tensile strain increases the adsorption enthalpy of OH adsorption and oxidation over the whole potential range [187]. This is compatible with the notion that tensile strain makes the surface more binding for oxygen, in other words, $\zeta < 0$ for oxysorption. That notion is supported by DFT [188] and by the observations on the surface stress along with Equation 2.45. Initially, an increased OH adsorption can accelerate the reaction by facilitating methanol oxidation into adsorbed intermediates, particularly CO (Equations 5.1 and 5.2), at lower potentials. Since the strain effect on the adsorption enthalpy of methanol and M' is relatively small, the observed rise in reaction current mainly results from strain-induced higher OH coverage. In contrast, non-CO intermediates, which exhibit weaker adsorption compared to CO, are more likely to desorb into the electrolyte as soluble products. This dual effect of tensile strain—enhancing both CO and OH adsorption—facilitates surface reactions while simultaneously promoting the desorption of less strongly adsorbed species. However, during the main reaction process, competitive adsorption between CO and non-CO intermediates limits the actual reaction activity enhancement caused by tensile strain.

This process is illustrated as Figure 5.6, the step processes, where the removal of different intermediates are influenced directly by the OH adsorption process, which can be modulated by the applied tensile strain. Specifically, tensile strain tends to enhance the binding of CO despite concurrently promoting stronger OH adsorption. The differential adsorption behavior under strain conditions plays a critical role in determining the surface reactivity and stability. Furthermore, non-CO intermediates exhibit a relatively indifferent response to tensile strain.

However, these intermediates tend to undergo oxidation more readily due to the enhanced OH adsorption facilitated by tensile strain. This leads to a complex interplay where tensile strain not only strengthens CO binding but also accelerates the oxidation of other intermediates by augmenting OH adsorption.

5.4.2 External strain effect on the reactivity at high potentials

At higher potentials, the stronger binding forces and increased oxide coverage can inhibit the reaction. The stronger interaction between the Pt surface and oxygen species (such as OH) competes with the adsorption of methanol and its intermediates. This counter adsorption effect leads to a blocking phenomenon, where the active sites are less available for the methanol oxidation reaction, reducing the overall reactivity at higher potentials.

From the stress variation results (Figure 4.18 and Figure 4.19), which are showing a platform during MOR, indicating that as soon as the OH adsorption starts, they are consumed immediately, namely the OH adsorption is the RDS in this case. However, an enhanced binding with OH (from external tensile strain modulation) does not bring a higher reaction activity, as the value is negative in the higher potential range with partially oxidized surface. Throughout the regime of high reactivity, the value of $\hat{j}_{\mathrm{re}}$ is negative, in other words, the reactivity is enhanced by compressive strain. This observation provides a direct confirmation that the enhanced reactivity of core-shell nanoparticles with compressed platinum surface layers [189] is indeed consistent with a strain effect, and may be understood independent of the ligament effects that contribute simultaneously in those catalysts.

As mentioned above, the MOR is believed to be essentially reaction-limited even when–as in our DECMA setup–no rotating disk electrode is used [156, 190–192]. The low sensitivity of all CVs on scan rate and cell geometry is at least consistent with that notion. That suggests that the DECMA result for $\hat{j}_{\mathrm{re}}$ represents an inherent strain dependence of the reaction, essentially independent of transport limitations. The largest relative change in current is around the peaks of j and $\hat{j}_{\mathrm{re}}$, where the data of Fig 4.21 suggest $\mathrm{d}\ln j/\mathrm{d}e = \hat{j}_{\mathrm{re}}/j \approx -4$. In other words, an elastic area strain of -10% – corresponding roughly to a lattice parameter decrease by 3%, which may be taken as a realistic upper limit based on existing core shell catalyst designs – enhances the reactivity by roughly 40%.

The transition between $\hat{j}_{\mathrm{re}} > 0$ at the onset of the MOR and $\hat{j}_{\mathrm{re}} < 0$ at finite overpotential suggests an distinct change in the dual role of oxygen, where oxygen transitions from acting as a reaction promoter to an inhibitor. Apparently, the availability of oxygen is no longer rate-limiting at high overpotential. The current-strain coupling will then be controlled by the strain-sensitivity of a reaction barrier height and/or the adsorption enthalpy of another species. In view of the complexity of the reaction mechanism, the nature of this barrier or species cannot be resolved by this experiment. However, the continuous variation of both the reaction current and the current-strain coupling during the CV implies that up until the discontinuous drop in reactivity, a single process may remain rate-limiting, regardless of the overpotential.

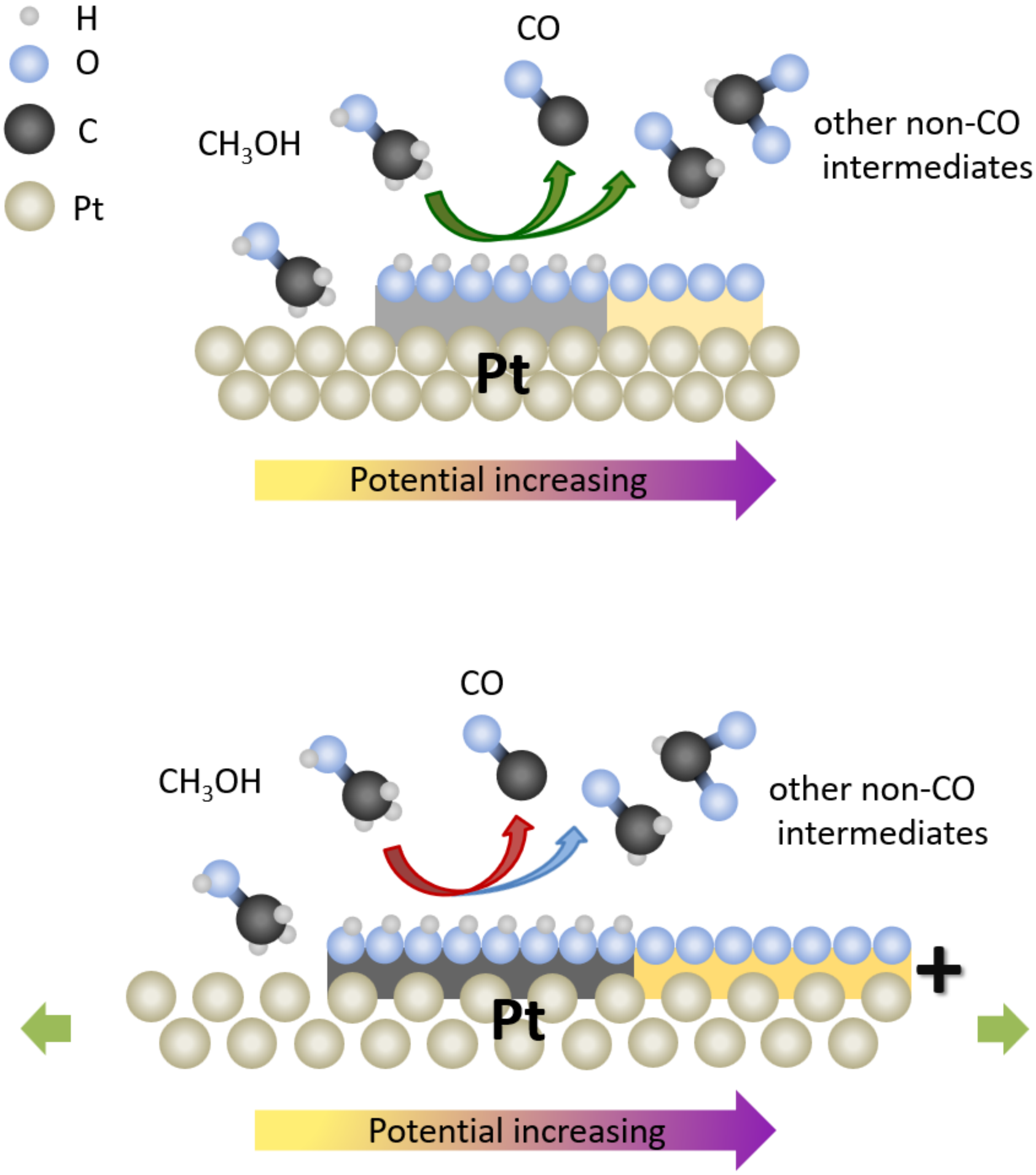

Figure 5.6: Schematic illustration of the MOR mechanism on Pt with and without external tensile strain effect. With tensile strain, the surface tends to have stronger binding and higher coverage of PtOH as well as Pt oxides, this can boost the CO oxidation at lower potential, but inhibit the reaction reactivity at higher potential due to the competitive adsorption effect against methanol intermediates and oxides formation with blocking effect.

Chapter 6

Summary and outlook

6.1 Summary

This thesis elaborates on and discusses the effect of external strain on Pt electrodes during the methanol oxidation reaction. Building on prior studies of electrocapillary coupling conducted by our group, which developed a quantitative method to determine electrocapillary coupling parameters using a custom-designed setup called Dynamic-Electrochemical-Mechanical Analysis (DECMA), this work extends the analysis by quantifying the reactivity-strain coupling coefficient as the current-strain coupling coefficient. The study establishes a direct relationship between external strain and reaction current during methanol oxidation reaction without looking into multiple sub steps and various intermediates. Additionally, adsorption-induced surface stress variations during MOR were measured using a cantilever bending setup. The cyclic voltammetry (CV) behavior of MOR was revisited in detail to improve understanding of this complex multi-step mechanism.

The combination of CVs and cantilever bending experiments offers a comprehensive analysis of methanol oxidation on Pt electrodes. It confirms that OH adsorption facilitates MOR in the early stages. However, when the surface becomes fully covered by Pt oxides, its activity declines, inhibiting further methanol oxidation. The second methanol oxidation peak observed during the cathodic scan correlates with the availability of free Pt surface sites and is irrelevant to the poisonous intermediate CO which is formed during the first methanol oxidation process in the anodic scan direction.

Surface stress variation was measured in situ during cyclic voltammetry. In the base electrolyte (0.1 M KOH), the sorption-strain coupling parameter ζ stays positive during HUPD region and turned into negative in oxidation region, which stays consistent with established research. This behavior implies that tensile strain enhances oxygen binding on the Pt surface and increases surface oxygen coverage at a constant electrode potential.

In methanol-containing electrolytes, surface stress measurements during different reaction stages suggest that methanol adsorption enthalpy is not strain-dependent, as surface stress remains relatively constant throughout the whole dehydrogenation process of methanol. The surface stress drops dramatically back to original surface state whenever the reaction is off. The surface stress results also exclude the CO poisoning, as no characteristic trace of CO adsorption of Pt surface was indicated from the surface stress measurement. In alkaline environment, especially when the surface is under tensile strain, which has a positive effect on adsorption strength of PtOH, the CO is unlikely to form a considerable poisoning coverage to occupy and block the Pt surface.

Current-strain coupling measurements from DECMA reveal a strong peak during methanol oxidation, independent of strain frequency. The dominance of the real part of the strain-modulated current indicates a significant effect on the Faradaic current, rather than the capacitive current, caused by external tensile strain. The decline in reaction current at higher overpotentials under tensile strain is attributed to the stronger bonding between Pt and surface oxides, inhibiting further oxidation activity.

6.2 Outlook

Strain effect on Au during oxygen reduction reaction (ORR)

On Au electrode surface, the situation is different and more complicated from Pt. Figure 6.1 shows the CVs and current-strain coupling coefficient of ORR on Au electrode. During the oxidation process, both $\hat{\jmath}$ are positive. This is well known for the tensile strain reinforced OH adsorption. During the first reduction of the Au oxides in backwards scan, $\hat{\jmath}$ shows similar positive value as the oxidation peak, right after that, $\hat{\jmath}$ continues to decrease and changed sign to negative during the ORR process. This is a clear difference from the oxides reduction peak, and also opposite tendency from Pt electrode towards tensile strain (Figure 4.20), in other words, tensile strain increase the gold oxides reduction current, but decrease the oxygen reduction current.

A hybrid strain effect on overall electrocatalytic reactivity has been observed from DECMA, which provides a direct evidence of different strain modulation mechanism on Pt and Au surface and opens new avenues for future research aimed at unlocking deeper mechanistic insights and advancing the design of more efficient electrocatalysts.

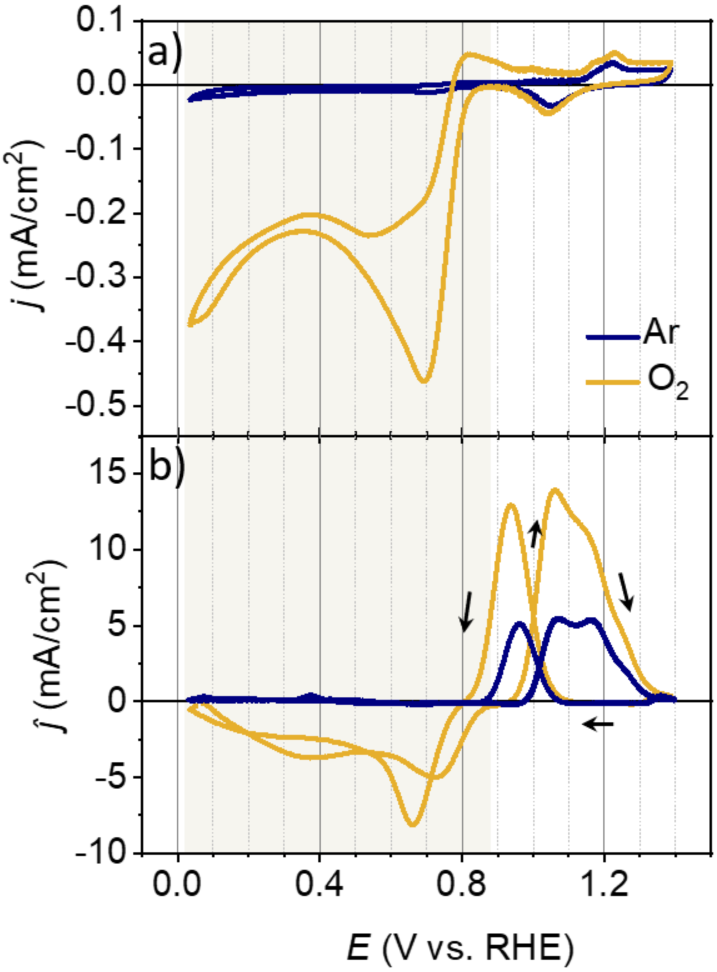

Figure 6.1: a) Cyclic voltammogram of Au electrode in 0.1 M KOH electrolyte in different atmosphere. The navy one is in Ar, and yellow one is in O_2. Scan rate is 20 mV/s. b) results of current-strain potential response which was *in situ* measured with CV. Arrows indicate the scan direction.

Bibliography

[1] Viktor Hacker and Shigenori Mitsushima. *Fuel cells and hydrogen: from fundamentals to applied research.* elsevier, 2018.

[2] William Robert Grove. Lvi. on a new voltaic combination: To the editors of the philosophical magazine and journal. *The London, Edinburgh, and Dublin Philosophical Magazine and Journal of Science*, 13(84):430–431, 1838.

[3] Supramaniam Srinivasan, EA Ticianelli, CR Derouin, and A Redondo. Advances in solid polymer electrolyte fuel cell technology with low-platinum-loading electrodes. *NASA-Lewis Research Center, Space Electrochemical Research and Technology (SERT)*, 1987.

[4] Omar Z Sharaf and Mehmet F Orhan. An overview of fuel cell technology: Fundamentals and applications. *Renewable and sustainable energy reviews*, 32:810–853, 2014.

[5] Klaus-Dieter Kreuer, Stephen J Paddison, Eckhard Spohr, and Michael Schuster. Transport in proton conductors for fuel-cell applications: simulations, elementary reactions, and phenomenology. *Chemical reviews*, 104(10):4637–4678, 2004.

[6] Steven J Hamrock and Michael A Yandrasits. Proton exchange membranes for fuel cell applications. *Journal of Macromolecular Science, Part C: Polymer Reviews*, 46(3):219–244, 2006.

[7] Yun Wang, Ken S Chen, Jeffrey Mishler, Sung Chan Cho, and Xavier Cordobes Adroher. A review of polymer electrolyte membrane fuel cells: Technology, applications, and needs on fundamental research. *Applied energy*, 88(4):981–1007, 2011.

[8] Yun Wang, Bongjin Seo, Bowen Wang, Nada Zamel, Kui Jiao, and Xavier Cordobes Adroher. Fundamentals, materials, and machine learning of polymer electrolyte membrane fuel cell technology. *Energy and AI*, 1:100014, 2020.

[9] Xiaoming Ren, Mahlon S Wilson, and Shimshon Gottesfeld. High performance direct methanol polymer electrolyte fuel cells. *Journal of the Electrochemical Society*, 143(1):L12, 1996.

[10] Chunwen Sun and Ulrich Stimming. Recent anode advances in solid oxide fuel cells. *Journal of Power Sources*, 171(2):247–260, 2007.

[11] R Mark Ormerod. Solid oxide fuel cells. *Chemical Society Reviews*, 32(1):17–28, 2003.

[12] A John Appleby. Fuel cell handbook. 1988.

[13] Saad Mekhilef, Rahman Saidur, and Azadeh Safari. Comparative study of different fuel cell technologies. *Renewable and Sustainable Energy Reviews*, 16(1):981–989, 2012.

[14] Siti Kartom Kamarudin, F Achmad, and Wan Ramli Wan Daud. Overview on the application of direct methanol fuel cell (dmfc) for portable electronic devices. *International Journal of hydrogen energy*, 34(16):6902–6916, 2009.

[15] Liyuan Gong, Zhiyuan Yang, Kui Li, Wei Xing, Changpeng Liu, and Junjie Ge. Recent development of methanol electrooxidation catalysts for direct methanol fuel cell. *Journal of energy chemistry*, 27(6):1618–1628, 2018.

[16] Claude Lamy, Alexandre Lima, Véronique LeRhun, Fabien Delime, Christophe Coutanceau, and Jean-Michel Léger. Recent advances in the development of direct alcohol fuel cells (dafc). *Journal of Power Sources*, 105(2):283–296, 2002.

[17] Norazlianie Sazali, Wan Norharyati Wan Salleh, Ahmad Shahir Jamaludin, and Mohd Nizar Mhd Razali. New perspectives on fuel cell technology: A brief review. *Membranes*, 10(5):99, 2020.

[18] Mike L Perry and Tom F Fuller. A historical perspective of fuel cell technology in the 20th century. *Journal of the electrochemical society*, 149(7):S59, 2002.

[19] Hansan Liu, Chaojie Song, Lei Zhang, Jiujun Zhang, Haijiang Wang, and David P Wilkinson. A review of anode catalysis in the direct methanol fuel cell. *Journal of Power Sources*, 155(2):95–110, 2006.

[20] Eileen Hao Yu, Keith Scott, and Robert W Reeve. A study of the anodic oxidation of methanol on pt in alkaline solutions. *Journal of Electroanalytical Chemistry*, 547(1):17–24, 2003.

[21] PS Kauranen, Eivind Skou, and J Munk. Kinetics of methanol oxidation on carbon-supported pt and pt+ ru catalysts. *Journal of Electroanalytical Chemistry*, 404(1):1–13, 1996.

[22] TS Zhao, Rong Chen, WW Yang, and Chao Xu. Small direct methanol fuel cells with passive supply of reactants. *Journal of Power Sources*, 191(2):185–202, 2009.

[23] Fusao Kitamura, Machiko Takahashi, and Masatoki Ito. Carbon monoxide adsorption on platinum (111) single-crystal electrode surface studied by infrared reflection-absorption spectroscopy. *Surface Science*, 223(3):493–508, 1989.

[24] S Gilman. A study of the mechanism of carbon monoxide adsorption on platinum by a new electrochemical procedure1. *The Journal of Physical Chemistry*, 67(1):78–84, 1963.

[25] RJ Behm, PA Thiel, PR Norton, and G Ertl. The interaction of co and pt (100). i. mechanism of adsorption and pt phase transition. *The Journal of Chemical Physics*, 78 (12):7437–7447, 1983.

[26] CW Olsen and RI Masel. An infrared study of co adsorption on pt (111). *Surface Science*, 201(3):444–460, 1988.

[27] K Wang, HA Gasteiger, NM Markovic, and PN Ross Jr. On the reaction pathway for methanol and carbon monoxide electrooxidation on pt-sn alloy versus pt-ru alloy surfaces. *Electrochimica Acta*, 41(16):2587–2593, 1996.

[28] S Gilman. The mechanism of electrochemical oxidation of carbon monoxide and methanol on platinum. ii. the "reactant-pair" mechanism for electrochemical oxidation of carbon monoxide and methanol1. *The Journal of Physical Chemistry*, 68(1):70–80, 1964.

[29] MW Breiter. Role of adsorbed species for the anodic methanol oxidation on platinum in acidic electrolytes. *Discussions of the Faraday Society*, 45:79–86, 1968.

[30] Charles K Westbrook and Frederick L Dryer. Comprehensive mechanism for methanol oxidation. *Combustion Science and Technology*, 20(3-4):125–140, 1979.

[31] E Herrero, W Chrzanowski, and A Wieckowski. Dual path mechanism in methanol electrooxidation on a platinum electrode. *The Journal of Physical Chemistry*, 99(25):10423–10424, 1995.

[32] Yuanhui Zuo, Wenchao Sheng, Wenquan Tao, and Zhuo Li. Direct methanol fuel cells system: A review of dual-role electrocatalysts for oxygen reduction and methanol oxidation. *Journal of Materials Science & Technology*, 2022.

[33] M. Mavrikakis, B. Hammer, and J. K. Norskov. Effect of strain on the reactivity of metal surfaces. *Physical Review Letters*, 81(13):2819–2822, 1998.

[34] E. E. Benson, M. A. Ha, B. A. Gregg, J. van de Lagemaat, N. R. Neale, and D. Svedruzic. Dynamic tuning of a thin film electrocatalyst by tensile strain. *Scientific Reports*, 9, 2019.

[35] Alireza Khorshidi, James Violet, Javad Hashemi, and Andrew A. Peterson. How strain can break the scaling relations of catalysis. *Nature Catalysis*, 2018.

[36] P. Strasser, S. Koh, T. Anniyev, J. Greeley, K. More, C. F. Yu, Z. C. Liu, S. Kaya, D. Nordlund, H. Ogasawara, M. F. Toney, and A. Nilsson. Lattice-strain control of the activity in dealloyed core-shell fuel cell catalysts. *Nature Chemistry*, 2(6):454–460, 2010.

[37] Andrei Ruban, Bjørk Hammer, Per Stoltze, Hans Lomholt Skriver, and Jens Kehlet Nørskov. Surface electronic structure and reactivity of transition and noble metals. *Journal of Molecular Catalysis A: Chemical*, 115(3):421–429, 1997.

[38] Sen Zhang, Xu Zhang, Guangming Jiang, Huiyuan Zhu, Shaojun Guo, Dong Su, Gang Lu, and Shouheng Sun. Tuning nanoparticle structure and surface strain for catalysis optimization. *Journal of the American Chemical Society*, 136(21):7734–7739, 2014.

[39] Hai-Jun Jin, Xiao-Lan Wang, Smrutiranjan Parida, Ke Wang, Masahiro Seo, and Jörg Weissmüller. Nanoporous au- pt alloys as large strain electrochemical actuators. *Nano letters*, 10(1):187–194, 2010.

[40] Qingying Jia, Wentao Liang, Michael K Bates, Prasanna Mani, Wendy Lee, and Sanjeev Mukerjee. Activity descriptor identification for oxygen reduction on platinum-based bimetallic nanoparticles: in situ observation of the linear composition–strain–activity relationship. *ACS nano*, 9(1):387–400, 2015.

[41] Masato Asano, Ryutaro Kawamura, Ren Sasakawa, Naoto Todoroki, and Toshimasa Wadayama. Oxygen reduction reaction activity for strain-controlled pt-based model alloy catalysts: surface strains and direct electronic effects induced by alloying elements. *Acs Catalysis*, 6(8):5285–5289, 2016.

[42] Yalin Xiong, Hao Shan, Zhengnan Zhou, Yucong Yan, Wenlong Chen, Yaxiong Yang, Yongfeng Liu, He Tian, Jianbo Wu, Hui Zhang, et al. Tuning surface structure and strain in pd-pt core-shell nanocrystals for enhanced electrocatalytic oxygen reduction. *Small*, 13 (7):1603423, 2017.

[43] A Schlapka, M Lischka, A Groß, U Käsberger, and P Jakob. Surface strain versus substrate interaction in heteroepitaxial metal layers: Pt on ru (0001). *Physical Review Letters*, 91 (1):016101, 2003.

[44] Minshu Du, Lishan Cui, Yi Cao, and Allen J Bard. Mechanoelectrochemical catalysis of the effect of elastic strain on a platinum nanofilm for the orr exerted by a shape memory alloy substrate. *Journal of the American Chemical Society*, 137(23):7397–7403, 2015.

[45] Alireza Khorshidi, James Violet, Javad Hashemi, and Andrew A Peterson. How strain can break the scaling relations of catalysis. *Nature Catalysis*, 1(4):263–268, 2018.

[46] Binghong Han, Christopher E Carlton, Anusorn Kongkanand, Ratandeep S Kukreja, Brian R Theobald, Lin Gan, Rachel O'Malley, Peter Strasser, Frederick T Wagner, and Yang Shao-Horn. Record activity and stability of dealloyed bimetallic catalysts for proton exchange membrane fuel cells. *Energy & Environmental Science*, 8(1):258–266, 2015.

[47] Peter Strasser, Shirlaine Koh, Toyli Anniyev, Jeff Greeley, Karren More, Chengfei Yu, Zengcai Liu, Sarp Kaya, Dennis Nordlund, Hirohito Ogasawara, et al. Lattice-strain control of the activity in dealloyed core–shell fuel cell catalysts. *Nature chemistry*, 2(6):454–460, 2010.

[48] Debangshu Mukherjee, Jocelyn TL Gamler, Sara E Skrabalak, and Raymond R Unocic. Lattice strain measurement of core@ shell electrocatalysts with 4d scanning transmission electron microscopy nanobeam electron diffraction. *ACS Catalysis*, 10(10):5529–5541, 2020.

[49] Lin Cao, Frieder Scheiba, Christina Roth, Franz Schweiger, Carsten Cremers, Ulrich Stimming, Hartmut Fuess, Liquan Chen, Wentao Zhu, and Xinping Qiu. Novel nanocomposite Pt/RuO$_x$ h2o/carbon nanotube catalysts for direct methanol fuel cells. *Angewandte Chemie*, 118(32):5441–5445, 2006.

[50] Yuehe Lin, Xiaoli Cui, Clive H Yen, and Chien M Wai. Ptru/carbon nanotube nanocomposite synthesized in supercritical fluid: a novel electrocatalyst for direct methanol fuel cells. *Langmuir*, 21(24):11474–11479, 2005.

[51] Yijin Kang, Jun Beom Pyo, Xingchen Ye, Thomas R Gordon, and Christopher B Murray. Synthesis, shape control, and methanol electro-oxidation properties of pt–zn alloy and pt3zn intermetallic nanocrystals. *Acs Nano*, 6(6):5642–5647, 2012.

[52] Yang Fan, Pei-Fang Liu, Zong-Wen Zhang, Ying Cui, and Yan Zhang. Three-dimensional hierarchical porous platinum–copper alloy networks with enhanced catalytic activity towards methanol and ethanol electro-oxidation. *Journal of Power Sources*, 296:282–289, 2015.

[53] Cuiling Li, Victor Malgras, Saad M Alshehri, Jung Ho Kim, and Yusuke Yamauchi. Electrochemical synthesis of mesoporous pt nanowires with highly electrocatalytic activity toward methanol oxidation reaction. *Electrochimica Acta*, 183:107–111, 2015.

[54] Xiangtai Zhang, Hui Wang, Julian Key, Vladimir Linkov, Shan Ji, Xingli Wang, Ziqiang Lei, and Rongfang Wang. Strain effect of core-shell co@ pt/c nanoparticle catalyst with enhanced electrocatalytic activity for methanol oxidation. *Journal of the Electrochemical Society*, 159(3):B270, 2012.

[55] Cuiling Li, Muhammad Iqbal, Jianjian Lin, Xiliang Luo, Bo Jiang, Victor Malgras, Kevin C-W Wu, Jeonghun Kim, and Yusuke Yamauchi. Electrochemical deposition: an advanced approach for templated synthesis of nanoporous metal architectures. *Accounts of chemical research*, 51(8):1764–1773, 2018.

[56] Aditi Halder, Sudhanshu Sharma, MS Hegde, and N Ravishankar. Controlled attachment of ultrafine platinum nanoparticles on functionalized carbon nanotubes with high electrocatalytic activity for methanol oxidation. *The Journal of Physical Chemistry C*, 113(4): 1466–1473, 2009.

[57] Chien-Te Hsieh, Po-Yuan Yu, Dong-Ying Tzou, Jo-Pei Hsu, and Ya-Ru Chiu. Bimetallic pd–rh nanoparticles onto reduced graphene oxide nanosheets as electrocatalysts for methanol oxidation. *Journal of Electroanalytical Chemistry*, 761:28–36, 2016.

[58] Yanli Wang, Zhongshui Li, Shuhong Xu, Yixin Xie, and Shen Lin. Highly dispersive platinum nanoparticles supporting on polyaniline modified three dimensional graphene and catalyzing methanol oxidation. *Materials Research Bulletin*, 102:172–179, 2018.

[59] Thulasi Radhakrishnan and N Sandhyarani. Three dimensional assembly of electrocatalytic platinum nanostructures on reduced graphene oxide–an electrochemical approach for high performance catalyst for methanol oxidation. *International Journal of Hydrogen Energy*, 42(10):7014–7022, 2017.

[60] Tianou He, Weicong Wang, Fenglei Shi, Xiaolong Yang, Xiang Li, Jianbo Wu, Yadong Yin, and Mingshang Jin. Mastering the surface strain of platinum catalysts for efficient electrocatalysis. *Nature*, 598(7879):76–81, 2021.

[61] A Maksic, Z Rakocevic, M Smiljanic, M Nenadovic, and S Strbac. Methanol oxidation on pd/pt (poly) in alkaline solution. *Journal of Power Sources*, 273:724–734, 2015.

[62] Asad Ali and Pei Kang Shen. Recent advances in graphene-based platinum and palladium electrocatalysts for the methanol oxidation reaction. *Journal of Materials Chemistry A*, 7 (39):22189–22217, 2019.

[63] Flavio Colmati, Ermete Antolini, and Ernesto R Gonzalez. Pt–sn/c electrocatalysts for methanol oxidation synthesized by reduction with formic acid. *Electrochimica Acta*, 50 (28):5496–5503, 2005.

[64] Xiaoqing Lu, Zhigang Deng, Chen Guo, Weili Wang, Shuxian Wei, Siu-Pang Ng, Xiangfeng Chen, Ning Ding, Wenyue Guo, and Chi-Man Lawrence Wu. Methanol oxidation on pt3sn (111) for direct methanol fuel cells: methanol decomposition. *ACS Applied Materials & Interfaces*, 8(19):12194–12204, 2016.

[65] Gabor Samjeské, Hongsen Wang, Thomas Löffler, and Helmut Baltruschat. Co and methanol oxidation at pt-electrodes modified by mo. *Electrochimica Acta*, 47(22-23):3681–3692, 2002.

[66] Audrey S Duke, Randima P Galhenage, Samuel A Tenney, Salai C Ammal, Andreas Heyden, Peter Sutter, and Donna A Chen. In situ ambient pressure x-ray photoelectron spectroscopy studies of methanol oxidation on pt (111) and pt–re alloys. *The Journal of Physical Chemistry C*, 119(40):23082–23093, 2015.

[67] Yang Xiao, Yuan Wang, and Arvind Varma. Low-temperature selective oxidation of methanol over pt-bi bimetallic catalysts. *Journal of catalysis*, 363:144–153, 2018.

[68] Maxim Smetanin, RN Viswanath, Dominik Kramer, Dirk Beckmann, Thomas Koch, Ludwig A Kibler, Dieter M Kolb, and J Weissmuller. Surface stress-charge response of a (111)-textured gold electrode under conditions of weak ion adsorption. *Langmuir*, 24(16): 8561–8567, 2008.

[69] M Smetanin, D Kramer, S Mohanan, U Herr, and J Weissmüller. Response of the potential of a gold electrode to elastic strain. *Physical Chemistry Chemical Physics*, 11(40):9008–9012, 2009.

[70] Qibo Deng, Daniel-Hendrik Gosslar, Maxim Smetanin, and Jörg Weissmüller. Electrocapillary coupling at rough surfaces. *Physical Chemistry Chemical Physics*, 17(17):11725–11731, 2015.

[71] Kai Yan, Tuhina Adit Maark, Alireza Khorshidi, Vijay A Sethuraman, Andrew A Peterson, and Pradeep R Guduru. The influence of elastic strain on catalytic activity in the hydrogen evolution reaction. *Angewandte Chemie International Edition*, 55(21):6175–6181, 2016.

[72] Kai Yan, Seok Ki Kim, Alireza Khorshidi, Pradeep R Guduru, and Andrew A Peterson. High elastic strain directly tunes the hydrogen evolution reaction on tungsten carbide. *The Journal of Physical Chemistry C*, 121(11):6177–6183, 2017.

[73] Fernando MF Rhen and Cian McKeown. Enhanced methanol oxidation on strained pt films. *The Journal of Physical Chemistry C*, 121(5):2556–2562, 2017.

[74] Bo You, Michael T Tang, Charlie Tsai, Frank Abild-Pedersen, Xiaolin Zheng, and Hong Li. Enhancing electrocatalytic water splitting by strain engineering. *Advanced Materials*, 31(17):1807001, 2019.

[75] Qibo Deng, Maxim Smetanin, and Jörg Weissmüller. Mechanical modulation of reaction rates in electrocatalysis. *Journal of catalysis*, 309:351–361, 2014.

[76] Han Zhu, Guohua Gao, Mingliang Du, Jinhui Zhou, Kai Wang, Wenbo Wu, Xu Chen, Yong Li, Piming Ma, Weifu Dong, et al. Atomic-scale core/shell structure engineering induces precise tensile strain to boost hydrogen evolution catalysis. *Advanced Materials*, 30(26): 1707301, 2018.

[77] Xuesi Wang, Yihan Zhu, Anthony Vasileff, Yan Jiao, Shuangming Chen, Li Song, Bin Zheng, Yao Zheng, and Shi-Zhang Qiao. Strain effect in bimetallic electrocatalysts in the hydrogen evolution reaction. *ACS Energy Letters*, 3(5):1198–1204, 2018.

[78] Ryan P Jansonius, Phil A Schauer, David J Dvorak, Benjamin P MacLeod, David K Fork, and Curtis P Berlinguette. Strain influences the hydrogen evolution activity and absorption capacity of palladium. *Angewandte Chemie International Edition*, 59(29):12192–12198, 2020.

[79] Li Jiao, Ershuai Liu, Sooyeon Hwang, Sanjeev Mukerjee, and Qingying Jia. Compressive strain reduces the hydrogen evolution and oxidation reaction activity of platinum in alkaline solution. *ACS Catalysis*, 11(13):8165–8173, 2021.

[80] Zhiqian Hou, Chenghao Cui, Yanni Li, Yingjie Gao, Deming Zhu, Yuanfan Gu, Guoyu Pan, Yaqiong Zhu, and Tao Zhang. Lattice-strain engineering for heterogenous electrocatalytic oxygen evolution reaction. *Advanced Materials*, 35(39):2209876, 2023.

[81] Peter Strasser. Free electrons to molecular bonds and back: closing the energetic oxygen reduction (orr)–oxygen evolution (oer) cycle using core–shell nanoelectrocatalysts. *Accounts of Chemical Research*, 49(11):2658–2668, 2016.

[82] Menggang Li, Zhonglong Zhao, Zhonghong Xia, Mingchuan Luo, Qinghua Zhang, Yingnan Qin, Lu Tao, Kun Yin, Yuguang Chao, Lin Gu, et al. Exclusive strain effect boosts overall water splitting in pdcu/ir core/shell nanocrystals. *Angewandte Chemie*, 133(15):8324–8331, 2021.

[83] S Anantharaj, SR Ede, K Karthick, S Sam Sankar, K Sangeetha, PE Karthik, and Subrata Kundu. Precision and correctness in the evaluation of electrocatalytic water splitting: revisiting activity parameters with a critical assessment. *Energy & Environmental Science*, 11(4):744–771, 2018.

[84] L Yu and Z Ren. Systematic study of the influence of ir compensation on water electrolysis. *Materials Today Physics*, 14:100253, 2020.

[85] Allen J Bard, Larry R Faulkner, and Henry S White. *Electrochemical methods: fundamentals and applications.* John Wiley & Sons, 2022.

[86] Alexandros Ch Lazanas and Mamas I Prodromidis. Electrochemical impedance spectroscopy a tutorial. *ACS Measurement Science Au*, 3(3):162–193, 2023.

[87] Taewhan Kim, Woosung Choi, Heon-Cheol Shin, Jae-Young Choi, Ji Man Kim, Min-Sik Park, and Won-Sub Yoon. Applications of voltammetry in lithium ion battery research. *Journal of Electrochemical Science and Technology*, 11(1):14–25, 2020.

[88] Digby D Macdonald. Reflections on the history of electrochemical impedance spectroscopy. *Electrochimica Acta*, 51(8-9):1376–1388, 2006.

[89] Byoung-Yong Chang and Su-Moon Park. Electrochemical impedance spectroscopy. *Annual Review of Analytical Chemistry*, 3:207–229, 2010.

[90] Woosung Choi, Heon-Cheol Shin, Ji Man Kim, Jae-Young Choi, and Won-Sub Yoon. Modeling and applications of electrochemical impedance spectroscopy (eis) for lithium-ion batteries. *Journal of Electrochemical Science and Technology*, 11(1):1–13, 2020.

[91] Xiaobo Yang, Yingyong Wang, Xili Tong, and Nianjun Yang. Strain engineering in electrocatalysts: fundamentals, progress, and perspectives. *Advanced Energy Materials*, 12(5): 2102261, 2022.

[92] Ro Shuttleworth. The surface tension of solids. *Proceedings of the physical society. Section A*, 63(5):444, 1950.

[93] Lord Rayleigh. On the tension of recently formed liquid surfaces. *Proceedings of the Royal Society of London*, 47:281–287, 1889.

[94] Joseph Louis Lagrange. *Mécanique analytique*, volume 1. Mallet-Bachelier, 1853.

[95] Jörg Weissmüller. Adsorption–strain coupling at solid surfaces. *Current opinion in chemical engineering*, 24:45–53, 2019.

[96] George Gerald Stoney. The tension of metallic films deposited by electrolysis. *Proceedings of the Royal Society of London. Series A, Containing Papers of a Mathematical and Physical Character*, 82(553):172–175, 1909.

[97] J Lipkowski, W Schmickler, DM Kolb, and R Parsons. Comments on the thermodynamics of solid electrodes. *Journal of Electroanalytical Chemistry*, 452(2):193–197, 1998.

[98] Wolfgang Haiss, Richard J Nichols, Jürgen K Sass, and Klaus P Charle. Linear correlation between surface stress and surface charge in anion adsorption on au (111). *Journal of Electroanalytical chemistry*, 452(2):199–202, 1998.

[99] Ludwig A Kibler, Ahmed M El-Aziz, Rüdiger Hoyer, and Dieter M Kolb. Tuning reaction rates by lateral strain in a palladium monolayer. *Angewandte Chemie International Edition*, 44(14):2080–2084, 2005.

[100] GOKHSHTE. AY. Charge acquirement by an elastically strained electrode. *Doklady Akademii Nauk SSSR*, 187(3):601, 1969.

[101] Vijay A Sethuraman, Deepa Vairavapandian, Manon C Lafouresse, Tuhina Adit Maark, Naba Karan, Shouheng Sun, Ugo Bertocci, Andrew A Peterson, Gery R Stafford, and Pradeep R Guduru. Role of elastic strain on electrocatalysis of oxygen reduction reaction on pt. *The Journal of Physical Chemistry C*, 119(33):19042–19052, 2015.

[102] Aleksandr Ya Gokhshtein. The estance method. *Russian Chemical Reviews*, 44(11):921, 1975.

[103] Maxim Smetanin, Qibo Deng, Domink Kramer, Senthilnathan Mohanan, Ulrich Herr, and Jörg Weissmüller. Reply to the ‘comment on “response of the potential of a gold electrode to elastic strain”’by á. horváth, g. nagy and r. schiller, phys. chem. chem. phys., 2010, 12. *Physical Chemistry Chemical Physics*, 12(26):7291–7292, 2010.

[104] Yoshitaka Umeno, Christian Elsässer, Bernd Meyer, Peter Gumbsch, Martina Nothacker, Jörg Weißmüller, and Ferdinand Evers. Ab initio study of surface stress response to charging. *EPL (Europhysics Letters)*, 78(1):13001, 2007.

[105] Herbert B Callen. Thermodynamics and an introduction to thermostatistics, 1998.

[106] J Weissmüller and D Kramer. Balance of force at curved solid metal- liquid electrolyte interfaces. *Langmuir*, 21(10):4592–4603, 2005.

[107] RP Buck and LR Griffith. Voltammetric and chronopotentiometric study of the anodic oxidation of methanol, formaldehyde, and formic acid. *Journal of the Electrochemical Society*, 109(11):1005, 1962.

[108] J Prabhuram and R Manoharan. Investigation of methanol oxidation on unsupported platinum electrodes in strong alkali and strong acid. *Journal of Power Sources*, 74(1): 54–61, 1998.

[109] M Chojak-Halseid, Zenonas Jusys, and Rolf Jürgen Behm. Methanol oxidation over a pt/c catalyst at high temperatures and pressure: an online electrochemical mass spectrometry study. *The Journal of Physical Chemistry C*, 114(51):22573–22581, 2010.

[110] Jamie L Cohen, David J Volpe, and Hector D Abruna. Electrochemical determination of activation energies for methanol oxidation on polycrystalline platinum in acidic and alkaline electrolytes. *Physical Chemistry Chemical Physics*, 9(1):49–77, 2007.

[111] Tom HM Housmans, Ad H Wonders, and Marc TM Koper. Structure sensitivity of methanol electrooxidation pathways on platinum: an on-line electrochemical mass spectrometry study. *The Journal of Physical Chemistry B*, 110(20):10021–10031, 2006.

[112] XH Xia, T Iwasita, F Ge, and W Vielstich. Structural effects and reactivity in methanol oxidation on polycrystalline and single crystal platinum. *Electrochimica Acta*, 41(5):711–718, 1996.

[113] H Wang, Th Löffler, and H Baltruschat. Formation of intermediates during methanol oxidation: A quantitative dems study. *Journal of applied electrochemistry*, 31(7):759–765, 2001.

[114] SS Mahapatra and J Datta. Characterization of pt-pd/c electrocatalyst for methanol oxidation in alkaline medium. *International Journal of Electrochemistry*, 2011, 2011.

[115] Guoyan Hou, Javier Parrondo, Vijay Ramani, and Jai Prakash. Kinetic and mechanistic investigation of methanol oxidation on a smooth polycrystalline pt surface. *Journal of The Electrochemical Society*, 161(3):F252, 2013.

[116] Erich Gülzow. Alkaline fuel cells: a critical view. *Journal of power sources*, 61(1-2):99–104, 1996.

[117] GT Burstein, CJ Barnett, AR Kucernak, and KR Williams. Aspects of the anodic oxidation of methanol. *Catalysis Today*, 38(4):425–437, 1997.

[118] Amalija V Tripković, K Dj Popović, Branimir N Grgur, B Blizanac, PN Ross, and NM Marković. Methanol electrooxidation on supported pt and ptru catalysts in acid and alkaline solutions. *Electrochimica Acta*, 47(22-23):3707–3714, 2002.

[119] John R Varcoe and Robert CT Slade. Prospects for alkaline anion-exchange membranes in low temperature fuel cells. *Fuel cells*, 5(2):187–200, 2005.

[120] H Angerstein-Kozlowska, BE Conway, and WBA Sharp. The real condition of electrochemically oxidized platinum surfaces: Part i. resolution of component processes. *Journal of Electroanalytical Chemistry and Interfacial Electrochemistry*, 43(1):9–36, 1973.

[121] AJ Appleby. Theory of successive electron transfer steps in cyclic voltammetry: Application to oxygen pseudocapacitance on platinum. *Journal of The Electrochemical Society*, 120(9): 1205, 1973.

[122] DM Dražić, AV Tripković, K Dj Popović, and JD Lović. Kinetic and mechanistic study of hydroxyl ion electrosorption at the pt (111) surface in alkaline media. *Journal of Electroanalytical Chemistry*, 466(2):155–164, 1999.

[123] S Wilhelm, T Iwasita, and W Vielstich. Coh and co as adsorbed intermediates during methanol oxidation on platinum. *Journal of electroanalytical chemistry and interfacial electrochemistry*, 238(1-2):383–391, 1987.

[124] Shao Xiong Liu, Ling Wen Liao, Qian Tao, Yan Xia Chen, and Shen Ye. The kinetics of co pathway in methanol oxidation at pt electrodes, a quantitative study by atr-ftir spectroscopy. *Physical Chemistry Chemical Physics*, 13(20):9725–9735, 2011.

[125] Teresa Iwasita. Electrocatalysis of methanol oxidation. *Electrochimica Acta*, 47(22-23): 3663–3674, 2002.

[126] A Hamnett. Mechanism and electrocatalysis in the direct methanol fuel cell. *Catalysis today*, 38(4):445–457, 1997.

[127] J-M Léger. Mechanistic aspects of methanol oxidation on platinum-based electrocatalysts. *Journal of Applied Electrochemistry*, 31(7):767–771, 2001.

[128] D Cao, G-Q Lu, Andrzei Wieckowski, Sally A Wasileski, and Matthew Neurock. Mechanisms of methanol decomposition on platinum: A combined experimental and ab initio approach. *The Journal of Physical Chemistry B*, 109(23):11622–11633, 2005.

[129] VS Bagotzky, Yu B Vassiliev, and OA Khazova. Generalized scheme of chemisorption, electrooxidation and electroreduction of simple organic compounds on platinum group metals. *Journal of Electroanalytical Chemistry and Interfacial Electrochemistry*, 81(2):229–238, 1977.

[130] R Parsons and T VanderNoot. The oxidation of small organic molecules: A survey of recent fuel cell related research. *Journal of electroanalytical chemistry and interfacial electrochemistry*, 257(1-2):9–45, 1988.

[131] Li Xiao, Zhan Zhao, Lidong Du, Shaohua Wu, and Qimin Liu. Annealing effect on the stability of platinum thin films covered by sio 2 or sin x layer. In *The 8th Annual IEEE International Conference on Nano/Micro Engineered and Molecular Systems*, pages 352–355. IEEE, 2013.

[132] U Schmid and H Seidel. Effect of high temperature annealing on the electrical performance of titanium/platinum thin films. *Thin Solid Films*, 516(6):898–906, 2008.

[133] David Nečas and Petr Klapetek. Gwyddion: an open-source software for spm data analysis. *Open Physics*, 10(1):181–188, 2012.

[134] ML Meade. Advances in lock-in amplifiers. *Journal of Physics E: Scientific Instruments*, 15(4):395, 1982.

[135] Liwei Lin, Albert P Pisano, and Roger T Howe. A micro strain gauge with mechanical amplifier. *Journal of Microelectromechanical Systems*, 6(4):313–321, 1997.

[136] Karl Hoffmann. *Applying the wheatstone bridge circuit.* HBM Darmstadt, Germany, 1974.

[137] Dan Mihai Ştefănescu. Strain gauges and wheatstone bridges—basic instrumentation and new applications for electrical measurement of non-electrical quantities. In *Eighth International Multi-Conference on Systems, Signals & Devices*, pages 1–5. IEEE, 2011.

[138] CL Bauer and RJ Farris. Determination of poisson's ratio for polyimide films. *Polymer Engineering & Science*, 29(16):1107–1110, 1989.

[139] Jongpal Kim, Dong-il Cho, and Richard S Muller. Why is (111) silicon a better mechanical material for mems? In *Transducers' 01 Eurosensors XV: The 11th International Conference on Solid-State Sensors and Actuators June 10–14, 2001 Munich, Germany*, pages 662–665. Springer, 2001.

[140] WA Brantley. Calculated elastic constants for stress problems associated with semiconductor devices. *Journal of Applied Physics*, 44(1):534–535, 1973.

[141] K Dahmen, S Lehwald, and H Ibach. Bending of crystalline plates under the influence of surface stress—a finite element analysis. *Surface science*, 446(1-2):161–173, 2000.

[142] E Herrero, K Franaszczuk, and A Wieckowski. Electrochemistry of methanol at low index crystal planes of platinum: An integrated voltammetric and chronoamperometric study. *The Journal of Physical Chemistry*, 98(19):5074–5083, 1994.

[143] Sengeni Anantharaj and Suguru Noda. ir drop correction in electrocatalysis: everything one needs to know! *Journal of Materials Chemistry A*, 10(17):9348–9354, 2022.

[144] K Tammeveski, T Tenno, J Claret, and C Ferrater. Electrochemical reduction of oxygen on thin-film pt electrodes in 0.1 m koh. *Electrochimica Acta*, 42(5):893–897, 1997.

[145] MM Jaksic, B Johansen, and R Tunold. Electrochemical behaviour of platinum in alkaline and acidic solutions of heavy and regular water. *International journal of hydrogen energy*, 18(10):817–837, 1993.

[146] H Angerstein-Kozlowska, BE Conway, B Barnett, and J Mozota. The role of ion adsorption in surface oxide formation and reduction at noble metals: general features of the surface process. *Journal of Electroanalytical Chemistry and Interfacial Electrochemistry*, 100(1-2): 417–446, 1979.

[147] Theo AM Suter, Keenan Smith, Jennifer Hack, Lara Rasha, Zahra Rana, Gyen Ming A Angel, Paul R Shearing, Thomas S Miller, and Dan JL Brett. Engineering catalyst layers for next-generation polymer electrolyte fuel cells: a review of design, materials, and methods. *Advanced Energy Materials*, 11(37):2101025, 2021.

[148] Leon Jacobse, Yi-Fan Huang, Marc TM Koper, and Marcel J Rost. Correlation of surface site formation to nanoisland growth in the electrochemical roughening of pt (111). *Nature materials*, 17(3):277–282, 2018.

[149] Alexander Björling and Juan M Feliu. Electrochemical surface reordering of pt (1 1 1): A quantification of the place-exchange process. *Journal of electroanalytical chemistry*, 662 (1):17–24, 2011.

[150] Jean Clavilier, Kamal El Achi, and Antonio Rodes. In situ characterization of the pt (s)-[n (111)/sx (111)] electrode surfaces using electrosorbed hydrogen for probing terrace an step sites. *Journal of electroanalytical chemistry and interfacial electrochemistry*, 272(1-2): 253–261, 1989.

[151] José Solla-Gullón, Paramaconi Rodríguez, Enrique Herrero, Antonio Aldaz, and Juan M Feliu. Surface characterization of platinum electrodes. *Physical Chemistry Chemical Physics*, 10(10):1359–1373, 2008.

[152] Ana Mª Gómez-Marín and Juan M Feliu. Oxide growth dynamics at pt (1 1 1) in absence of specific adsorption: a mechanistic study. *Electrochimica Acta*, 104:367–377, 2013.

[153] Maria JTC Van Der Niet, Nuria Garcia-Araez, Javier Hernández, Juan M Feliu, and Marc TM Koper. Water dissociation on well-defined platinum surfaces: The electrochemical perspective. *Catalysis today*, 202:105–113, 2013.

[154] Leon Jacobse, Marcel J Rost, and Marc TM Koper. Atomic-scale identification of the electrochemical roughening of platinum. *ACS central science*, 5(12):1920–1928, 2019.

[155] Brian E Conway. Electrochemical oxide film formation at noble metals as a surface-chemical process. *Progress in surface science*, 49(4):331–452, 1995.

[156] B Beden, F Kadirgan, C Lamy, and JM Leger. Oxidation of methanol on a platinum electrode in alkaline medium: effect of metal ad-atoms on the electrocatalytic activity. *Journal of Electroanalytical Chemistry and Interfacial Electrochemistry*, 142(1-2):171–190, 1982.

[157] F Kadirgan, B Beden, JM Leger, and C Lamy. Synergistic effect in the electrocatalytic oxidation of methanol on platinum+ palladium alloy electrodes. *Journal of Electroanalytical Chemistry and Interfacial Electrochemistry*, 125(1):89–103, 1981.

[158] Dong Young Chung, Kyung-Jae Lee, and Yung-Eun Sung. Methanol electro-oxidation on the pt surface: revisiting the cyclic voltammetry interpretation. *The Journal of Physical Chemistry C*, 120(17):9028–9035, 2016.

[159] Thomas Holm, Per Kristian Dahlstrøm, Svein Sunde, Frode Seland, and David A Harrington. Dynamic electrochemical impedance study of methanol oxidation at pt at elevated temperatures. *Electrochimica Acta*, 295:139–147, 2019.

[160] I-Ming Hsing, Xin Wang, and Yong-Jun Leng. Electrochemical impedance studies of methanol electro-oxidation on pt/c thin film electrode. *Journal of the Electrochemical Society*, 149(5):A615, 2002.

[161] Ryan E Melnick and G Tayhas R Palmore. Impedance spectroscopy of the electro-oxidation of methanol on polished polycrystalline platinum. *The Journal of Physical Chemistry B*, 105(5):1012–1025, 2001.

[162] Demudu Babu Gorle, Venkatesh Velacheri Kumman, and Manickam Anbu Kulandainathan. Highly efficient, large surface area and spherically shaped pt particles deposited electrolytically synthesized graphene for methanol oxidation with impedance spectroscopy. *international journal of hydrogen energy*, 42(25):16258–16268, 2017.

[163] Lindsay R Merte, Farzad Behafarid, Daniel J Miller, Daniel Friebel, Sangwan Cho, Felix Mbuga, Dimosthenis Sokaras, Roberto Alonso-Mori, Tsu-Chien Weng, Dennis Nordlund, et al. Electrochemical oxidation of size-selected pt nanoparticles studied using in situ high-energy-resolution x-ray absorption spectroscopy. *Acs Catalysis*, 2(11):2371–2376, 2012.

[164] Masahiro Seo and Yoko Serizawa. Changes in surface stress of platinum electrode in acidic and alkaline sulfate or alkaline fluoride solutions. *Journal of The Electrochemical Society*, 150(10):E472, 2003.

[165] L. L. Mickelson and C. Friesen. Direct observation of bifunctional electrocatalysis during co oxidation at ru0=0.37/pt111 surfaces via surface stress measurements. *Journal of the American Chemical Society*, 131(41):14879–14884, 2009.

[166] Yeyoung Ha, Justin L Oberst, Zhenhua Zeng, Thao TH Hoang, Yair Cohen, David J Wetzel, Ralph G Nuzzo, Jeffrey Greeley, and Andrew A Gewirth. In situ surface stress measurement and computational analysis examining the oxygen reduction reaction on pt and pd. *Electrochimica Acta*, 260:400–406, 2018.

[167] Eric D Rus, Ryo H Wakabayashi, Hongsen Wang, and Héctor D Abruña. Methanol oxidation at platinum in alkaline media: a study of the effects of hydroxide concentration and of mass transport. *ChemPhysChem*, 22(13):1397–1406, 2021.

[168] Leandro MC Pinto, Paola Quaino, Mauricio D Arce, Elizabeth Santos, and Wolfgang Schmickler. Electrochemical adsorption of oh on pt (111) in alkaline solutions: combining dft and molecular dynamics. *ChemPhysChem*, 15(10):2003–2009, 2014.

[169] Lihua Lai, Guangxing Yang, Qiao Zhang, Hao Yu, and Feng Peng. Essential analysis of cyclic voltammetry of methanol electrooxidation using the differential electrochemical mass spectrometry. *Journal of Power Sources*, 509:230397, 2021.

[170] Augusta M Hofstead-Duffy, De-Jun Chen, Shi-Gang Sun, and YuYe J Tong. Origin of the current peak of negative scan in the cyclic voltammetry of methanol electro-oxidation on pt-based electrocatalysts: a revisit to the current ratio criterion. *Journal of Materials Chemistry*, 22(11):5205–5208, 2012.

[171] Rubén Rizo, Julia Fernández-Vidal, Laurence J Hardwick, Gary A Attard, Francisco J Vidal-Iglesias, Victor Climent, Enrique Herrero, and Juan M Feliu. Investigating the presence of adsorbed species on pt steps at low potentials. *Nature communications*, 13(1): 2550, 2022.

[172] P. J. Feibelman. First-principles calculations of stress induced by gas adsorption on pt(111). *Physical Review B*, 56(4):2175–2182, 1997.

[173] J Weissmüller, RN Viswanath, LA Kibler, and DM Kolb. Impact of surface mechanics on the reactivity of electrodes. *Physical Chemistry Chemical Physics*, 13(6):2114–2117, 2011.

[174] Manon C Lafouresse, Ugo Bertocci, and Gery R Stafford. Dynamic stress analysis applied to (111)-textured pt in hclo4 electrolyte. *Journal of the Electrochemical Society*, 160(9): H636, 2013.

[175] Yeyoung Ha, Zhenhua Zeng, Yair Cohen, Jeffrey Greeley, and Andrew A Gewirth. Electrochemical surface stress development during co and no oxidation on pt. *The Journal of Physical Chemistry C*, 120(16):8674–8683, 2016.

[176] Thao TH Hoang, Yair Cohen, and Andrew A Gewirth. In situ electrochemical stress measurements examining the oxygen evolution reaction in basic electrolytes. *Analytical chemistry*, 86(22):11290–11297, 2014.

[177] Sung Sakong and Axel Groß. Methanol oxidation on pt (111) from first-principles in heterogeneous and electrocatalysis. *Electrocatalysis*, 8:577–586, 2017.

[178] Jeff Greeley and Manos Mavrikakis. Competitive paths for methanol decomposition on pt (111). *Journal of the American Chemical Society*, 126(12):3910–3919, 2004.

[179] Sanket K Desai, Matthew Neurock, and K Kourtakis. A periodic density functional theory study of the dehydrogenation of methanol over pt (111). *The Journal of Physical Chemistry B*, 106(10):2559–2568, 2002.

[180] Eric M. Karp, Trent L. Silbaugh, Matthew C. Crowe, and Charles T. Campbell. Energetics of adsorbed methanol and methoxy on pt(111) by microcalorimetry. *Journal of the American Chemical Society*, 134(50):20388–20395, 2012.

[181] L Mickelson, Th Heaton, and Cody Friesen. Surface stress observations during the adsorption and electrochemical oxidation of co on pt {111}. *The Journal of Physical Chemistry C*, 112(4):1060–1063, 2008.

[182] Larry L Mickelson and Cody Friesen. Direct observation of bifunctional electrocatalysis during co oxidation at ruθ= 0.37/pt {111} surfaces via surface stress measurements. *Journal of the American Chemical Society*, 131(41):14879–14884, 2009.

[183] LAURO OLIVER Paz-Borbon, RL Johnston, G Barcaro, and ALESSANDRO Fortunelli. Chemisorption of co and h on pd, pt and au nanoclusters: a dft approach. *The European Physical Journal D*, 52(1-3):131–134, 2009.

[184] Yeyoung Ha, Justin L Oberst, Zhenhua Zeng, Thao TH Hoang, Yair Cohen, David J Wetzel, Ralph G Nuzzo, Jeffrey Greeley, and Andrew A Gewirth. In situ surface stress measurement and computational analysis examining the oxygen reduction reaction on pt and pd. *Electrochimica Acta*, 260:400–406, 2018.

[185] J. Weissmüller, R. N. Viswanath, D. Kramer, P. Zimmer, R. Würschum, and H. Gleiter. Charge-induced reversible strain in a metal. *Science*, 300(5617):312–315, 2003.

[186] RN Viswanath, D Kramer, and J Weissmüller. Adsorbate effects on the surface stress–charge response of platinum electrodes. *Electrochimica Acta*, 53(6):2757–2767, 2008.

[187] Qibo Deng, Varun Gopal, and Jörg Weissmüller. Less noble or more noble: How strain affects the binding of oxygen on gold. *Angewandte Chemie International Edition*, 54(44): 12981–12985, 2015.

[188] Xingqun Zheng, Li Li, Jing Li, and Zidong Wei. Intrinsic effects of strain on low-index surfaces of platinum: roles of the five 5d orbitals. *Physical Chemistry Chemical Physics*, 21(6):3242–3249, 2019.

[189] Rongfang Wang, Hui Wang, Fan Luo, and Shijun Liao. Core–shell-structured low-platinum electrocatalysts for fuel cell applications. *Electrochemical Energy Reviews*, 1:324–387, 2018.

[190] W. Vielstich. Zum mechanismus der elektrochemischen oxydation von methylalkohol. *Chemie Ingenieur Technik*, 35(5):362–367, 1963.

[191] Frode Seland, Reidar Tunold, and David A Harrington. Activating and deactivating mass transport effects in methanol and formic acid oxidation on platinum electrodes. *Electrochimica acta*, 55(9):3384–3391, 2010.

[192] Vinod Kumar Puthiyapura, Wen-Feng Lin, Andrea E. Russell, Dan J. L. Brett, and Christopher Hardacre. Effect of mass transport on the electrochemical oxidation of alcohols over electrodeposited film and carbon-supported pt electrodes. *Topics in Catalysis*, 61(3):240–253, 2018.